ISSN 1590-8844
Vol. 10 No 02
2009

International Journal of Mechanics and Control

Editor: Andrea Manuello Bertetto

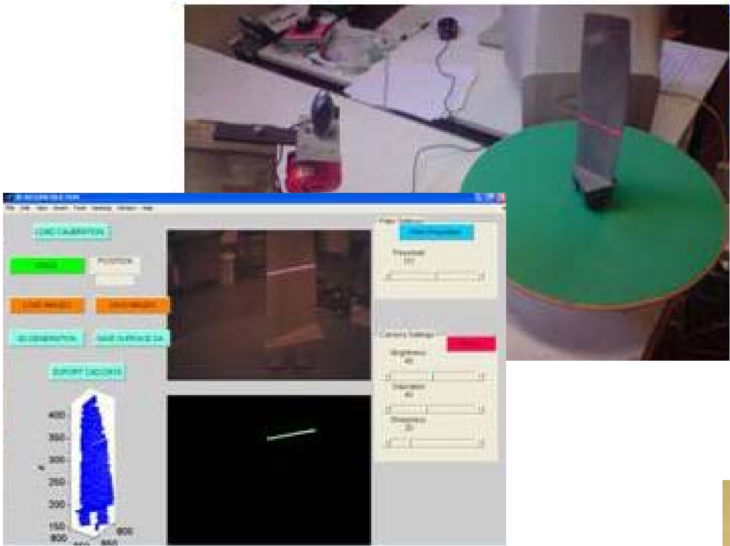

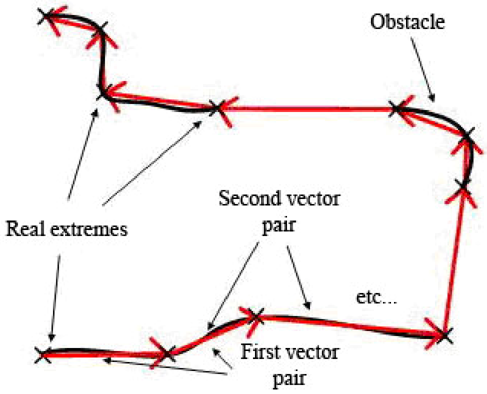

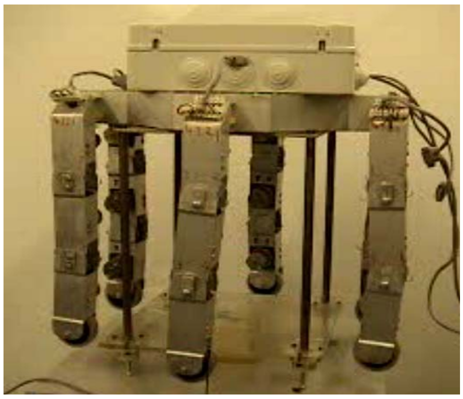

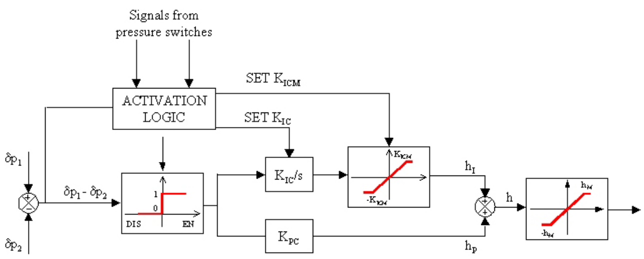

LIBRERIA EDITRICE UNIVERSITARIA
LEVROTTO & BELLA
TORINO

Official Torino Italy Court Registration
n.5390, 5th May 2000

Deposito presso il Tribunale di Torino
numero 5390 del 5 maggio 2000
Direttore responsabile:
Andrea Manuello Bertetto

International Journal of Mechanics and Control

The Journal is addressed to scientists and engineers who work in the fields of mechanics (mechanics, machines, systems, control, structures). It is edited in Turin (Northern Italy) by Levrotto&Bella Co., with an international board of editors. It will have not advertising.
Turin has a great and long tradition in mechanics and automation of mechanical systems. The journal would will to satisfy the needs of young research workers of having their work published on a qualified paper in a short time, and of the public need to read the results of researches as fast as possible.
Interested parties will be University Departments, Private or Public Research Centres, Innovative Industries.

Aims and scope

The *International Journal of Mechanics and Control* publishes as rapidly as possible manuscripts of high standards. It aims at providing a fast means of exchange of ideas among workers in Mechanics, at offering an effective method of bringing new results quickly to the public and at establishing an informal vehicle for the discussion of ideas that may still in the formative stages.

Language: English

International Journal of Mechanics and Control will publish both scientific and applied contributions. The scope of the journal includes theoretical and computational methods, their applications and experimental procedures used to validate the theoretical foundations. The research reported in the journal will address the issues of new formulations, solution, algorithms, computational efficiency, analytical and computational kinematics synthesis, system dynamics, structures, flexibility effects, control, optimisation, real-time simulation, reliability and durability. Fields such as vehicle dynamics, aerospace technology, robotics and mechatronics, machine dynamics, crashworthiness, biomechanics, computer graphics, or system identification are also covered by the journal.

Please address contributions to

Prof. Guido Belforte
Prof. Andrea Manuello Bertetto
PhD Eng. Elvio Bonisoli

Dept. of Mechanics
Technical University - Politecnico di Torino
C.so Duca degli Abruzzi, 24.
10129 - Torino - Italy - E.C.

www.jomac.it
e_mail: jomac@polito.it

Subscription information

Subscription order must be sent to
the publisher:

Libreria Editrice Universitaria
Levrotto&Bella
2/E via Pigafetta – 10129 Torino – Italy

www.levrotto-bella.net
e_mail: info@levrotto-bella.net
tel. +39.011.5097367
+39.011.5083690
fax +39.011.504025

ISSN 1590-8844
International Journal of Mechanics and Control, Vol. 10, No. 02, 2009

ROBOT ASSISTED LASER SCANNING

Cesare Rossi Sergio Savino Salvatore Strano
University of Napoli "Federico II"

ABSTRACT

The main aim of the research consists in the developing of a new method for the calibration of a 3-D laser scanner, mostly for robotic applications. The rig essentially consists in a laser emitter and a webcam with fixed relative positions. In addition, a cylindrical lens is provided with the laser housing in order to obtain a planar light. An optical filter was also used in order to segment the laser stripe from the rest of the scene.
The method was tested on both planar and non-planar surfaces. Tests confirmed that it is possible to calibrate the intrinsic parameters of the video system, the position of the image plane and the laser plane in a given frame, all in the same time. In addition it was possible to recognize and to record surface shapes with an appreciable accuracy. The authors present some test results showing that the proposed method can be used for robot assisted 3D surfaces recognition and recording. For this last purpose the test rig is fitted on a robot arm that permits to the scanner device to 'observe' the 3D object from different and known positions.
The method could be also used in other applications such as robotic kinematic calibration.

Keywords: robotic applications, laser scanning, vision systems, 3D reconstruction

1 INTRODUCTION

Laser scanning range sensors are widely used for high-precision, high-density three-dimensional (3D) reconstruction and inspection of the surface of physical objects [8]. The process typically involves planning a set of views, physically altering the relative object-sensor pose, taking scans, registering the acquired geometric data in a common coordinate frame of reference, and finally integrating range images into a non-redundant model [9]. Efficiencies could be achieved by automating or semi-automating this process. The first aim of the research was to study an analysis procedure to elaborate image of laser in order to obtain 3-D object reconstruction, after an opportune system calibration. The technique has been automated by developing an interactive GUI to acquire and to elaborate data. Reverse engineering is concerned with the problem of creating computer aided design (CAD) models of real objects by interpreting point data measured from their surfaces [9, 10]. For complex objects, it is important that the measuring device is free to move along arbitrary paths and make its measurements from suitable directions.

Contact author: Cesare Rossi

via Claudio, 21 – 80125 Napoli ITALY
E-mail: cesare.rossi@unina.it

The system is planned to be part of a future automatic system for the Reverse Engineering of unknown objects.The system was designed around a test rig developed in our department by means of a commercial linear laser and a common web-cam; this system is moved by a revolute robotic arm.

2 3-D RECONSTRUCTION: PRINCIPLE OF OPERATION

There are many methods in order to reconstruct the object shape by means of videos or images [1]. In this paper is described a system, that consists of a linear laser emitter and a webcam, and uses triangulation principle applied to a scanning belt on object surface, [2]. Camera observes the intersection between laser and object: laser line points in image frame, are the intersections between image plane and optical rays that pass through the intersection points between laser and object. By means of a transformation matrix, it is possible to express the image frame coordinates, in pixel, in a local reference frame. In figure 1 a) is shown a scheme of scanning system: {W} is local reference frame, {I} is image frame with coordinates system {u,v}, and {L} is laser frame. {L2} is laser plane that contains laser knife and scanning belt on the surface of object, and it coincides with (x,y) plane of laser frame {L}, [3].

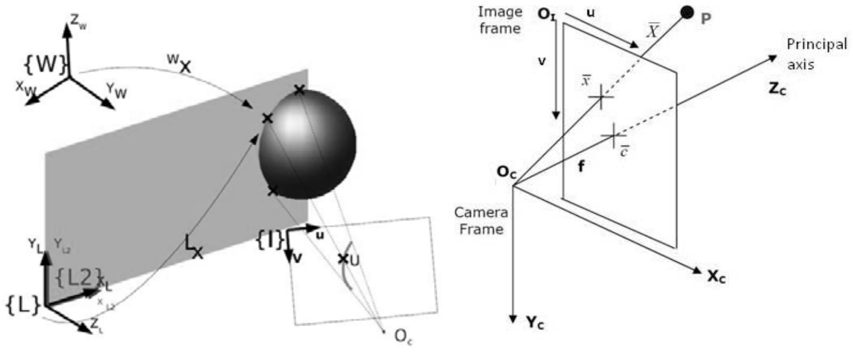

a) b)

Figure 1 Reference frames

Starting from the coordinates in pixel (u,v), in image frame, it is possible to write the coordinates of the scanning belt on the object surface, in camera frame by means of equation (1). Camera frame is located in camera focal point figure 1 b).

$$\begin{Bmatrix} x_c \\ y_c \\ z_c \\ 1 \end{Bmatrix} = \begin{bmatrix} \delta_x & 0 & 0 & -\delta_x u_0 \\ 0 & \delta_y & 0 & -\delta_y v_0 \\ 0 & 0 & 0 & f \\ 0 & 0 & 0 & 1 \end{bmatrix} = \begin{Bmatrix} u \\ v \\ 0 \\ 1 \end{Bmatrix} \tag{1}$$

With:
(u_0,v_0): image frame coordinates of focal point projection in image plane;
(δ_x, δ_y): physical dimension of sensor pixel along direction u and v;
f: focal length.
It is possible to write the expression of the optical beam of a generic point in the image frame, that can be identified by means of parameter t.

$$\begin{cases} x_c = (u-u_0)\delta_x t \\ y_c = (v-v_0)\delta_y t \\ z_c = ft \end{cases} \tag{2}$$

Laser frame {L} is rotated and translated respect to camera frame, the steps and their sequence are:
1. Translation Δx_{lc} along axis x_c;
2. Translation Δy_{lc} along axis y_c;
3. Translation Δz_{lc} along axis z_c;
4. Rotation φ_{lc} around axis z_c;
5. Rotation θ_{lc} around axis y_c;
6. Rotation ψ_{lc} around axis x_c ;

Hence in equation (3) the transformation matrix between laser frame and camera frame is:

$$\left[{}^cT_l\right] = \begin{bmatrix} 1 & 0 & 0 & 0 \\ 0 & \cos(\psi_{lc}) & -\sin(\psi_{lc}) & 0 \\ 0 & \sin(\psi_{lc}) & \cos(\psi_{lc}) & 0 \\ 0 & 0 & 0 & 1 \end{bmatrix} \cdot \begin{bmatrix} \cos(\theta_{lc}) & 0 & \sin(\theta_{lc}) & 0 \\ 0 & 1 & 0 & 0 \\ -\sin(\theta_{lc}) & 0 & \cos(\theta_{lc}) & 0 \\ 0 & 0 & 0 & 1 \end{bmatrix} \cdot \begin{bmatrix} \cos(\varphi_{lc}) & -\sin(\varphi_{lc}) & 0 & 0 \\ \sin(\varphi_{lc}) & \cos(\varphi_{lc}) & 0 & 0 \\ 0 & 0 & 1 & 0 \\ 0 & 0 & 0 & 1 \end{bmatrix} \cdot \begin{bmatrix} 1 & 0 & 0 & 0 \\ 0 & 1 & 0 & 0 \\ 0 & 0 & 1 & \Delta z_{lc} \\ 0 & 0 & 0 & 1 \end{bmatrix} \cdot \begin{bmatrix} 1 & 0 & 0 & 0 \\ 0 & 1 & 0 & \Delta y_{lc} \\ 0 & 0 & 1 & 0 \\ 0 & 0 & 0 & 1 \end{bmatrix} \cdot \begin{bmatrix} 1 & 0 & 0 & \Delta x_{lc} \\ 0 & 1 & 0 & 0 \\ 0 & 0 & 1 & 0 \\ 0 & 0 & 0 & 1 \end{bmatrix} \tag{3}$$

Laser plane {L2} coincides with (x,y) plane of laser frame {L}, so it contains three points:

$$\{p\}_l = \{0,0,0,1\}^T; \{q\}_l = \{1,0,0,1\}^T; \{r\}_l = \{0,0,1,1\}^T \tag{4}$$

In camera frame:

$$\{p_x, p_y, p_z, 1\}_c^T = \left[{}^cT_l\right]^{-1}\{p\}_l; \{q_x, q_y, q_z, 1\}_c^T = \left[{}^cT_l\right]^{-1}\{q\}_l; \{r_x, r_y, r_z, 1\}_c^T = \left[{}^cT_l\right]^{-1}\{r\}_l \tag{5}$$

It is possible to obtain laser plane equation in camera frame, solving equation (6) in x_c, y_c and z_c.

$$\det\begin{bmatrix} x_c - p_x & y_c - p_y & z_c - p_z \\ q_x - p_x & q_y - p_y & q_z - p_z \\ r_x - p_x & r_y - p_y & r_z - p_z \end{bmatrix} = 0 \tag{6}$$

If it is:

$$M_x = \det\begin{bmatrix} q_y - p_y & q_z - p_z \\ r_y - p_y & r_z - p_z \end{bmatrix}; M_y = \det\begin{bmatrix} q_x - p_x & q_z - p_z \\ r_x - p_x & r_z - p_z \end{bmatrix};$$

$$M_z = \det\begin{bmatrix} q_x - p_x & q_y - p_y \\ r_x - p_x & r_y - p_y \end{bmatrix}$$

ISSN 1590-8844
International Journal of Mechanics and Control, Vol. 10, No. 02, 2009

equation in camera frame, is:

$$(x_c - p_x)M_x - (y_c - p_y)M_y + (z_c - p_z)M_z = 0 \tag{7}$$

It is possible to evaluate coordinates x_c, y_c e z_c, in camera frame, solving system (8) with unknown t:

$$\begin{cases} x_c = (u - u_0)\delta_x t \\ y_c = (v - v_0)\delta_y t \\ z_c = ft \\ (x_c - p_x)M_x - (y_c - p_y)M_y + (z_c - p_z)M_z = 0 \end{cases} \tag{8}$$

The solution is:

$$t = \frac{p_x M_x - p_y M_y + p_z M_z}{(u - u_o)\delta_x M_x - (v - v_o)\delta_y M_y + f M_z} \tag{9}$$

Equation (9) permits to compute in the camera frame, the points coordinates of the scanning belt on the object surfaces, starting to its image coordinates (u,v). In this way it is possible to carry out a 3-D objects reconstruction by means of a laser knife.

3 DETECTION OF THE LASER PATH

A very important step for 3-D reconstruction is image elaboration for the laser path on the target, [4, 5, 6] , the latter is shown in figure 2.

Figure 2 Laser path image.

Image elaboration procedure permits to user to choose some image points of laser line, in order to identify three principal colours (Red, Green, and Blue) of laser line, figure 3.

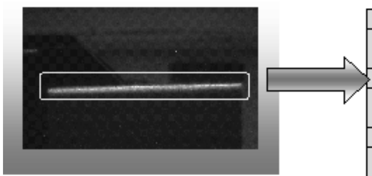

R	G	B
247	72	72
226	161	143
248	118	114
242	249	185
225	135	153
233	157	148
240	140	154
225	220	192
237	226	210
240	160	129

Figure 3

With mean values of scanning belt principal colours, it is possible to define a brightness coefficient of the laser line, according to relation (10):

$$s = \frac{\max(mean(R), mean(G), mean(B)) + \min(mean(R), mean(G), mean(B))}{2} \tag{10}$$

By means of relation (11), an intensity analysis is carried out on RGB image.

$$L(u,v) = \frac{\max(R,G,B) + \min(R,G,B)}{2} \tag{11}$$

By equation (11), the matrix that contains the three layers of RGB image, is transformed in a matrix L, that represents image intensity. This matrix represents same initial image, but it gives information only about luminous intensity in each image pixel, and so it is a grayscale expression of initial RGB image, figure 4 a) and b).

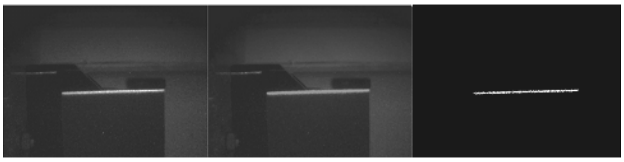

a) b) c)

Figure 4 a) RGB initial image;
b) grayscale initial image L; c) matrix I_b.

With relation (12), it is possible to define a logical matrix I_b. Matrix I_b indicates pixels of matrix L with a brightness in a range of 15% brightness coefficient s.

$$I_b(u,v) = \begin{cases} 1 & se \quad 0.85 \cdot s \le L(u,v) \le 1.15 \cdot s \\ 0 & otherwise \end{cases} \tag{12}$$

In figure 4 c), matrix I_b is shown.

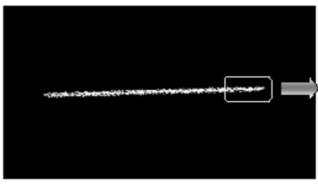

0	0	0	0	0	0	0	0	0	0	0	0	0	0	0
1	1	0	0	0	1	1	0	0	0	0	0	1	0	0
0	1	1	1	1	1	1	0	1	1	1	1	1	0	0
0	1	1	1	1	1	1	1	1	1	1	1	1	1	0
1	1	1	1	1	1	1	1	1	1	1	1	1	1	1
1	0	0	0	0	0	0	0	0	0	1	0	1	1	1
1	0	0	1	1	0	0	0	0	0	1	0	1	1	1
0	0	0	0	1	1	1	1	0	0	0	1	0	0	0
0	0	0	0	0	0	0	0	0	0	0	0	0	0	0

Figure 5 I_b representation.

In matrix I_b, the scanning belt on the object surface (see fig. 5) is represented by means of the pixel value one. The area of the laser path in the image plane depends on the real dimension of laser beam and on external factors such as: reflection phenomena, inclination of object surfaces.

3-D reconstruction procedure is based on triangulation principle and it doesn't consider the laser beam thickness, so it is necessary to associate a line to the image of scanning belt.

Since the laser path in the image plane is rather horizontal, a geometrical mean is computed on, on the columns of the matrix I_b, that is to say: in the opposite direction to wider extension of the laser path in the image. This is shown in equation (13).

$$\Omega := \{u,v\};\ \bar{\Omega} := \{\bar{u},\bar{v}\} \Rightarrow$$
$$\{\bar{u} = \frac{\sum_{u,v\in\Omega} u I_b(u,v)}{\sum_{u,v\in\Omega} I_b(u,v)} \neq \infty, \bar{v} = v : \sum_{u,v\in\Omega} I_b(u,v) \neq 0\} \qquad (13)$$

Then a matrix h_p is also defined as follows:

$$h_b(u,v) = \begin{cases} 1 & se \quad \{u,v\} \in \bar{\Omega} \\ 0 & otherwise \end{cases} \qquad (14)$$

Matrix h_b is hence a logical matrix with same dimension of I_b in which that represents laser image like a line, figure 6. This line is centre line of scanning belt on object surface in image.

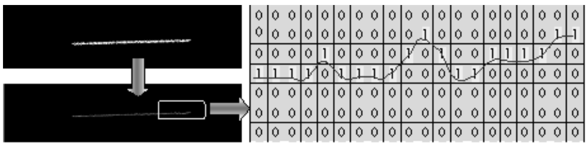

Figure 6 h_b representation.

The set of transformations (11), (12) and (13) represents the image elaboration, that is necessary to identify a laser line in image. The points of this line are used in 3-D reconstruction procedure.

4 CALIBRATION PROCEDURE

It is necessary to identify all model parameters in order to obtain a good 3-D reconstruction. Calibration is a basic procedure for the data analysis, [3, 5, 7]. For this reason, it was developed a calibration procedure for a classic laser scanner module.

The laser scanner module is composed by a web-cam with resolution 640x480 pixel and a linear laser. The calibration test rig is realized with a guide on which is fixed the laser scanner module and a digital micrometer with a target, figure 7 a).

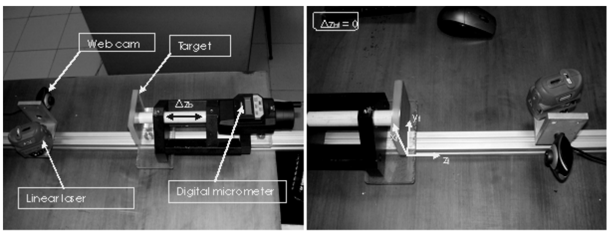

a) b)

Figure 7 a) laser scanner module calibration test rig; b) fixed frame $O_f x_f y_f z_f$.

A fixed frame $O_f x_f y_f z_f$ has origin in a vertex of the rectangular target with dimension a=68 mm and b=74.5 mm, like it is shown in figure 7 b). Target movements are indicated with Δz_{bf}.

In figure 8 some steps of calibration procedure are shown.

Figure 8 Calibration procedure steps.

Calibration procedure is based on a set of images, taken with the target placed in different positions respect to the laser scanner module. A least square optimization allows to identify all parameters. In figure 9 are shown 10 images used for calibration, of scanning belt, with 10 different Δ_{zbf}.

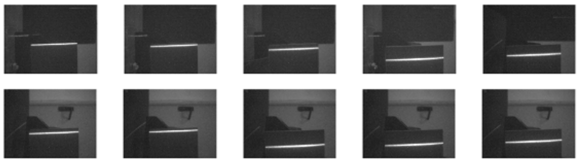

Figure 9 Images used for calibration.

The aim of calibration procedure is to obtain the parameters that define the relation between laser frame $Lx_L y_L z_L$ and camera frame $O_c x_c y_c z_c$, figure 1.

In every calibration step, it is possible to define transformation matrix between fixed frame $O_f x_f y_f z_f$ and target frame:

$$\left[{}^fT_b\right] = [1 \quad 0 \quad 0 \quad 0; 0 \quad 1 \quad 0 \quad 0; 0 \quad 0 \quad 1 \quad -\Delta z^i_{fb}; 0 \quad 0 \quad 0 \quad 1] \qquad (13)$$

The transformation matrix between fixed frame $O_f x_f y_f z_f$ and camera frame $O_c x_c y_c z_c$ can be optained analogous to matrix $[{}^cT_l]$, and it is a function of six parameters:

$$\left[{}^fT_c\right] = f(\Delta x_{cf}, \Delta y_{cf}, \Delta z_{cf}, \psi_{cf}, \theta_{cf}, \varphi_{cf}) = f(\pi_{cf}) \qquad (14)$$

with π_{cf} set of parameter of transformation $[{}^fT_c]$.

Equation (3) can be written as:

$$\left[{}^cT_l\right] = g(\Delta x_{lc}, \Delta y_{lc}, \Delta z_{lc}, \psi_{lc}, \theta_{lc}, \varphi_{lc}) = f(\pi_{lc}) \qquad (15)$$

with π_{lc} set of parameter of transformation $[{}^cT_l]$.

For each step of the calibration procedure it is possible to evaluate the coordinates of the points of the laser line in the camera frame, according to equations (5) and (13):

$$\{\bar{x}_c, \bar{y}_c, \bar{z}_c, 1\}_i^T = f(\pi_{lc}, f) \cdot \{\bar{u}, \bar{v}, 0, 1\}_i^T \qquad (16)$$

By means of equation (14), it is possible to write:

$$\{\bar{x}_f, \bar{y}_f, \bar{z}_f, 1\}_i^T = \left[{}^fT_c\right]^{-1} \cdot \{\bar{x}_c, \bar{y}_c, \bar{z}_c, 1\}_i^T =$$
$$\left[{}^fT_c\right]^{-1} \cdot f(\pi_{lc}, f) \cdot \{\bar{u}, \bar{v}, 0, 1\}_i^T = \omega(\pi_{cf}, \pi_{lc}, f) \cdot \{\bar{u}, \bar{v}, 0, 1\}_i^T \qquad (17)$$

The optimization problem can be defined as:

$$\min_{\rho \in R^{13}} F(\rho)^2 \quad (18)$$

F(ρ) is a vectorial function defined as:

$$\begin{aligned} F(\rho) = \{ & (\bar{z}_f^{i+1} - \bar{z}_f^i) - (\Delta\bar{z}_{bf}^{i+1} - \Delta\bar{z}_{bf}^{i+1}), \min(\bar{x}_f^i), \\ & \max(\bar{x}_f^i) - a, \max(\bar{z}_f^i) - \min(\bar{z}_f^i), \\ & \max(\bar{y}_f^i) - \min(\bar{y}_f^i), \min(\bar{y}_f^1), \min(\bar{z}_f^1)\}^T \end{aligned} \quad (19)$$

With a least square optimization, the unknown parameters of set [π_{cf}, π_{lc}, f] are identified.
An interactive GUI was developed to allow the user to acquire images, to execute optimization and to verify the results.
In figure 10, a graphical result of calibration is shown: it is possible to observe the camera frame position, the laser beam (represented by the quadrilateral on the left), and the 3-D reconstructions of scanning beam on target surface, for each image used in the calibration procedure.

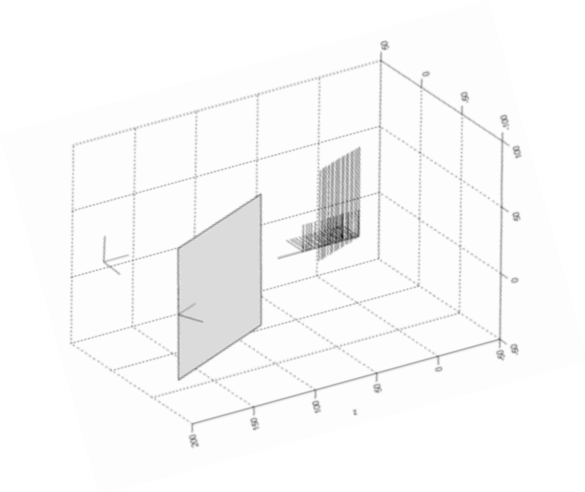

Figure 10 Calibration results.

5 SYSTEM ACURACY

5.1 CAMERA ERROR

An obvious source of camera calibration error arises from the spatial quantization of the image. However, many times the image event of interest spans many pixels. It is then possible to calculate the centroid of this event to sub-pixel accuracy, thereby reducing the spatial quantization error. Limiting the sub-pixel accuracy is the fact that in general the perspective projection of an object's centroid does not equal the centroid of the object's perspective projection. However, often times the error incurred from assuming the centroid of the projection is the projection of the centroid is quite small [14].
Camera accuracy is a function of its distance from observed object.

If an unitary variation of pixels in the directions u and v is considered, from the equation (2) is gotten:

$$x_c = (u + 1 - u_0)\delta_x \frac{z_c}{f}$$
$$y_c = (v + 1 - v_0)\delta_y \frac{z_c}{f}$$

Calculating the difference respectively between x_c and y_c after and before the variation is gotten the accuracy of the system, that is the variation of x_c and y_c that it can be gotten for a minimum variation in terms of pixels in the image frame:

$$\Delta x_c = x_c(u+1) - x_c(u)$$
$$\Delta y_c = y_c(v+1) - y_c(v)$$

The image accuracies in directions x_c and y_c are:

$$a^c{}_x = \delta_u \cdot \frac{z_c}{f}$$
$$a^c{}_y = \delta_v \cdot \frac{z_c}{f} \quad (20)$$

5.2 SCANNER MODULE ERROR

It is possible to define an accuracy expression for 3D-reconstruction that can be obtained by means of laser scanner module, according to equations (8) and (9).
A variation (α, β) of image coordinates (u,v), generates a variation of parameter t of equation (9):

$$\Delta t = \frac{-(p_x M_x - p_y M_y + p_z M_z) \cdot (\alpha\delta_x M_x - \beta\delta_y M_y)}{(u\delta_x M_x + \alpha\delta_x M_x - v\delta_y M_y - \beta\delta_y M_y + fM_z) \cdot (u\delta_x M_x - v\delta_y M_y + fM_z)} \quad (21)$$

where:
- α pixel variation in u direction;
- β pixel variation in v direction;

The variation of parameter t, allows to define an expression of accuracy of 3D reconstruction. In fact, by means of equation (8), it is possible to obtain the variation of coordinates in camera frame in function of variation of image coordinates:

$$\begin{cases} \Delta x_c = \alpha\delta_u \cdot \dfrac{p_x M_x - p_y M_y + p_z M_z}{(u - u_o + \alpha)\delta_x M_x - (v - v_o + \beta)\delta_y M_y + fM_z} + (u - u_0)\delta_x \cdot \Delta t \\ \Delta y_c = \beta\delta_v \cdot \dfrac{p_x M_x - p_y M_y + p_z M_z}{(u - u_o + \alpha)\delta_x M_x - (v - v_o + \beta)\delta_y M_y + fM_z} + (v - v_0)\delta_y \cdot \Delta t \\ \Delta z_c = \Delta t \cdot f \end{cases} \quad (22)$$

An unitary variation of image coordinates (α=1 and β=0, or α=0 and β=1, or α=1 and β=1), allows to define three accuracy parameters of scanner laser 3D reconstruction:

$$\begin{cases} a^{SL}{}_x = \Delta x_c \\ a^{SL}{}_y = \Delta y_c \\ a^{SL}{}_z = \Delta z_c \end{cases} \Rightarrow with \Rightarrow \begin{cases} (\alpha, \beta) = (0,1) \\ or \\ (\alpha, \beta) = (1,0) \\ or \\ (\alpha, \beta) = (1,1) \end{cases} \quad (23)$$

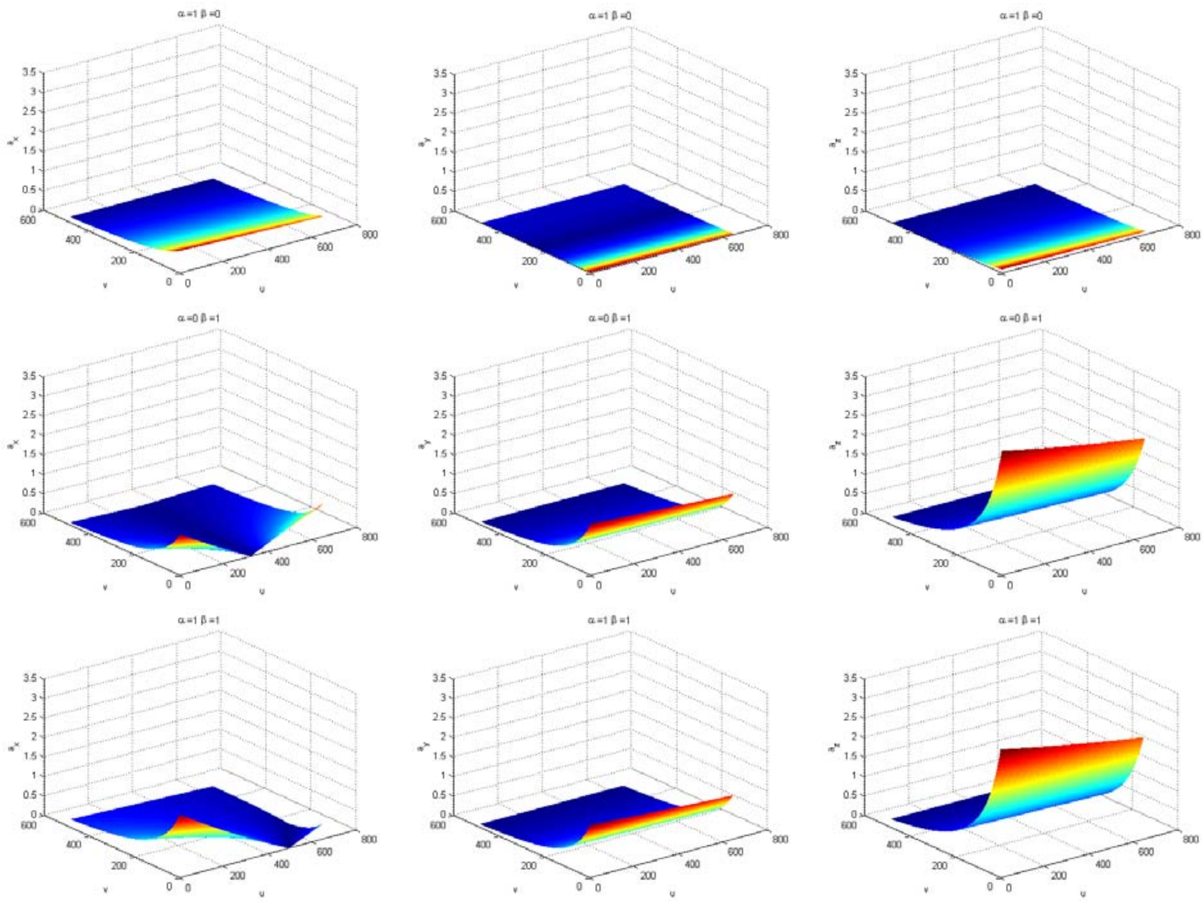

Figure 10 Error of the accuracy.

As it has shown in the figure 10, the worst accuracy of the laser scanner for a pixel variation is in the direction z_c. Besides it can be seen that a_z has minimum value for values of $v = d_v$ and it grows up to $v = 1$ with a non-linear law.

5.3 LASER PRECISION

Most of the outlier and other erroneous points are caused by reflections. In these cases, the high energy laser beam is reflected from mirroring surfaces such as metal or glass. Therefore, too much light hits the sensor of the camera and so-called blooming effects occur. In other cases, a direct reflection may miss the camera. In addition, a part of the object may lie in the path from the projected laser line to the camera causing a shadowing effect. All these effects are responsible for gaps and holes. At sharp edges of some objects, partial reflections appear. In addition, craggy surfaces cause multiple reflections and, therefore, indefinite point correlations.

Furthermore, aliasing effects in the 2D image processing of laser beam, lead to high frequent noise in the generated 3D data [15].

The laser beam thickness in the image, can vary because of the above described effects, but 3-D reconstruction procedure is based on triangulation principle and it doesn't consider this phenomenon. In fact, the detection of laser path allows to identify a line in image with a thickness of a pixel.

The real laser beam thickness and its path thickness in the image, must be considered to evaluate the precision of 3D reconstruction.

The accuracy $a^c{}_z$ becomes worse, if a thickness parameter is considered. This parameter is a generalized measure of laser beam thickness in pixel, and it can be expressed with two components: th_u thickness measure along direction u in image frame and th_v thickness measure along direction v in image frame.

An expression of 3D reconstruction accuracy in direction z of camera frame, can be obtained by means of equation (3), in which parameters (α, β) are the generalized laser beam thickness (th_u, th_v):

$$\begin{cases} a_x = \Delta x_c \\ a_y = \Delta y_c \Rightarrow with \Rightarrow (\alpha, \beta) = (th_u / 2, th_v / 2) \\ a_z = \Delta z_c \end{cases} \tag{24}$$

The equations (24) define the resolution of the laser scanner 3-D reconstruction, and they allows to evaluate the accuracy of each point coordinates that is obtained with laser beam image elaboration.

5.4 SCANNER RANGE

Another characteristic of a 3D laser scanner is the minimum and the maximum distance between a generic point of a surface and the image plane. These parameters define the range of the scanning procedure. Decreasing the angle θ of inclination of the laser plain respect to the plain $x_c z_c$ of the camera frame at a respective fixed distance s the range of scanning increases (figure 11).

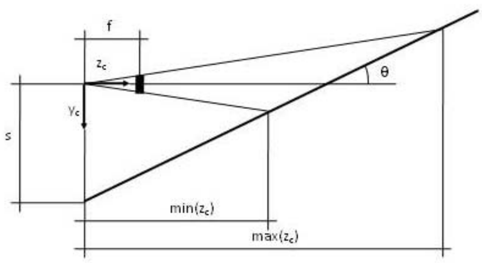

Figure 11

This is not a good solution since to decrease of this angle the accuracy a_z worsens notably as is shown in figure 12.

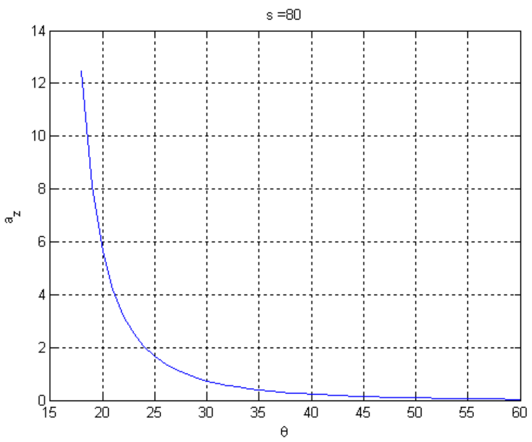

Figure 12

For the considered system with values s = 90 mm and θ = 23° it have been gotten: $max(z_c)$ = 525 mm and $min(z_c)$ = 124 mm;

6 EXPERIMENTAL RESULTS

To evaluate the accuracy of the laser scanner system, it was fixed on a robot arm, in this way it was possible to capture a lot of shape information of the object from different views.

6.1 EXPERIMENTAL RIG

6.1.1 Laser Scanner Module

Our rig, is based on a laser profile, that essentially consists in a line laser and a camera. The laser beam defines a “laser plane” and the part of the laser plane that lies in the image view of the camera is denoted the “scanning window”, figure 13.

Figure 13 Scanner module

The laser scanner device was realized by assembling a commercial linear laser and a common web-cam.

6.1.2 Robot

In order to optimize the accuracy of the reconstruction resulting model, scanning should be adapted to the shape of the object. One way to do that is to use an industrial robot to move a laser profile scanner along curved paths.

The scanner laser module was mounted on a revolute robot with three d.o.f., designed and assembled in our Department, figure 14.

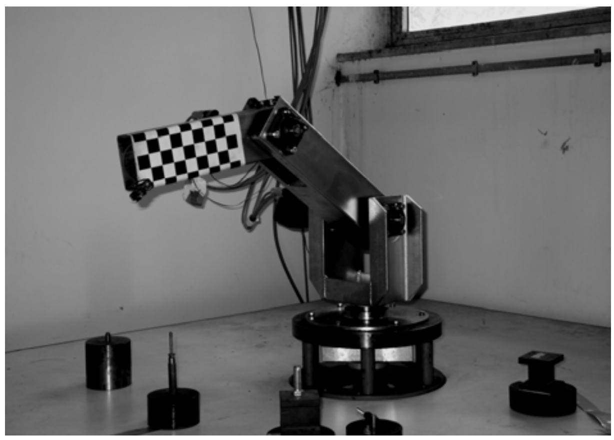

Figure 14 Revolute robot

The robot serves as a measuring device to determine the scanning window position and orientation in 3D for each camera picture, with a great precision. All scan profiles captured during a scan sequence must be mapped to a common 3D coordinate system, and to do this, positional information from the robot were used [11]. Figure 15 shows the equipment at work.

The authors have developed a solution where the robot controller and scanner software work separately during a scan sequence that will be described in the following paragraphs.

ISSN 1590-8844
International Journal of Mechanics and Control, Vol. 10, No. 02, 2009

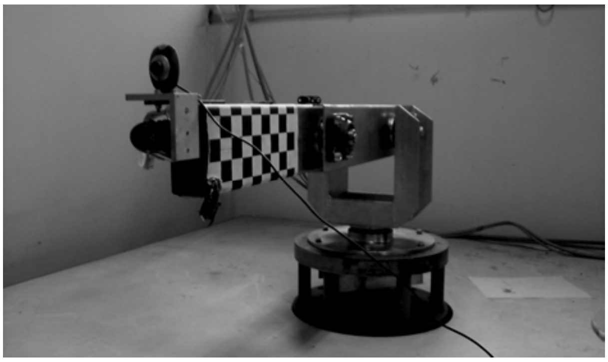

Figure 15 The robot scanning system.

6.2 MODEL OF THE LASER SCANNER ON THE ROBOT

When the laser scanner module is installed on the robot, figure 15, it is possible to use positional information from robot to determine the scanning window position and orientation in 3D.

Defining [*DH*] as the transformation matrix between coordinates in the robot base frame 0 (the fixed one) and those in frame 3 (the one of the last link), figure 16, for the coordinates of a generic point *P* exists this relationship:

$$\{P\}_0 = [DH] \cdot \{P\}_3 \tag{20}$$

The matrix [DH] depends on 9 constant kinematic structure parameters, that are known, and 3 variable joints position parameters that are measurable by means of robot control system.

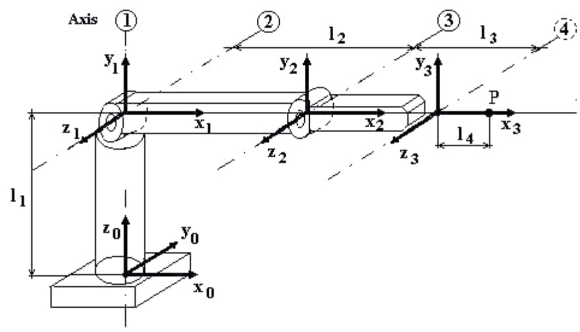

Figure 16 Revolute robot scheme.

Knowing the transformation matrix $[^cT_3]$ between the camera frame and the frame of the robot last link, it is possible to obtain a transformation matrix between the camera frame and the frame 0, figure 17.

$$\{P\}_c = [^cT_3] \cdot [DH]^{-1} \cdot \{P\}_0 \tag{21}$$

By means of the equations (8), (9) and (21), the relationship between image coordinates *(u,v)* of the laser path and its coordinates in the robot base frame 0, is defined. By means of these equations, it is possible to reconstruct the 3D points in the robot base frame, of the intersection between the laser line and the object.

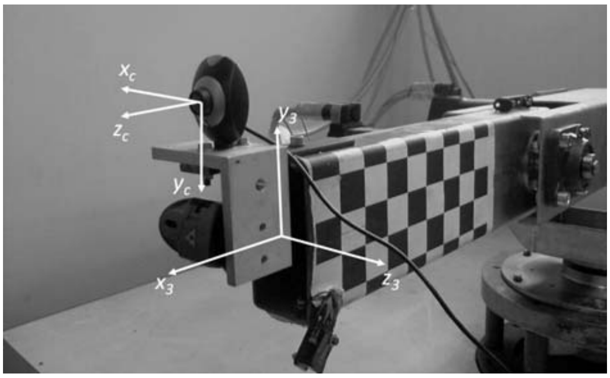

Figure 17 Camera reference system.

Robot positioning errors do not influence the 3D reconstruction, because each image is acquired and elaborated in a real robot position, that is known by means of robot encoders [12].

6.3 DATA CAPTURE AND REGISTRATION

The scanner video camera captures profiles from the surface of the object as 2D coordinates in the laser plane. During a scan sequence the laser scanner module is moved in order to capture object images from different sides and with different angles-shot according to the shape of the object.

In Matlab, an interactive GUI was developed in order to allows users to acquire and to elaborate data, figure 18. For each camera picture, along the scan path, the scanner derives a scan profile built up of point coordinates, in real-time.

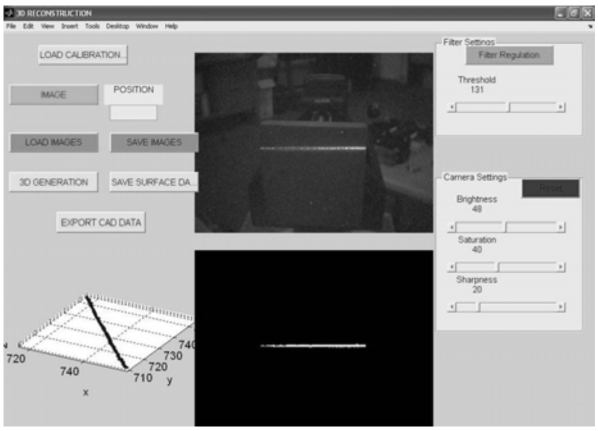

Figure 18 Developed software.

The first step present in the GUI is the load of the calibration parameters that are composed by the laser scanner parameters and the matrix $[^cT_3]$. The second step is to filter the pixels of the laser path from the image, to do this, there are some regulations: the identification of the intensity of selected pixels, the calculus of the threshold and other regulations of the camera settings. The third step is to write the 3 joint position parameters of the robot in the window "position" , after this, clicking on the button "Image" the software save all the information, necessary

for the reconstruction, in the workspace of the Matlab. Clicking on the button "3D generation" the software calculates the 3D positions of the laser path in the robot base frame, and the result is shown on the GUI window.
When the scanning procedure is completed, the user can save images and relative robot position information in a file, save the cloud of points represent the surface of the test object and export the surface information in a file format that permits to load the data from the CAD software "CATIA".
Besides it's possible to load image information from a preview scanning procedure, this is useful for reconstruct the same laser path information using different calibration parameters.

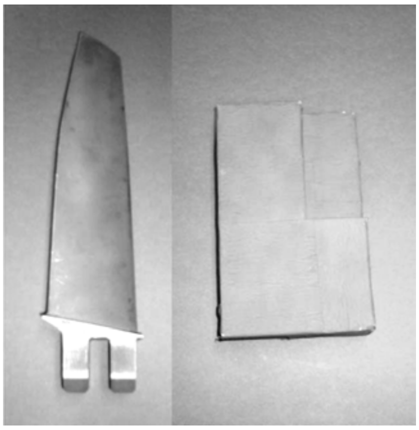

Figure 19 Test objects.

6.4 SURFACES RECONSTRUCTION
The system has been tested before in a fixed robot position, to verify calibration and reconstruction procedures, then the shape of some components, was defined using robot to move laser scanner module. The test objects are shown in the figure 19. In the figure 20 and 21 it is possible to see a step of the procedure with the final results for the two test specimens.
With the use of the software CATIA it was possible to build the surface of the two test objects, in this way it was obtained the CAD model, this step of the 3D reconstruction method is a real reverse engineering application.

The routine "Digitized shape editor" of the "CATIA" addresses digitalized data import, clean up, tessellation, cross sections, character line, shape and quality checking. In the figure 22 and 23 are shown the comparisons between the clouds of points and the respective surfaces for each object. In the figures 24 and 25, an evaluation of 3D-reconstruction accuracy is shown for the two analyzed test specimen. It is possible to observe, that these first results have the worst accuracy along direction z of camera frame, according to observations of paragraph 5.3.

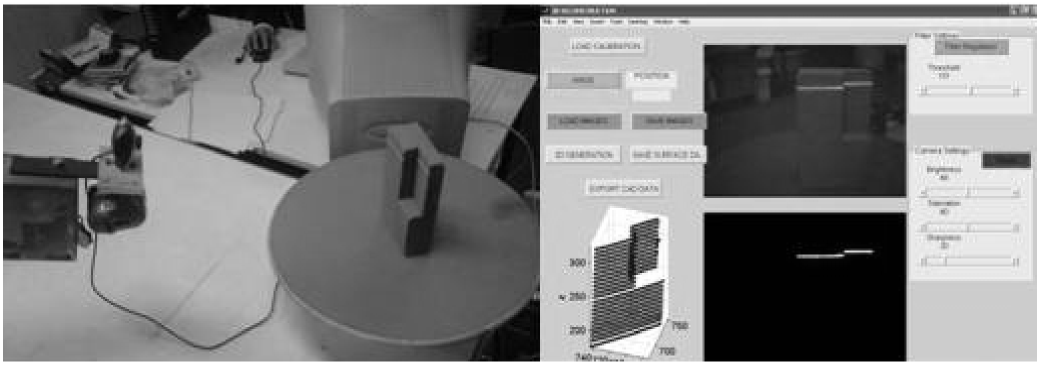

Figure 20 Elaboration procedure of the first test specimen.

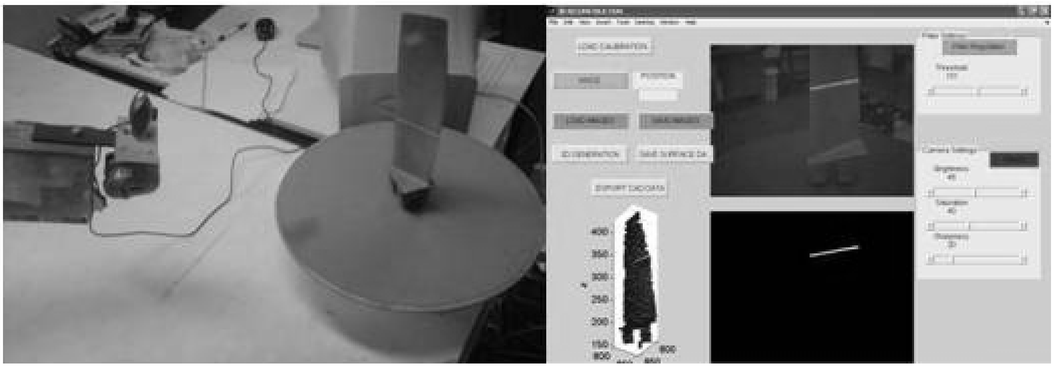

Figure 21 Elaboration procedure of the second test specimen.

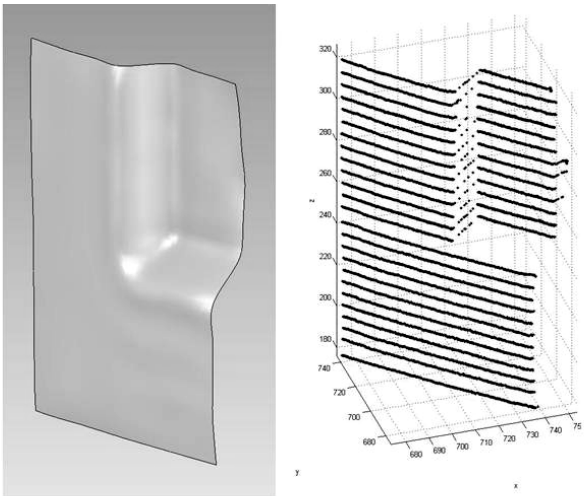

Figure 22 First test specimen results.

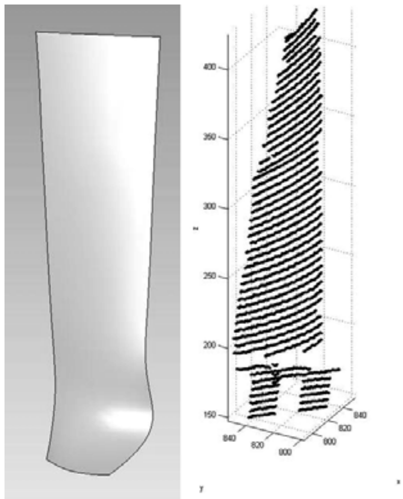

Figure 23 Second test specimen results.

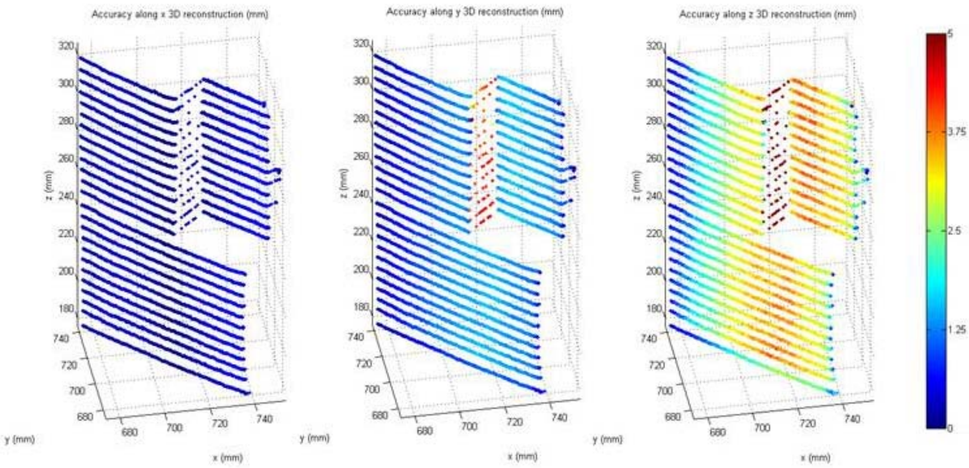

Figure 24 First test specimen results.

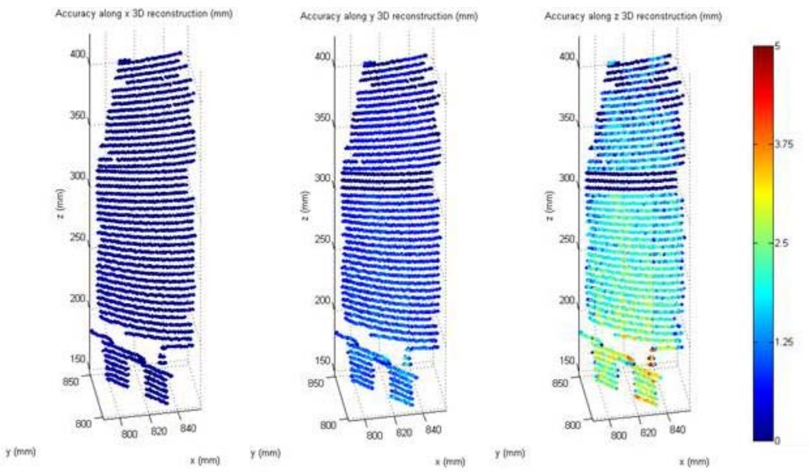

Figure 25 First test specimen results.

7 CONCLUSION

The proposed procedure is absolutely non-invasive since it does not involve any modification of the scene; in fact no markers with features visible by both the camera and the laser, or any other device, are required. The first results of a new method for real time shape acquisition with a laser scanner are presented. Although the test rig has been conceived just to validate the method (hence no high resolution cameras were adopted), the tests have showed encouraging results.

The first tests have shown encouraging results. These latter can be summarized as follows.

1. It is possible to calibrate the intrinsic parameters of the video system, the position of the image plane and the laser plane in a given frame, all in the same time.
2. The surface shapes can be recognized and recorded with an appreciable accuracy.
3. The proposed method can be used for robotic applications such as robotic kinematic calibration and 3D surfaces recognition and recording. For this last purpose the test rig was fitted on a robot arm that permitted to the scanner device to 'observe' the 3D object from different and known position.

A detailed analysis of the sources of errors and the verification of the accuracy has been carried on. As far as the latter aspect is concerned, the authors believe that a better system for tracking the position of the robot arm could enhance accuracy.

Finally, the authors would like to point out that the solution proposed is relatively low cost, scalable and flexible. It is also suitable for applications other than RE, like robot control or inspection.

REFERENCES

[1] F. Blais: "Review of 20 years of range sensor development", *Journal of Electronic Imaging* , Vol. 13, No. 1, pp. 231–240, 2004.

[2] D. Acosta, O. García and J. Aponte: "Laser Triangulation for shape acquisition in a 3D Scanner Plus Scanner", *Proc. of the Electronics Robotics and Automotive Mechanics Conference*, 2006.

[3] J. Forest:" New methods for triangulation-based shape acquisition using laser scanners", PhD thesis, University of Girona, 2004.

[4] C. Colombo, D. Comanducci and A. Del Bimbo: "Low-Cost 3D Scanning by Exploiting Virtual Image Symmetries", *Journal of Multimedia*, Vol. 1, No. 7, 2006.

[5] N. Koller: "Fully Automated Repair of Surface Flaws using an Artificial Vision Guided Robotic Grinder", *PhD thesis*, University of Leoben, 2007.

[6] C. Matabosch: "Hand-held 3D-scanner for large surface registration", PhD thesis, University of Girona, 2007.

[7] M. Ritter, M. Hemmleb, O. Sinram, J. Albertz and H. Hohenberg: "A Versatile 3D Calibration Object for Various Micro-range Measurement Methods", *Proc. of ISPRS*, pp. 696-701, Istanbul, 2004.

[8] L.A. Albuquerque and J.M.S.T. Motta: " Implementation of 3D Shape Reconstruction from Range Images for Object Digital Modeling", *ABCM Symposium Series in Mechatronics*, Vol. 2, pp.81-88, 2006.

[9] Sören Larsson and J.A.P. Kjellander: "Motion control and data capturing for laser scanning with an industrial robot", *Robotics and Autonomous Systems*, Vol.54, No.6, pp. 453-460, 30 June 2006.

[10] Sören Larsson and J.A.P. Kjellander: "Motion control and data capturing for laser scanning with an industrial robot", *Robotics and Autonomous Systems*, Vol.54, No.6, pp. 453-460, 30 June 2006.

[11] R.A. Jarvis and Y.L. Chiu: "Robotic Replication of 3D Solids", Proceedings of IROS, 1996.

[12] V. Niola, C. Rossi and S. Savino: "Vision System for Industrial Robots Path Planning", *Journal of Mechanics and Control*, 2007.

[13] Cesare Rossi, Sergio Savino and Salvatore Strano, "3D object reconstruction using a robot arm", *Proc. of 2-nd European Conference on Mechanism Science*, Cassino, Italy, 2008.

[14] J. Russell Noseworthy, Arthur M. Ryan, Lester A. Gerhardt: "Camera and Laser Scanner Calibration with Imprecise Data", *Proc. of Third Annual Conference on Intelligent Robotic Systems for Space Exploration,* pp. 99-111, 1991.

[15] C. Teutsch, T. Isenberg, E. Trostmann, M. Weber: "Evaluation and Optimization of Laser Scan Data", *15th Simulation and Visualisation,* March 4–5, 2004.

ISSN 1590-8844
International Journal of Mechanics and Control, Vol. 10, No. 02, 2009

TRIANGULATION OF MOBILE ROBOT POSITION WITH DETECTED INHERENT ENVIRONMENT LANDMARKS

Ladislav Jurišica   František Duchoň

Faculty of Electrical Engineering and Information Technology,
Institute of Control and Industrial Informatics, Ilkovičova 3, Bratislava

ABSTRACT

The aim of this paper is to design methods for relation assignation between direct movement and rotation among two positions of robot (relative position in environment) following information about environment in these positions obtained by laser scanner. It is assumed, that environment map neither relation between attributes (landmarks) are not known antecedent. For calculation of relative movement (rotation) between two positions of robot is used method of triangulation. Supposed method was verified on real system. Calculated value of movement (rotation) can be used for odometry correction.

Keywords: position of mobile robot, triangulation of mobile robot position, laser scanner, landmarks

1 INTRODUCTION

At mobile robot position identification with triangulation methods are assumed two situations. In first situation is assumed, that environment map, i.e. positions of the landmarks and relations between them are known. In this case is needed to solve equation for absolute position with 3 point triangulation [1], i.e. estimate of position and orientation. In second situation is assumed, that environment map is not known and relative displacement of mobile robot $-\varepsilon$ between two positions of this mobile robot in environment considering environment landmarks will be defined. This information can be than used for correction of odometry [6].

2 ASSIGNATION OF ABSOLUTE MOBILE ROBOT POSITION

At mobile robot absolute position identification will determinate its position $p = (R_x \ , R_y)$ and orientation θ_r according to global coordinate system $\left[x^{(e)}, y^{(e)}\right]$. There is assumption, that position of environment landmarks in global coordinate system is known, therefore environment map is known. Coordinate system of environment map (Figure 1) is global coordinate system and it is dedicated by axis $x^{(e)}$ and $y^{(e)}$. This global coordinate system differs from local robotic system, which is by analogy dedicated by axis $x^{(r)}$ and $y^{(r)}$.

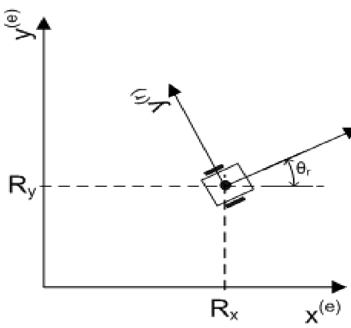

Figure 1 Position of mobile robot assigned by vector $p = (R_x, R_y)$ and rotation θ_r in respect of global coordinate system $\left[x^{(e)}, y^{(e)}\right]$.

Environment mark L can be defined in both coordinate systems. Vector $l^{(e)}$ defines mark in global coordinate system and vector $l^{(r)}$ defines mark in local coordinate system (Figure 2).

Position of robot is defined in global coordinate system $\left[x^{(e)}, y^{(e)}\right]$ by vector $p = (R_x, R_y)$. Vector p connects

Contact authors: Ladislav Jurišica, František Duchoň
E-mail: ladislav.jurisica@stuba.sk
frantisek.duchon@stuba.sk

ISSN 1590-8844
International Journal of Mechanics and Control, Vol. 10, No. 02, 2009

the beginnings of coordinate systems $\left[x^{(e)}, y^{(e)}\right]$ and $\left[x^{(r)}, y^{(r)}\right]$ [5]. Robot is oriented in direction of axis $x^{(r)}$.

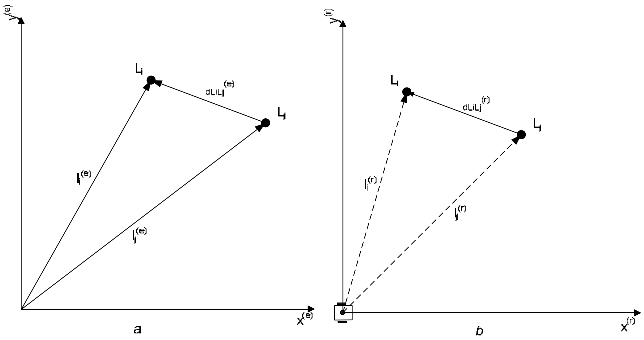

Figure 2 Landmarks L_i a L_j in:

a) global coordinate system with vectors $l_i^{(e)}$ and $l_j^{(e)}$

b) local coordinate system with vectors $l_i^{(r)}$ and $l_j^{(r)}$

Orientation of robot is expressed by angle θ_r, which is angle between axis $x^{(e)}$ of global coordinate system and axis $x^{(r)}$ of local coordinate system.

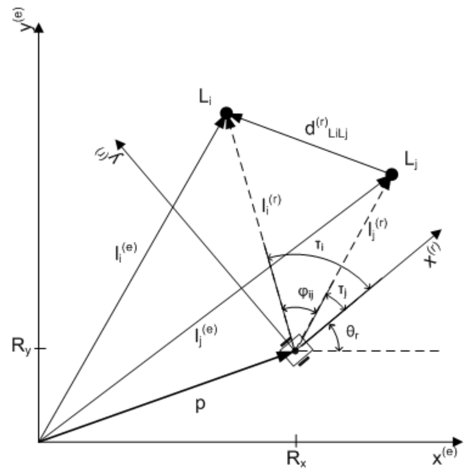

Figure 3 Environment map expressed with global and local coordinate system. Both vectors, $l_i^{(e)}$ in global coordinate system and $l_i^{(r)}$ in local coordinate system, express position of mark L_i. Position of robot is expressed by vector p and angle θ_r.

Figure 3 describes relations between global and local coordinate system by means of a positional vector $l_i^{(e)},...l_n^{(e)}$ expressed in global coordinate system. Robot measures position (distance and angle) of each environment mark considering its orientation towards global coordinate system. τ_i stand for angle between environment landmarks $l_i^{(r)}$ for $i = 1,...,n$ and axis $x^{(r)}$, which designates robot orientation:

$$\tau_i = \angle(l_i^{(r)}, x^{(r)}) \tag{1}$$

Angle obtained by measure of one environment mark relatively to another environment mark is called view angle of two environment landmarks and is described:

$$\varphi_{ij} = \tau_i - \tau_j \tag{2}$$

If angle θ_r is equal to zero, vector between two landmarks L_i and L_j can be expressed as (Figure 3):

$$d_{LiLj}^{(r)} = l_i^{(r)} - l_j^{(r)} = d_{LiLj}^{(e)} = l_i^{(e)} - l_j^{(e)} \tag{3}$$

If angle θ_r isn't equal to zero, there must be applied conversion between global and local coordinate system. For $n+1$ environment landmarks can be formulated conclusion:

If positions $l_1^{(e)},...,l_n^{(e)}$ of environment landmarks are known in global coordinate system and measured angles between landmarks $\tau_1,...,\tau_n$ are also known, position p and orientation θ_r of robot in environment can be estimated.

3 ASSIGNATION OF ABSOLUTE MOBILE ROBOT POSITION BY TRIANGULATION

3.1 TWO POINTS TRIANGULATION

If view angle φ_{ij}, which represents angle between landmarks L_i a L_j and distance dL_iL_k between both landmarks are known in unknown robot position, then relative position p of robot can be assigned on circumference of circle, which connects landmarks L_i and L_j (Figure 4).

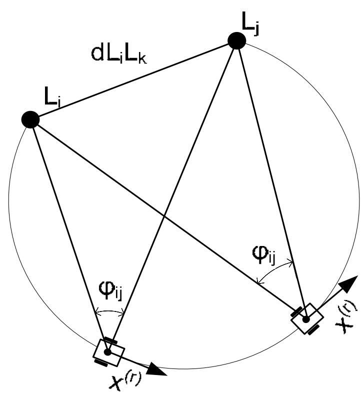

Figure 4 Triangulation with two landmarks L_i and L_j. Position of robot is on circle, which connect these both landmarks. Robot is orientated in direction of axis $x^{(r)}$.

3.2 THREE POINTS TRIANGULATION

Third mark L_k is needed for outright definition of position p. Position p is then defined by intersection of circle circumscribed by landmarks L_i and L_j and circle circumscribed by landmarks L_j and L_k (Figure 5).

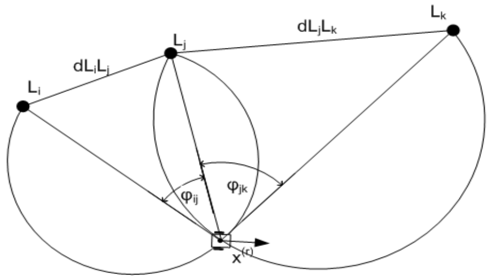

Figure 5 Triangulation with three landmarks. Position of robot is clear and specified by node of both circles.

However position p is not clearly defined in case, when landmarks L_i, L_j and L_k are not situated at the same circle (Figure 6). One method of position p calculation is to describe both circles analytically and then point of intersection can be dedicated. If angles and distances between the landmarks are dedicated, law of cosine can be used to calculate radius of each circle. Coordinates of circle centers can be calculated from coordinates of the landmarks L_i, L_j and L_k. Directly if position p is known, orientation of the robot is known too.

Other method of position p calculation consists in calculation of distances between robot and environment landmarks. This approach is preferable to antecedent, if data about environment landmarks are loaded by some errors. Besides using n landmarks, $\binom{n}{3}$ combinations of three landmarks is obtained, which leads to system of predefined equations. These equations can be solved by method of smallest squares. Estimated position of robot in environment is then calculated as average of partial calculations of combinations between three used environment landmarks.

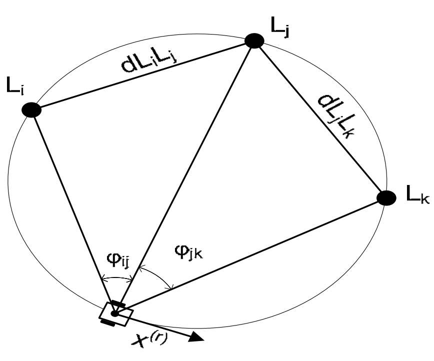

Figure 6 Triangulation with three landmarks lying on one circle. Position of robot is not clear.

With usage of cosine law, relation between two landmarks L_i and L_j can be described as:

$$\left|dL_iL_j\right|^2 = \left|l_i^{(r)}\right|^2 + \left|l_j^{(r)}\right|^2 - 2\left|l_i^{(r)}\right|\left|l_j^{(r)}\right|\cos\varphi_{ij} \tag{4}$$

Where $\left|dL_iL_j\right|$ is known distance between landmarks L_i and L_j, φ_{ij} is view angle between landmarks L_i and L_j considering robot position and $\left|l_i^{(r)}\right|$, $\left|l_j^{(r)}\right|$ are distances of environment landmarks (Figure 7). Angle φ_{ij} is calculated from measured angles τ_i and τ_j (2) (Figure 3). With usage of cosine law on each possible couple of landmarks, system of predefined equations is obtained, which can be solved by method of smallest squares. For case on Figure 5 can be formed system of equations:

$$\begin{aligned}
\left|dL_iL_j\right|^2 &= \left|l_i^{(r)}\right|^2 + \left|l_j^{(r)}\right|^2 - 2\left|l_i^{(r)}\right|\left|l_j^{(r)}\right|\cos\varphi_{ij} \\
\left|dL_iL_k\right|^2 &= \left|l_i^{(r)}\right|^2 + \left|l_k^{(r)}\right|^2 - 2\left|l_i^{(r)}\right|\left|l_k^{(r)}\right|\cos\varphi_{ik} \\
\left|dL_jL_k\right|^2 &= \left|l_j^{(r)}\right|^2 + \left|l_k^{(r)}\right|^2 - 2\left|l_j^{(r)}\right|\left|l_k^{(r)}\right|\cos\varphi_{jk}
\end{aligned} \tag{5}$$

Solution of this system of equations are distances of environment landmarks from robot positions, thus in this case distances of entities $\left|l_i^{(r)}\right|$, $|\, l_j^{(r)}\,|$, $|\, l_k^{(r)}\,|$. In order to determinate robot position is needed to solve system of equations:

$$\begin{aligned}
\left|l_i^{(r)}\right|^2 &= \left(Lx_i - R_x\right)^2 + \left(Ly_i - R_y\right)^2 \\
\left|l_j^{(r)}\right|^2 &= \left(Lx_j - R_x\right)^2 + \left(Ly_j - R_y\right)^2 \\
\left|l_k^{(r)}\right|^2 &= \left(Lx_k - R_x\right)^2 + \left(Ly_k - R_y\right)^2
\end{aligned} \tag{6}$$

With subtraction of second and third equation from the first one, two equations with two unknown variables R_x and R_y are obtained:

$$\begin{aligned}
\left|l_i^{(r)}\right|^2 - \left|l_j^{(r)}\right|^2 &= Lx_i^2 - Lx_j^2 + 2R_x\left(x_j - x_i\right) + y_i^2 - y_j^2 + 2R_y\left(y_j - y_i\right) \\
\left|l_i^{(r)}\right|^2 - \left|l_k^{(r)}\right|^2 &= Lx_i^2 - Lx_k^2 + 2R_x\left(x_k - x_i\right) + y_i^2 - y_k^2 + 2R_y\left(y_k - y_i\right)
\end{aligned} \tag{7}$$

With solution of these nonlinear equations robot position $p = (R_x, R_y)$ is obtained.

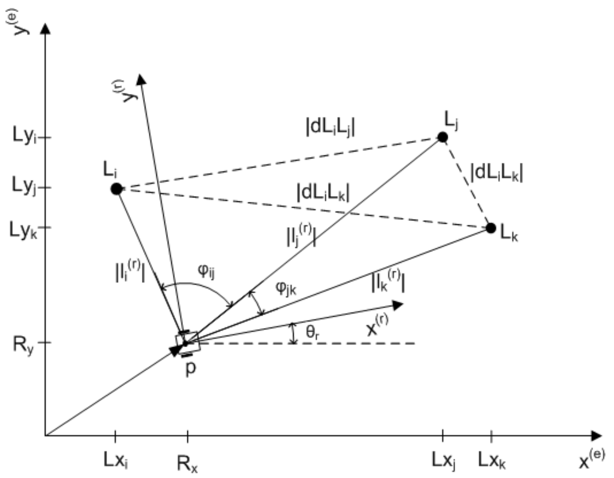

Figure 7 Relations between environment landmarks for position assignation using law of cosine.

In system of equations (5) $\left|l_i^{(r)}\right|$, $|\ l_j^{(r)}\ |$, $|\ l_k^{(r)}\ |$ are distances of the landmarks from robot position, which has been solved from system of equations (6), (R_x, R_y) present coordinates of robot position in Cartesian coordinate system and $(Lx_i\ , Ly_i\ )$, $(Lx_j\ , Ly_j\ ), (Lx_k\ , Ly_k)$ are coordinates of landmarks L_i, L_j and L_k in Cartesian coordinate system. With solving system of equations (6) is possible to acquire robot position in Cartesian coordinates, but only in that case, when Cartesian coordinates of the environment landmarks are also known. If position p is defined, then orientation θ can be calculated by simple calculation of vector $l_i^{(r)} = l_i^{(e)} - p$ for some i and then angle θ_r can be assigned by relation:

$$\theta_r = \angle(l_i^{(r)}, x^{(e)}) - \tau_i \tag{8}$$

4 ASSIGNATION OF RELATIVE DISPLACEMENT

When calculating relative displacement of mobile robot, there is assumption, that environment map is unknown. In this case, relative displacement ε is calculated between two positions of mobile robot in environment considering two environment landmarks. Robot position $p = (R_x, R_y)$ will be designated relatively to coordinate system $\left[x^{(l)}, y^{(l)}\right]$, which is defined by two environment landmarks (Figure 8). First mark represents beginning of coordinate system and a second mark defines x or y axis. Undefined axis is defined by rules of right-handed Cartesian coordinate system.

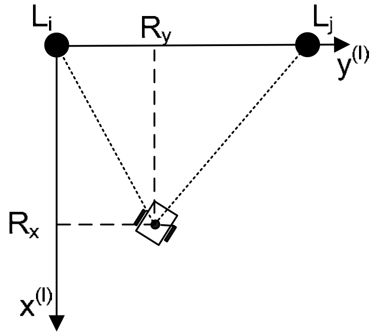

Figure 8 Definition of coordinate system described by landmarks L_i and L_j .

Basic principle of this method is calculation of distance dP_1, dP_2 in two different robot positions P_1 and P_2. Model situation can be seen on Figure 9. There is assumption, that distances between robot and landmarks $\mathrm{dP_1L_1}$, $\mathrm{dP_1L_2}$, $\mathrm{dP_2L_1}$, $\mathrm{dP_2L_2}$ and angles between robot and landmarks $\varphi_{\mathrm{P_1L_1L_2}}$, $\varphi_{\mathrm{P_2L_1L_2}}$ in both robot positions are known.

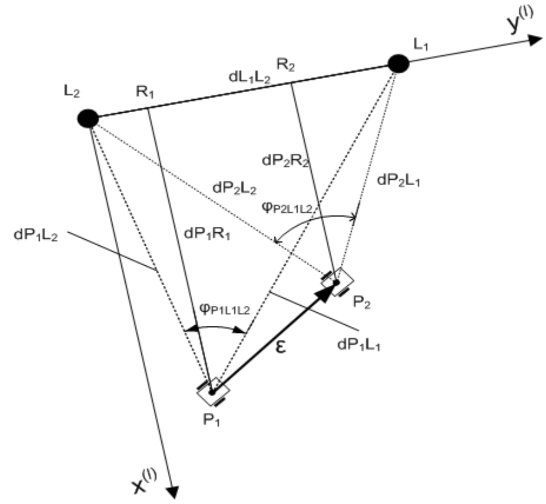

Figure 9 Coordinate system described by landmarks L_1 and L_2, relations between landmarks and robot in both positions.

Law of sine states (Figure 10):
For each triangle ABC with inner angles α, β, γ and with sides a, b, c holds:

$$\frac{a}{\sin\alpha} = \frac{b}{\sin\beta} = \frac{c}{\sin\gamma} \tag{9}$$

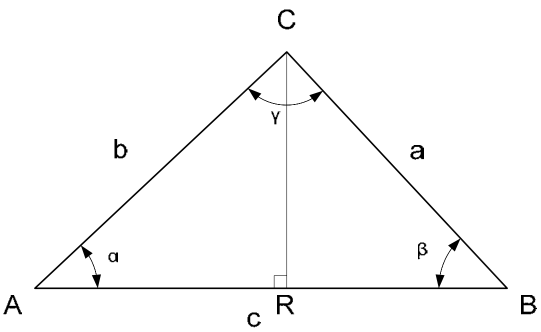

Figure 10 Law of sine.

If distance AB and angle γ are known, from the equation (9) can be size of angles α and β expressed as:

$$\alpha = \arcsin\left(\frac{BC.\sin\gamma}{AB}\right)$$
$$\beta = \arcsin\left(\frac{AC.\sin\gamma}{AB}\right) \quad (10)$$

If angles α and β are known, we can express length RC as:

$$RC=\left(\frac{AB.\sin\alpha.\sin\beta}{\sin\gamma}\right) \quad (11)$$

Lengths AR and BR can be then calculated by application of Pythagorean Theorem:

$$AR=\sqrt{AC^2-RC^2}$$
$$BR=\sqrt{BC^2-RC^2} \quad (12)$$

From the Figure 11 there is analogy, thus for the position P_1 holds:

$\mathrm{A}=L_1$, $\mathrm{B}=L_2$, $\mathrm{C}=\mathrm{P}_1$, $\alpha=\alpha_{P1}$, $\beta=\beta_{P1}$

thus:

$$\mathrm{AB}=\mathrm{d}L_1L_2, \qquad \mathrm{AC}=\mathrm{dP_1L_1}, \qquad \mathrm{BC}=\mathrm{dP_1L_2}$$
$$\gamma=\varphi_{\mathrm{P_1L_1L_2}} \quad (13)$$

Moreover for the position P2 holds :

$\mathrm{A}=L_1$, $\mathrm{B}=L_2$, $\mathrm{C}=\mathrm{P}_2$, $\alpha=\alpha_{P2}$, $\beta=\beta_{P2}$

thus:

$$\mathrm{AB}=\mathrm{d}L_1L_2, \qquad \mathrm{AC}=\mathrm{dP_2L_1}, \qquad \mathrm{BC}=\mathrm{dP_2L_2}$$
$$\gamma=\varphi_{\mathrm{P_2L_1L_2}} \quad (14)$$

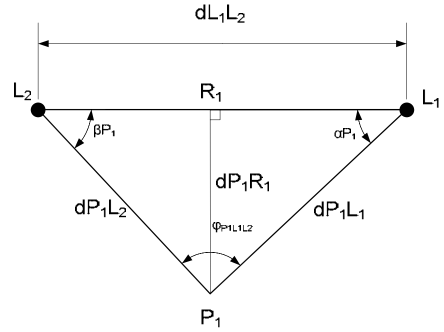

Figure 11 Law of sine application.

From the equations (10), (11), (12) and from the analogies (13) and (14) can be expressed these equations.

For angles α_{P1}, β_{P1} in position P_1 and for angles α_{P2} α_{P2} in position P_2 holds:

$$\alpha_{P1}=\arcsin\left(\frac{\mathrm{dP_1L_2}.\sin\varphi_{\mathrm{P_1L_1L_2}}}{\mathrm{d}L_1L_2}\right)$$
$$\beta_{P1}=\arcsin\left(\frac{\mathrm{dP_1L_1}.\sin\varphi_{\mathrm{P_1L_1L_2}}}{\mathrm{d}L_1L_2}\right)$$
$$\alpha_{P2}=\arcsin\left(\frac{\mathrm{dP_2L_2}.\sin\varphi_{\mathrm{P_2L_1L_2}}}{\mathrm{d}L_1L_2}\right)$$
$$\beta_{P2}=\arcsin\left(\frac{\mathrm{dP_2L_1}.\sin\varphi_{\mathrm{P_2L_1L_2}}}{\mathrm{d}L_1L_2}\right) \quad (15)$$

Orthographic distances between environment landmarks L_1 and L_2 in robot positions P_1 and P_2 can be calculated as:

$$\mathrm{dP_1R_1}=\left(\frac{\mathrm{d}L_1L_2.\sin\alpha_{P1}.\sin\beta_{P1}}{\sin\varphi_{\mathrm{P_1L_1L_2}}}\right)$$
$$\mathrm{dP_2R_2}=\left(\frac{\mathrm{d}L_1L_2.\sin\alpha_{P2}.\sin\beta_{P2}}{\sin\varphi_{\mathrm{P_2L_1L_2}}}\right) \quad (16)$$

Lengths L_1R_1, L_2R_1 in position P_1 and lengths L_1R_2, L_1R_2 in position P_2 can be calculated by application of Pythagorean Theorem:

$$L_1R_1=\sqrt{\mathrm{dP_1L_1}^2-\mathrm{dP_1R_1}^2}$$
$$L_2R_1=\sqrt{\mathrm{dP_1L_2}^2-\mathrm{dP_1R_1}^2} \quad (17)$$

ISSN 1590-8844
International Journal of Mechanics and Control, Vol. 10, No. 02, 2009

$$L_1R_2 = \sqrt{\mathrm{dP_2L_1}^2 - \mathrm{dP_2R_2}^2}$$

$$L_2R_2 = \sqrt{\mathrm{dP_2L_2}^2 - \mathrm{dP_2R_2}^2}$$

Relative displacement ε of robot between positions $\mathrm{P_1}$ and $\mathrm{P_2}$ can be calculated (Figure 12):
For x and y compound:

$$\varepsilon_x = \mathrm{dP_1}R_1 - \mathrm{dP_2}R_2$$
$$\varepsilon_y = \mathrm{L_1}R_1 - \mathrm{L_1}R_2 \tag{18}$$

Thus relative displacement ε can be calculated by application of Pythagorean Theorem:

$$\varepsilon = \sqrt{\varepsilon_x^{\;2} + \varepsilon_y^2} \tag{19}$$

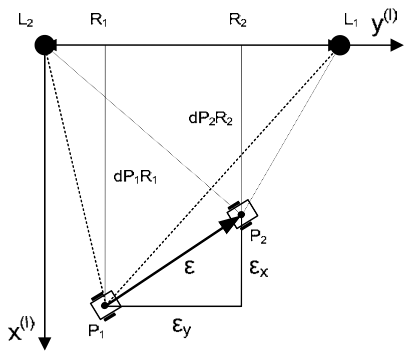

Figure 12 Assignation of relative movement ε

5 SIMULATION TESTS

These tests were used to verify triangulation methods. Inputs in these tests were directly defined, such as position of mobile robot or positions of landmarks. Thus the verification consisted of computation of robot position from these inputs using triangulation methods described in chapter 3 and 4. First simulated situation was estimation of mobile robot position with knowledge of environment landmarks, whereby minimally three were visible every time. Arrangement of environment landmarks can be seen on Figure 13. Usage of artificial environment landmarks was considered, because the aim was to test triangulation methods, not to design landmarks detection. So there is assumption, that landmarks are successfully detected and identified. Robot can move only in area bounded by spotty line. In this area are at least three environment landmarks visible every time. Localization can be realized, i.e. robot position $p = (R_x, R_y)$ and orientation θ_r can be dedicated.

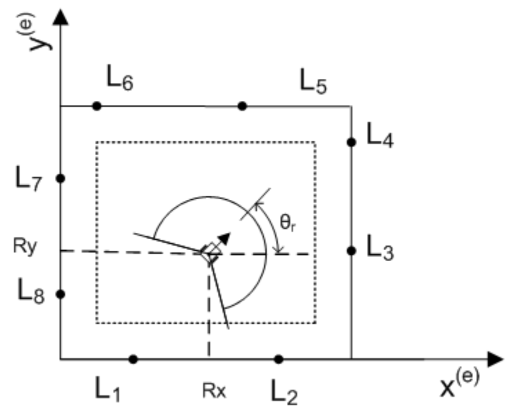

Figure 13 Arrangement of environment landmarks

In this simulation example were real sensorial system tested. In this case it means, that robot detects landmarks in view angle of its laser scanner [4] (240º). Inputs in this test were position and orientation of robot and test resides in computation of its position and orientation considering environment landmarks and with usage of triangulation methods. Each detected mark has corresponding position in global coordinate system. Now, positions of landmarks in global coordinate system, distances and angles between landmarks and robot are known. At these assumptions we can solve estimation of absolute robot localization in environment. Let's consider specific situation as seen on Figure 14. Inputs are $p = (R_x, R_y) = (20.50, 19.15)$ a $\theta_r = 130.9°$.

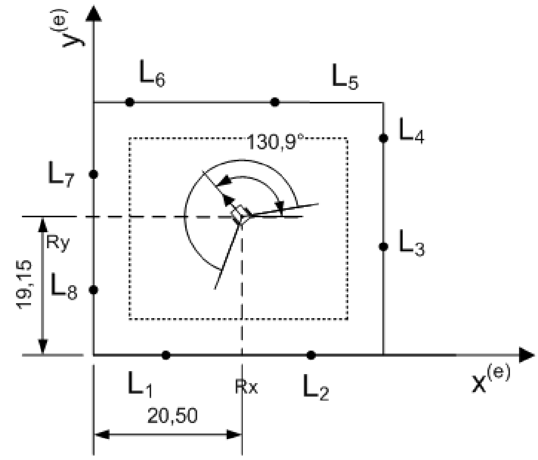

Figure 14 Scheme for calculating the position and rotation of robot.

By application of equations from the chapter 3 were obtained these results (Figure 15):
$p = (R_x, R_y) = (20.768, 19.506)$ a $\theta_r = 131.31°$

This algorithm of absolute mobile robot estimation calculates position correctly in cases, where are fulfilled all assumptions. When robot finds itself beyond spotty line, it can become, that at least three landmarks will not be seen, so robot can't localize itself in environment.

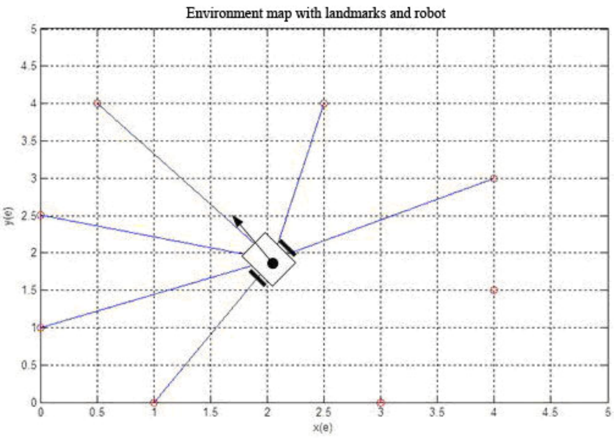

Figure 15 Portrayal of robot position assigned by environment landmarks triangulation in Matlab.

Second simulated situation assumes no-knowledge of environment, or more precisely relations between landmarks and their positions in environment map are not known. The only assumption is detection of two identical environment landmarks in both robot positions. Displacement of robot can be then calculated by equations listed in chapter 4. There is assumption, that robot forms triangle with base given by environment landmarks every time. Whereby orthographic plan of robot position on base L1L2 lie between landmarks L_1 and L_2 every time (Figure 16).

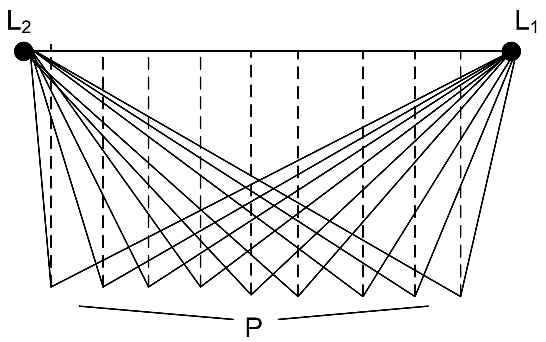

Figure 16 Assumed arrangements of landmarks and robot.

These times were inputs the data, which will return laser scanner [3], angle and distance of detected landmarks. Test situation is on Figure 17. With simulation in Matlab [2] were obtained these results:

$\varepsilon = 282.3681$

$p_1 = (R_{x1}, R_{y1}) = (529.2029, 99.6318)$

$p_2 = (R_{x2}, R_{y2}) = (371.8666, 334.2383)$

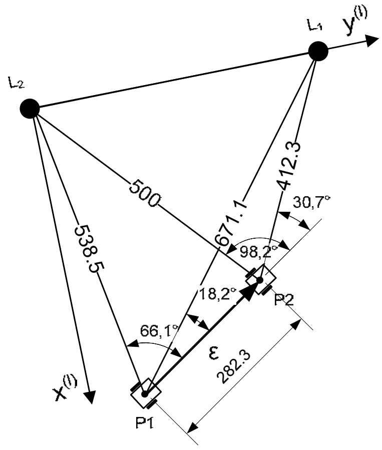

Figure 17 Scheme of simulated example for calculation of relative movement between two positions of robot.

6 VERIFICATION ON REAL DEVICE

Verification on real device consists of calculation of relative displacement/rotation of mobile robot between two positions of this robot. For the verification were used real data from laser scanner and considered these two situations:

1. Movement forwards by 17 cm
2. Movement forwards by 28 cm and consecutive rotation by 10°

Our used scanner was a laser scanner from Hokuyo URG-04LX, which has 0.36° angular resolution and 240° area scanning range. Final of measured data is 768x2 matrixes, where first column represents scanning step and second represents measured distance. Rows represent measured distances for specified scanning steps. Relation between scanning step and angle of scanning can be seen on Figure 18. Step 384 represents angle 0º. Steps 44 and 726 represent angle -120 º and 120º. Scanner measure distances from 20mm to 4094mm. Distances smaller than 20mm represent internal error code of scanner.

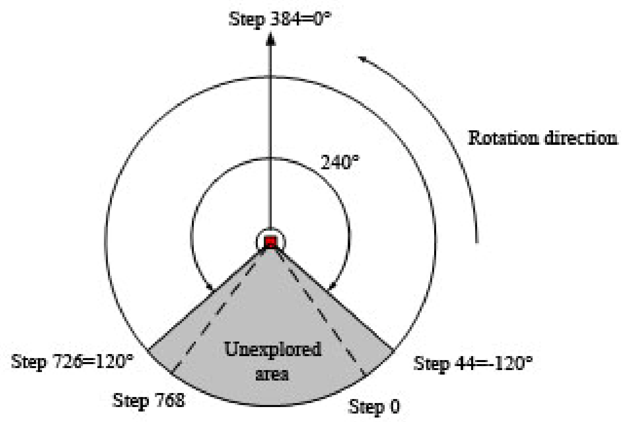

Figure 18 Angle representations of data from real laser scanner.

Scheme of algorithms for assignation of relative displacement in position of mobile robot using detection of environment landmarks can be viewed on Figure 19.

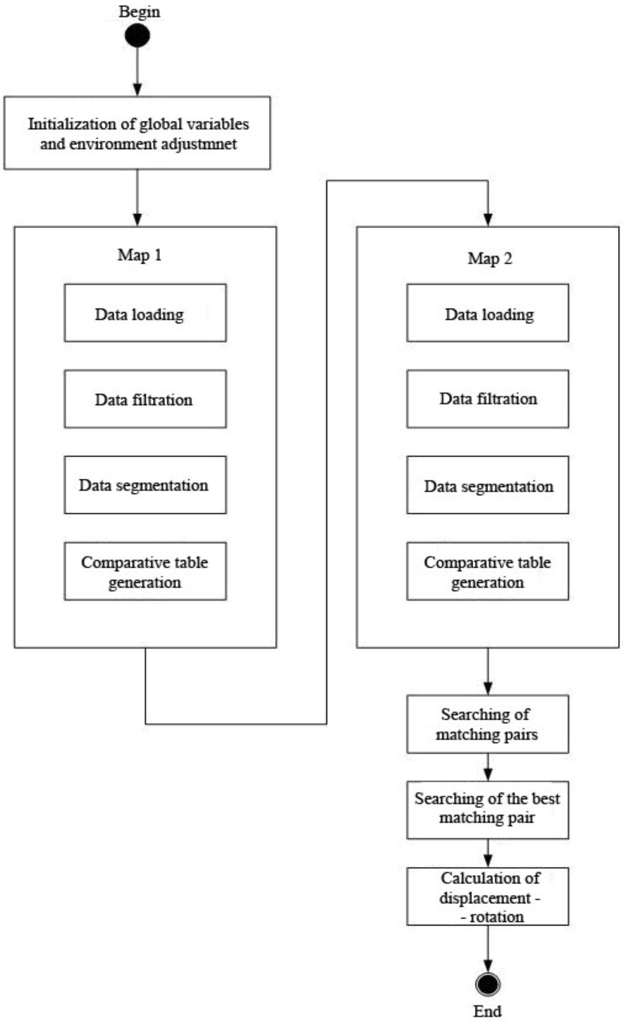

Figure 19 Algorithm scheme.

If detection of environment landmarks is correctly performed, it is also needed to assign match between two subsequent environment maps. Matching between two maps uses relations between environment landmarks, which are independent from robot position and orientation. These relations between detected landmarks represent their common properties as distance and angle between them.

First experiment was method, which compares mutual relations between landmarks. Principle of this method is generation of all the vector pairs from real extremes in environment map. Otherwise this method returns correct matching, but only in case of small amount of real extremes. When environment maps contain a lot of detected real extremes, a lot of combinations are generated. This leads to massive computing time. So the new matching method must be invented.

New way of matching consists of array generation. This array stores couples of consecutive vectors, which consist of real extremes (Figure 20). By this way is principle of matching using mutual relations between landmarks conserved and computation time is small.

Mentioned array generation uses comparative table. Aim of this comparative table is to gather already received information and generation all new information required for matching real extremes in environment maps. Comparative table is generated for each map. Comparative table (Figure 21) by itself consists of rows – couple of vectors, where each column represents attribute of latter comparison (eventually indexing). First three columns of table represent indexes of points, which creates vectors (1 – first point of real extreme from first vector, 2 – last point of real extreme from first vector and first point of real extreme from second vector, 3 – last point of real extreme from second vector), additional two columns represent length of vectors (4 – length of first vector, 5 – length of second vector). Last column represents angle between vectors.

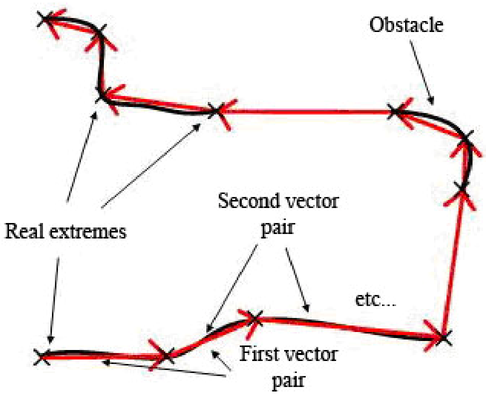

Figure 20 Principle of generating comparative table.

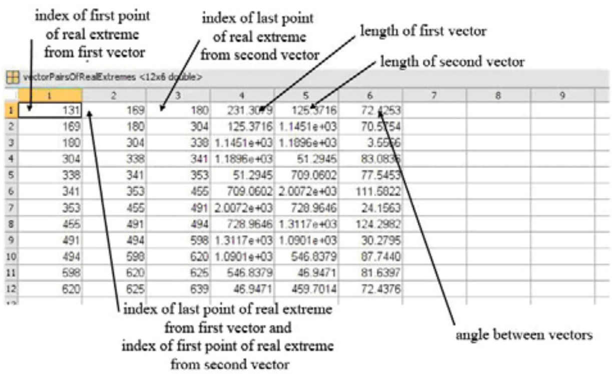

	1	2	3	4	5	6	7	8	9
1	131	169	180	231.30[illegible]9	125.3716	72.4253			
2	169	180	304	125.3716	1.1451e+03	70.5754			
3	180	304	338	1.1451e+03	1.1896e+03	3.55[illegible]6			
4	304	338	341	1.1896e+03	51.2945	83.083[illegible]			
5	338	341	353	51.2945	709.0602	77.5453			
6	341	353	455	709.0602	2.0072e+03	111.5822			
7	353	455	491	2.0072e+03	728.9646	24.1563			
8	455	491	494	728.9646	1.3117e+03	124.2982			
9	491	494	598	1.3117e+03	1.0901e+03	30.2795			
10	494	598	620	1.0901e+03	546.8379	87.7440			
11	598	620	625	546.8379	46.9471	81.6397			
12	620	625	639	46.9471	459.7014	72.4376			

Figure 21 Example of comparative table.

If tables are generated for both consecutive maps, it is possible to find match. Records from first comparative table are combined with records from second comparative table. If there is a match in length of first vector, in length of second vector and in angle between these two vectors, it is concerned as three real extremes match (Figure 22). Result is written to final matching table (Figure 23).

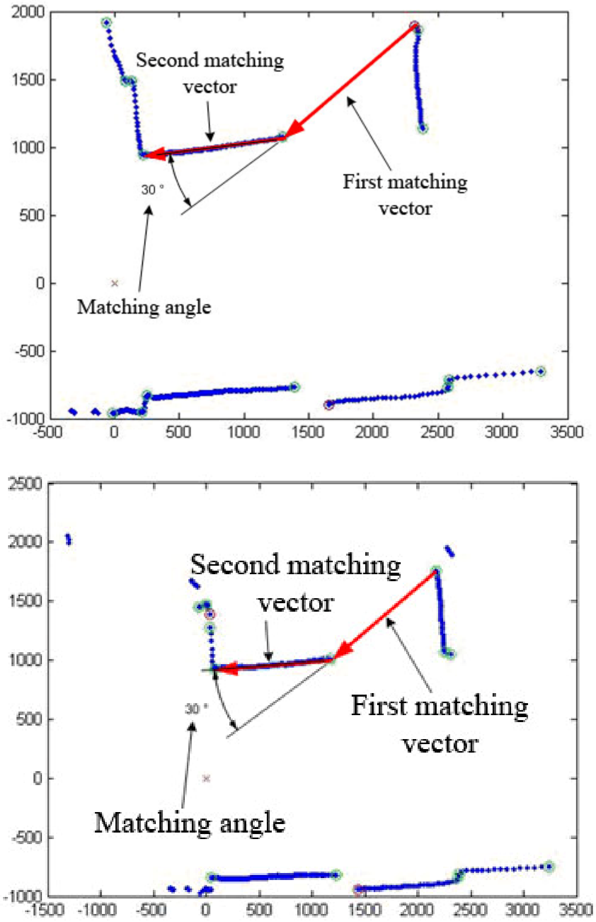

Figure 22 Pair of vectors in map number 1 and number 2.

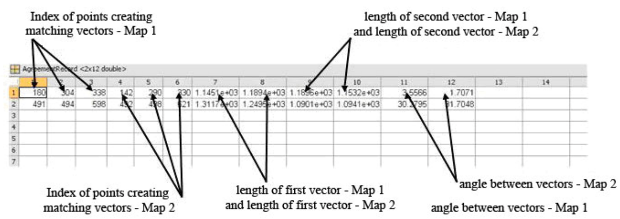

Figure 23 Final matching table.

At searching of matching pairs is possible to use property of probable matching points, i.e. points, which are situated directly before and after extreme. They can be used for edge detection of objects. Function searching of matching - GetMapPairs uses this property. Concretely this property is utilized in function GetOppositeRealExtremeInMap2 used in GetMapPairs. This searching consists of each vector combination with every remaining vector. Difference is that, now are not used every detected vectors, but just known pairs of matching (contained in array *MapPairs*).

If all matches are designated (Figure 24), main task is to select the best one. The best match provides the best result. Conditions for best match are: First point must be situated at left side of robot, second point at right side (Figure 25). The best match is assigned by the best rate of distances and angles of these points.

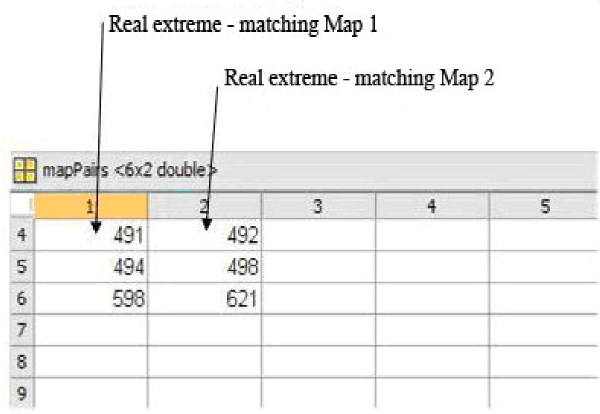

Figure 24 Matching of real extremes in couple of maps.

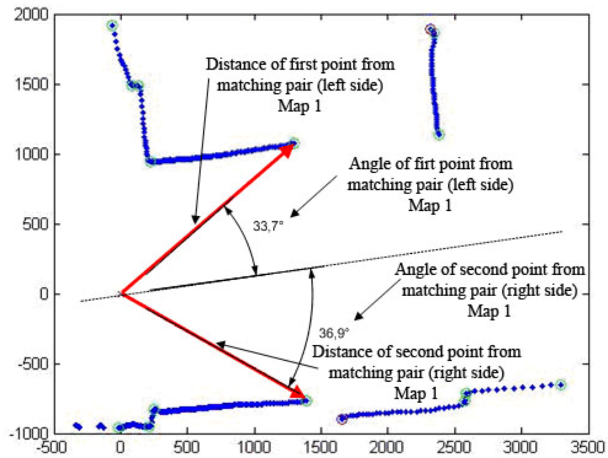

Figure 25 Conditions for the best matching.

If the best match is dedicated, i.e. indexes of matched landmarks, relative displacement can be calculated, eventually rotation of robot between two robot positions. For calculation is used function GetRobotMovementRelativeChange, whose input is array of the best match. Values of displacement/rotation are calculated by equations described in chapter 4. There is assumption, that robot cannot simultaneously rotate and displace in short intervals, therefore if it is calculated relative displacement lower than parameter robotInStopModeDistance (in our case empirically set on 40mm) it is possible to calculate angle rotation. This angle is calculated as rotation of environment mark from map 1 to matched environment mark in map 2. Function returns as result value of relative displacement ε between two robot positions, eventually if robot just turns, function returns angle rotation in degrees.

7 RESULTS FROM REAL DEVICE

Movement forwards - 17cm

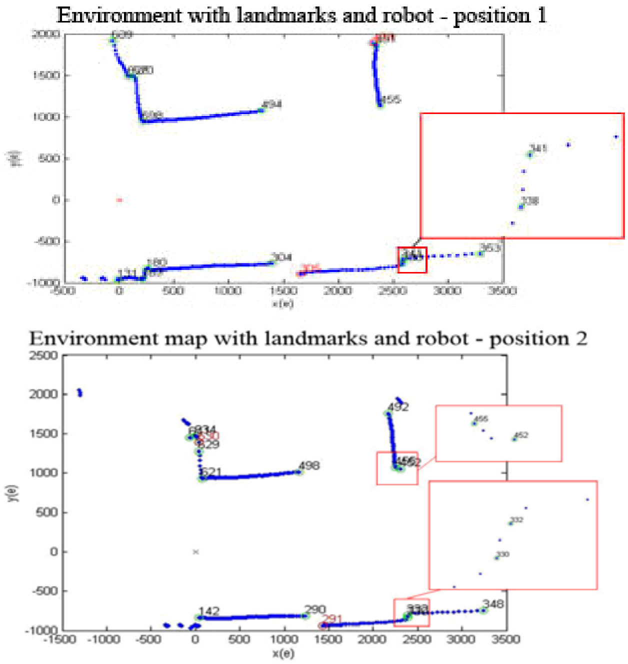

Figure 26 Maps for movement forwards - 17 cm.

Result (Figure 26):
$\varepsilon = 16.31cm$ and $\theta_r = 0°$

Movement forwards - 28cm

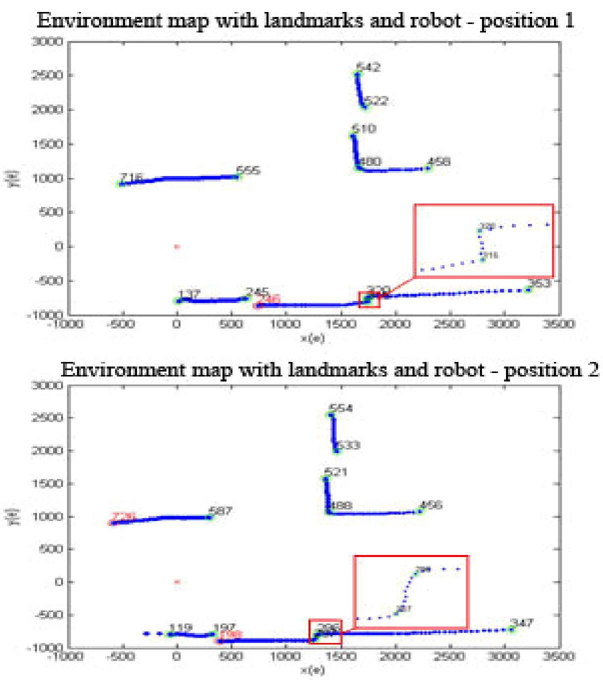

Figure 27 Maps for movement forwards - 28 cm.

Result (Figure 27):
$\varepsilon = 28.3cm$ a $\theta_r = 0°$

Robot rotation - +10°

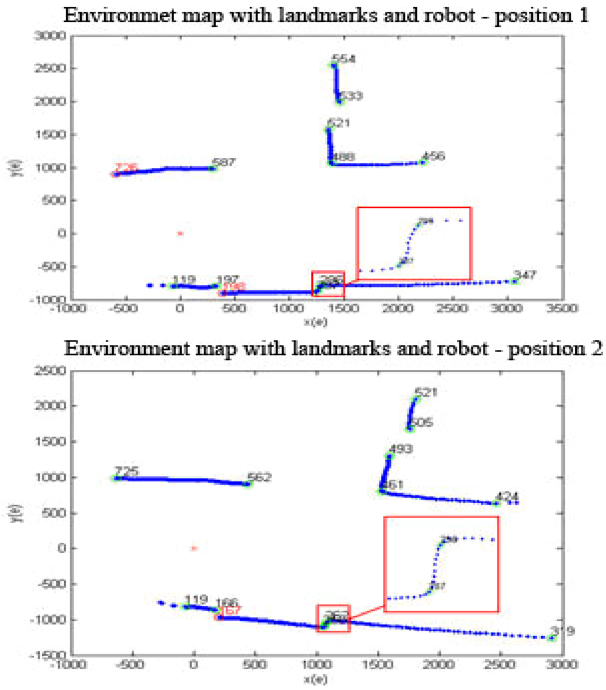

Figure 28 Maps for rotation of +10°.

Result (Figure 28):
$\varepsilon = 0.185cm$ a $\theta_r = 10.98°$

8 CONCLUSION

Suggested methods give possibilities to calculate relative position of mobile robot in environment on the ground of detected artificial landmarks or natural properties of objects. These methods allow imprinting with errors, that are generated at odometry and thereby they increase quality of information about robot position in environment.

ACKNOWLEDGMENT

This work was supported by MS SR under the contract VEGA 1/0690/09.

REFERENCES

[1] Betke M., Gurvits K., *Mobile Robot Localization Using Landmarks*, IEEE Transactions on Robotics and Automation, vol. 13, No. 2, pp. 251 – 263, 1997.

[2] Matlab Documentation, http://www.mathworks.com/access/helpdesk/help/techdoc/matlab.shtml

[3] Kilpelä A., *Pulsed time-of-flight laser range finder techniques for fast, high precision measurement applications*, Department of Electrical and Information Engineering, University of Oulu, Finland, 2004

[4] Koskinen M., Kostamovaara J., Myllylä R., *Comparison of the continuous wave and pulsed time-of-flight laser rangefinding techniques*, Illuminationd and Image Sensing for Machine Vision, Proc. SPIE Vol. 1614, pp. 296-305.

[5] Typiak A., *Use of laser rangefinder to detecting in surroundings of mobile robot the obstacles*, The 25th International Symposium on Automation and Robotics in Construction, June 26-29, 2008.

[6] Rodina J., Hubinský P., Stability control design of segway like differential drive by using MEMS sensor, *Proc. Of Conference Modeling of the mechanical and mechatronic systems*, Zemplínska Šírava, Slovakia, pp. 483 – 487, September 22-24, 2009.

ISSN 1590-8844
International Journal of Mechanics and Control, Vol. 10, No. 02, 2009

DESIGN AND SIMULATION OF CASSINO HEXAPODE WALKING MACHINE

G. Carbone*, M. Suciu **, M. Ceccarelli*, D. Pisla**

* University of Cassino Via Di Biasio 43, 03043 Cassino (FR), Italy

** Technical University of Cluj-Napoca Str. Daicoviciu 15, 400020 Cluj-Napoca (CJ), Romania

ABSTRACT

In this paper design and simulation of enhancements are presented for Cassino Hexapode Walking Machine. Simulation results are reported from kinematic and dynamic analyses of a suitable model for the current design and other proposed improvements. Some tests are shown to discuss main characteristics and problems for the proposed solutions.

Keywords: Walking Machines, Hexapod Robots, Simulation, Design, Experimental Validations

1 INTRODUCTION

Walking machines have been attempted since the beginning of the technology of transportation machinery with the aim to overpass the limits of wheeled systems by looking at legged solutions in nature. But only since the last part of the 20-th century very efficient walking machines have been conceived, designed, and built with good performances that are suitable for practical applications carrying significant payload with relevant flexibility and versatility [1].

A key feature of many robots that are intended to perform useful work in any environment is that they must be able to navigate unassisted both indoor and outdoor. Therefore legged locomotion is of fundamental importance with both power and task autonomy as mobility is required. Only robots that can move freely in real-world environments without human assistance are suitable candidates for real-world tasks.

Bipeds, quadrupeds, hexapods, and octopods are all potentially capable of performing suitable movements. However, bipeds and quadrupeds need to operate with dynamic control, and six and eight legged robots are naturally stable, even while in motion. The additional two legs in octopods can be considered for a redundant solution, and they make the robot heavier and more complex, by requiring more power and computational control. Walking robots with more than 3-DOFs per leg can be considered not convenient, since they require extra amounts of control and provide unnecessary additional joints.

An interesting example of a hexapod robot is The walking forest machine in [2]. This machine adapts automatically to the forest floor. Moving on six articulated legs, the robot moves forward and backward, sideways and diagonally. It can also turn in place and step over obstacles. Depending on the irregularity of the terrain, the operator can adjust both the ground clearance of the machine and height of each step as pointed out in [2]. The machine's control center is an intelligent computer system that controls all walking functions, including the direction of movement, the traveling speed, the step height and gait, and the ground clearance. To further optimize machine operation, Timberjack's Total Machine Control system (TMC) regulates the functions of machine's loader and engine. All control systems are designed for easy of use. The operator-friendly controls are incorporated in a single joystick.

Another example of a successful hexapod robot is the TUM Walking Machine. Dr. Friedrich Pfeiffer at Technische Universität München began work on the TUM Walking Machine in 1991 [3]. This robot is based on the structure of stick insect and uses a form of cruse-control for leg coordination. The TUM Walking Machine uses distributed leg control so that each leg may be self-regulating with influences from adjacent legs, as pointed out in [3]. In fact, "A leg is hindered from starting its return stroke while its posterior leg is performing a return stroke", [3], and is applied to contra lateral adjacent legs. Additionally, a leg is

Contact author: G. Carbone[1], M. Suciu[2]

[1] University of Cassino
Via Di Biasio 43, 03043 Cassino (FR), Italy.
[2] Technical University of Cluj-Napoca
Str. Daicoviciu 15, 400020 Cluj-Napoca (CJ), Romania.

prevented from entering the swing phase while any adjacent neighboring leg is still in swing motion.
Generally, multi legged systems can be slow and more difficult to design and operate as compared to machines that are equipped with crawlers or wheels. But, legged robots are more suitable for rough terrain, where obstacles of any size can appear. In fact, the use of wheels or crawlers limits the size of the obstacle that can be climbed, to half the diameter of the wheels. On the contrary, legged machines can overcome obstacles that are comparable with the size of the machine leg. Thus, the types of walking robots may range from crawler devices to hybrid walking machines with a set of wheels. The wheels are usually used to enhance the speed when walking on flat terrain.
The advantage of the legged systems over the wheeled systems can be understood by looking at their kinematic capability and static performance. In addition, legged motion can easily avoid large obstacles and any kind of direction change can be performed more quickly in less space. They can also move sideways and can represent a better approach for moving in environments, where the surface has less adherence (on the moon for instance, where the lower gravity causes a friction reduction).
In this paper, problems and solutions are investigated through numerical simulation in order to do the necessary design and operation enhancements of the Cassino Hexapod Walking Machine for a more efficient walking operation.

2 CASSINO HEXAPOD WALKING MACHINE

The Cassino Hexapod Walking Machine can fit a cuboid of 60 cm x 60 cm x 50 cm without any payload or PLC installation. The picture of this robot is shown in Figure 1. For the body, a simple aluminum frame was adopted. Each leg of the robot has three motors, two for the joints and one for the wheel. This allows each leg to execute rotations in the Z plane.

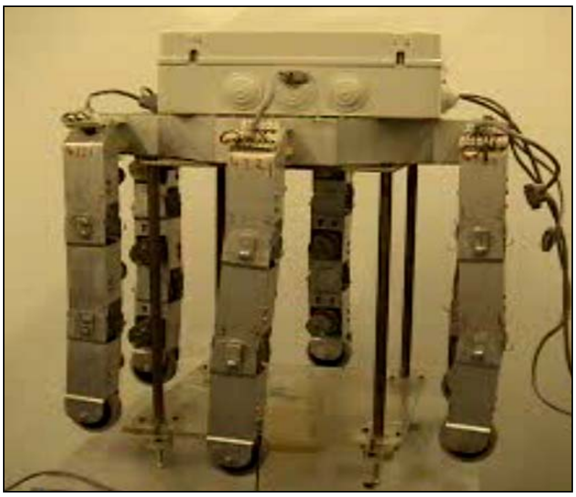

Figure 1 The Cassino Hexapod Walking Machine with powered wheels at the feet [4,5].

Referring to Fig. 2, the kinematic design of each leg is composed of 3 modules, whose links l_1, l_2 and l_3 connect each other by 3 rotational joints R_1, R_2, R_3. The wheel is modeled through joint R_4. In particular, an anthropomorphic design can be recognized in the superior part of the leg with joints R_1 and R_2, since they may reproduce a femur frame. In this particular case R_2 raises and lowers the leg and R_1 operates the movement of the wheel forward or backwards. The third joint, R_3 in the lower part of the leg reproduces the knee motion.

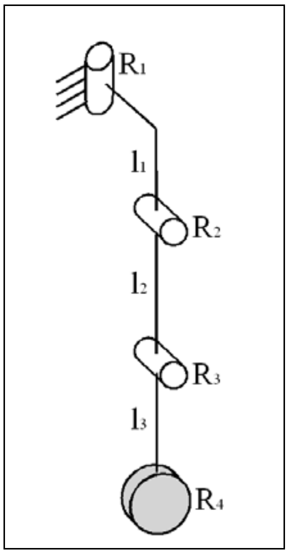

a)

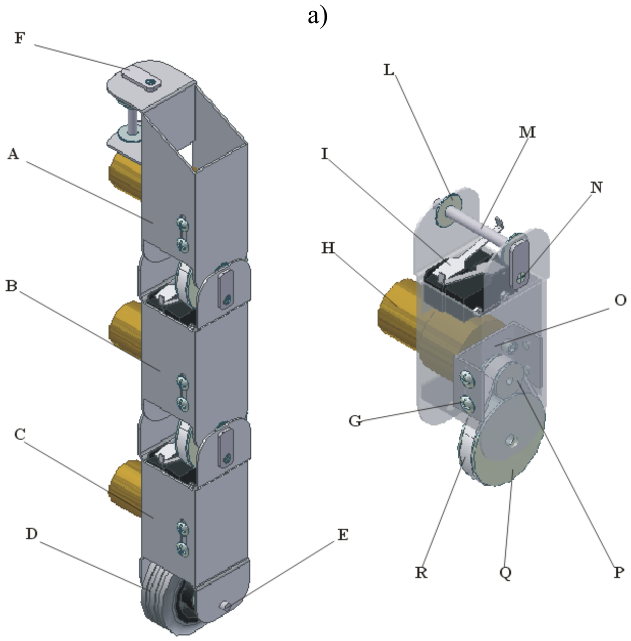

b)

Figure 2 The leg design for Cassino Hexapode Walking Machine, [6]: a) a Kinematic scheme b) a mechanical design in which letters indicate single parts.

Table I - Components of the leg design in Figure 2b).

A	Support module
B	Standard module
C	Module for the wheel
D	Wheel
E	Hinge for the Wheel
F	Hinge for the support
G	Screw for motor
H	D.C Motor
I	Limit Switch
L	Washer
M	Hinge between the modules
N	Screw of blocking hinge
O	Support for the motor
P	Pulley for the motor
Q	Movable pulley
R	Timing belt

Each leg consists of three modules with total height of 500 mm. Each module contains a motor for driving the corresponding link. The actuation system includes belt and pulley for speed reduction and transfer of motion from the motor to the link. In addition, a touch sensor is installed on the motor for detecting the extreme ends of the leg motion. This mechanical design is shown in Fig. 2b and the single parts are listed table 1 [6].

The kinematic mobility of the robot allows a good number of operations to be carried out. These operations include walking, rotation, translation, translation by the wheels, climbing and descending stairs.

Each joint can move up to an angle of +/- 90°. Timing belts for the motion transmission give smooth motion of the links. Nevertheless, problems in the current Cassino Hexapod Walking Machine can be identified as due to its design, such as low speed, high design complexity, low autonomy, large overall weight, and complicated movement control.

Stable, efficient and fast robots are needed to navigate in uneven environments which can help humans in unconventional applications like inspection and restoration of archeological sites and interplanetary exploration. In fact, a very important and immediate use of the Cassino Hexapod Walking Machine robot has been identified for the inspection of inaccessible areas in the pavement of Basilica of Montecassino Abbey. In addition, referring to the Cassino Hexapod Walking Machine and its capabilities, further possible applications can be identified in deep sea or planet surveying; exploration on the Moon or on Mars; underground mining robot; automated agriculture or foresting robot; automated or tele-remote controlled construction robot; firefighting robots that can climb over rough terrain and large obstacles.

The operation of the Cassino Hexapod Walking Machine is achieved by using a PLC which controls the leg motors. A Siemens PLC S7-200 is fixed onboard on the robot body platform. In order to accommodate all the inputs and outputs, an extension module has been provided for the PLC. The program for the operation has been written in STEP-7/Micro WIN 32. The program from a PC can be downloaded onto the flash memory of the PLC by using a RS 232/PPI Cable. A schematic layout of the overall system is shown in Figure 3 [5].

In addition, a control pad with latching switches can be also used to operate the Cassino Hexapod Walking Machine with the designed solution in Figure 4. An external DC Power Supply is used to provide power to the robot.

On the Cassino Hexapod Walking Machine, there are six legs and each leg has 3 motors. Thus, a total of 18 motors are installed for walking operation of the robot. A input to each motor is needed for switching On/Off the motor and one input can be used for changing the direction of rotation of a motor. An external relay circuit has been used for changing the direction of rotation of a motor. This enables the use of only one PLC with one extension module for operating the robot.

For programming purposes, the motors have been identified as x.y, where x refers to the leg number and y refers to the motor number in the leg. The motors in any of legs are numbered from top to bottom. It must be noted that the motors of the right half and the left half of the robot are connected in the opposite polarity. This ensures that the control of both sides of the robot is identical. Thus, for the forward motion of the robot, if the motor in the right side rotates in the clockwise direction, the motor in the left side must rotate in the anticlockwise direction.

In preliminary tests, the wheel motors of legs 1,2,3 have been connected together and similarly the wheel motors legs of 4,5,6 r. This can be used for making easy forward and backward motions. Also, the turning of the robot can be achieved by moving the motors of one side keeping the motors on the other side stopped.

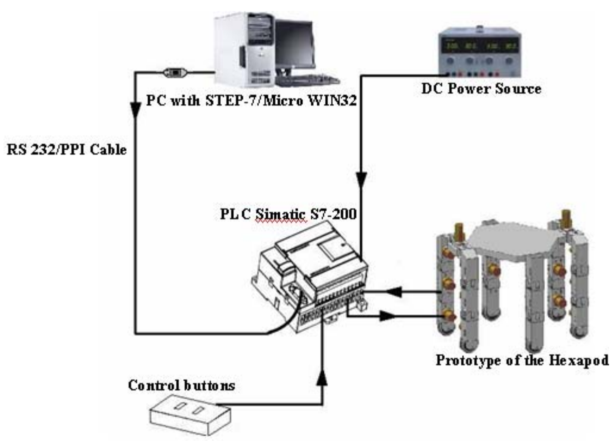

Figure 3 A schematic diagram of the hardware layout for Cassino Hexapod Walking Machine operation [5].

Figure 4 The control pad for controlling Cassino Hexapod Walking Machine.

3 DEVELOPMENTS FOR AN ENHANCED DESIGN

The following modifications have been proposed and analyzed:

- Increase of turning and rotating capacity;
- Reduction of stress in the joints;
- Improvement in the run-out of the system;
- Review the CAD design of the robot by looking at each component and then the whole assembly by using the real parameters of the built prototype;
- Component design for cheap solutions;
- Reduction of the time for the movements;

The proposal for changes starts with the mechanical transmissions in the robot. For turning the legs suitable actuations and mechanical transmissions system are needed as composed of electric motor, driving belts and wheels for each actuated joint. By considering the modularity and the cost-oriented feature of the prototype the same electric motor has been adopted for the actuation of each joint in all the legs. The transmission system is composed of the gear wheel and the driving belt as shown in the design of the actuator Fig.5.

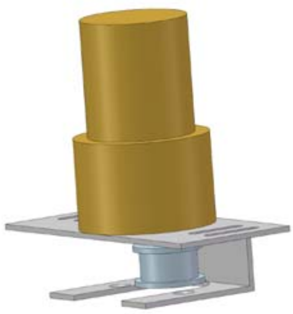

Figure 5 Proposed actuation system and its support.

All these new features combined in an inventive and efficient way, can provide a better turning capacity of the robot, and in the same time reduce the wear and tear on the whole assembly. Another very important aspect to which this change contributes is the reduction of stress in the leg joints so that the system can be used for a larger period of time, more efficiently and in harsher real time conditions.
The new system with the proposed design and functional changes is shown in Fig. 6.
In this new proposed version the two central legs have only two degrees of freedom, because there is no more use of the inner and outer rotational movements of these legs, once it is understood that these are redundant degrees of freedom for the actions that the robot executes.
Another solution for the central legs could be the rigid connection to the body of the support module, so that the robot will still move in the same way. This will simplify the system and will make it cheaper. But for general aspects on symmetrical design for dynamical stability of the whole system, the same kind of support was implemented. Another solution that will decrease the total cost of the robot is the elimination of electric motors that actuate the wheels of the central legs. Even with this change, the robot will be still able to execute a proper rotation and translation but the speed by which the movements will be executed will be surely influenced. Because of this reason it is convenient to keep the electric motors, as in the original design.

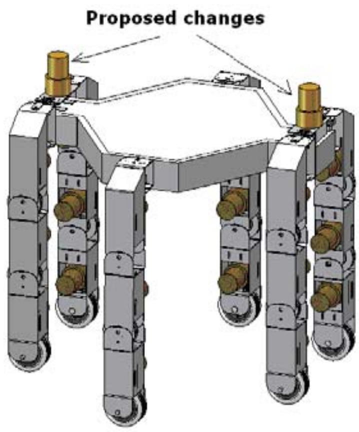

a)

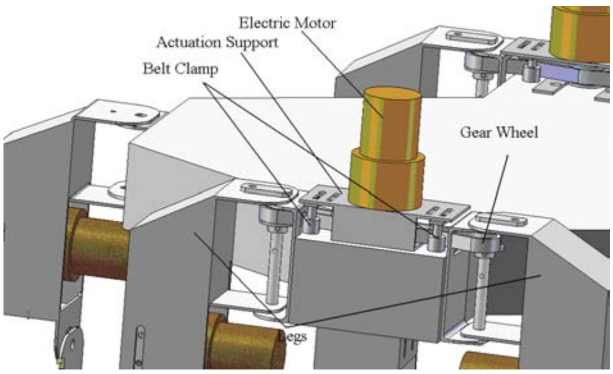

b)

Figure 6 A new mechanical design of Cassino Hexapod Walking Machine with the proposed changes in leg actuation: a) a general layout; b) the mechanical design of actuator installation.

Thus, the anterior and posterior legs are connected to the robot body platform trough the same joints that are actuated by the same electric motors as for the all other legs. This makes possible to use the same mechanical transmission system as in the other actuated leg joints, in the design that it is shown in the details in Fig. 6 b.

Another important factor is the control of the implemented mechanical transmission system of the two motors for the rotational movement. A maximum degree of rotation can be determined in order to avoid collision among legs and the body platform. Since it could be not convenient to install a sensor that could delimit the movement to a certain point, a suitable alternative solution could be the time control for the motors actions. For example it is easily possible to prescribe a maximum time for the motor rotation.

By using the above-mentioned changes Cassino Hexapod Walking Machine can perform more successfully sets of actions, namely to translate, to rotate in a smother and faster way, to walk in an uneven terrain, and to go up or down along stairs.

For a movement in uneven terrain a tripod-gate movement can be conveniently adopted, and the basic rule is to always keep three legs in contact with the ground. In generating a tripod-gate movement, a cycle can be programmed by planning two types of fundamental steps that can be repeated in succession. The two types of steps can be identified in the following: the front and the rear legs of one side and the middle leg of the other side perform their swing movements at the same time while the other three legs remain in contact with the ground; and the second phase is the same repeated but by alternating the set of the three legs in the above swinging and support phases.

Referring to the schemes in Fig. 7, a motion sequence can be programmed for the tripod-gate walking through the fallowing eight phases.

Phase 1: in the initial phase, figure 7 a), the robot has all the legs in vertical position; then the robot moves simultaneously three legs per phase, two of them from one side and another leg in the other side, in order to generate a forward walk. Phase 2: the step is performed by moving three legs forward ahead, figure 7 b), and afterwards in phase 3 they will be moved down to contact the ground, figure 7 c). Phase 4: while three legs are in contact with the ground, and raise the other three legs to make the robot to walk forward or half step, , figure 7 d).

In this way, by repeating the phases from 1-4 for the other three legs, a complete step is carried out. The overall length of the step can be planned for a length of 310 mm.

The robot can go forward or backwards by using the same sequence just by inverting the rotation direction of the motor. In addition, by operating the two motors on the robot body platform, turning can be achieved, while walking with the above mentioned tripod-gate sequence yet. In this way the effective time that is needed for effectuating a full rotation of the robot can be decreased. In addition there is the mechanical stress at the joints is limited because the movement is much smoother and continuous.

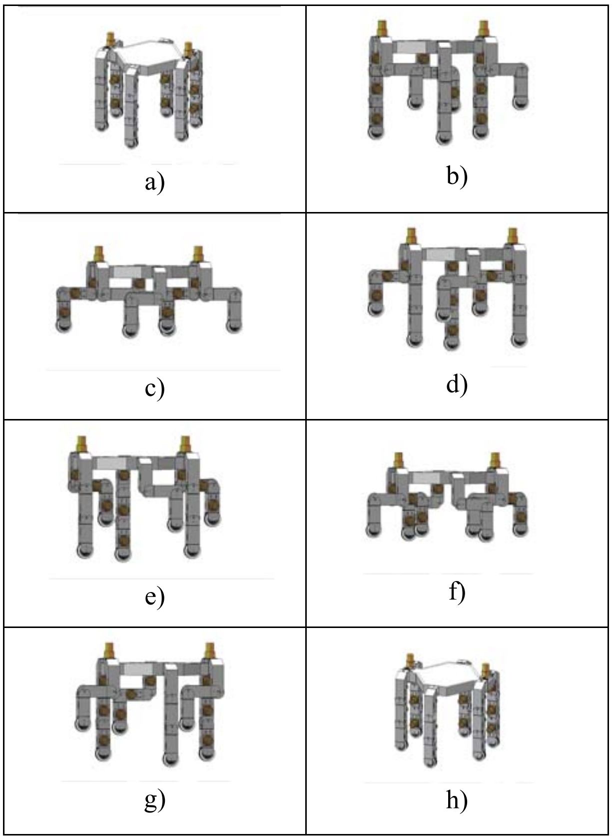

Figure 7 A motion sequence for the tripod gate: a) phase 1; b) phase 2; c) phase 3; d) phase 4; e) phase 5; f) phase 6; g) phase 7; h) phase 8.

4 SIMULATION RESULTS

The proposed changes have been analyzed through simulation with suitable modeling in ADAMS environment with the CosmosMotion package,[10]. In Fig. 8, the model is shown in the CosmosMotion environment.

In order to compute a proper simulation and a correct analysis of the assembly, the parameters which are implemented in CosmosMotion have been accurate as related to the built prototype. In the following example the robot performs a complex type of movement, namely a rotational movement for the first and second joint, and then a translational movement of the whole robot by using the wheel in joint 3. Fig. 9 presents one of the legs of the robot, and it’s joints as they are taken in consideration. The displacements in the first two joints are equal but in opposite directions, and the displacement in the third joint is larger and its direction depends on the direction to which the robot is moving.

ISSN 1590-8844
International Journal of Mechanics and Control, Vol. 10, No. 02, 2009

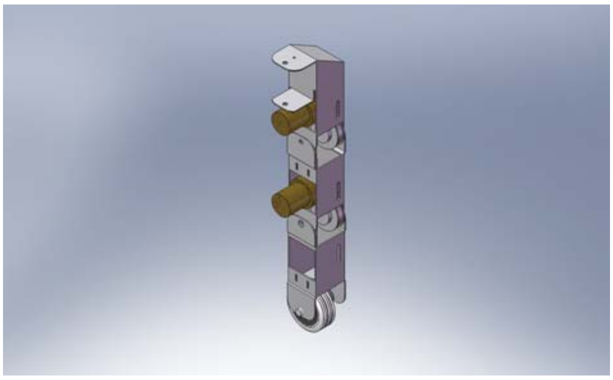

a)

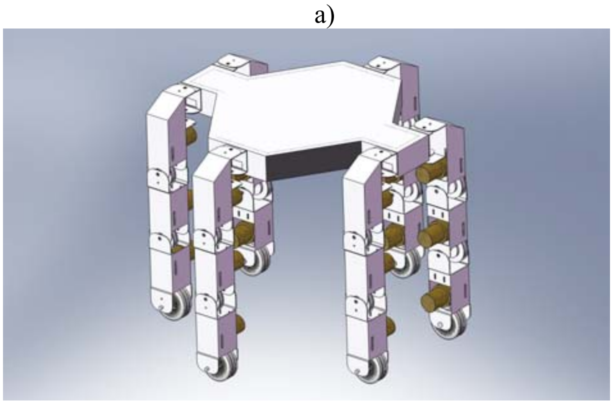

b)

Figure 8 CosmosMotion model: a) one leg; b) the Cassino Hexapod Walking Machine.

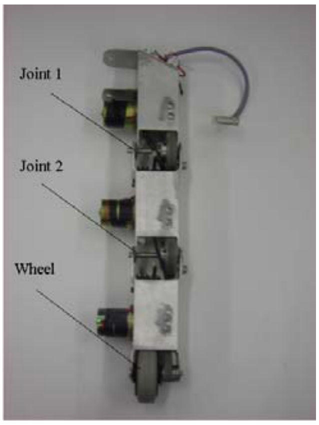

Figure 9 Representation of the joints in the built prototype.

In Fig. 10 the results of the simulation in Adams are presented for the three joints of one leg.

In Fig. 11 it can be seen that by implementing a certain angular velocity in each of the first two joints, the obtained torque is of similar amplitude but reversed sense. Also the outcome of this simulation shows that the torque in each case depends of the velocity: it increases if the velocity is increased and once the velocity has reached its highest pick the torque also reaches its maximum value and then remains constant up to the end of the movement.

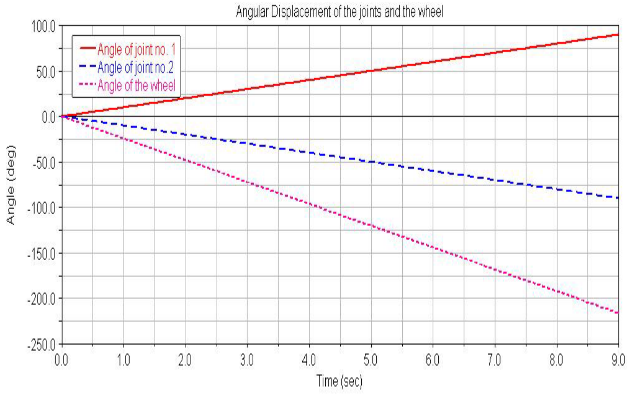

Figure 10 Angular displacement of the wheel and the other two joints.

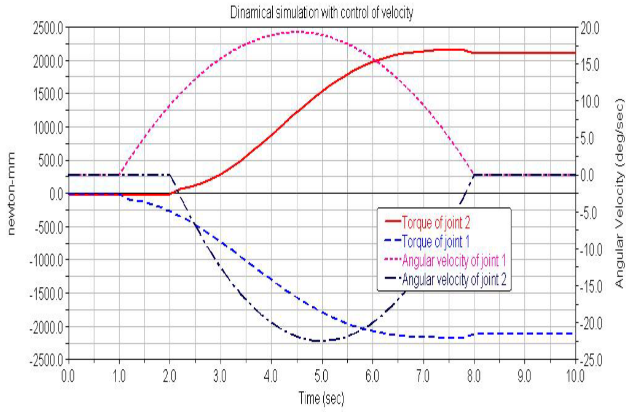

Figure 11 Results of dynamical simulation of the model with velocity control.

In Fig.12 the mechanical power consumption is reported as related to one leg. It can be seen that the energy consumption increases as the distance from the ground becomes shorter: the smallest consumption is on the first joint, and the larges is in the wheel. This is because the first joint has to move only the upper part of the robot, while the second one supports also the first joint and its components.

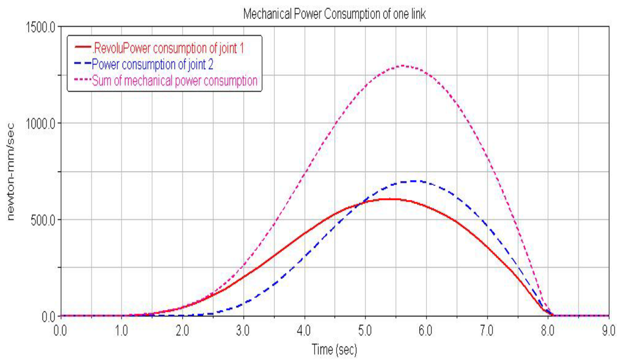

Figure 12 Results for mechanical power consumption in the leg motion.

5 LABORATORY TESTS

The feasibility of the tripod-gate walking has been tested in a test that is shown in Fig.13. In Fig. 13 a) all legs are in vertical configuration. Later on in Fig. 13 b) legs 1-3-5 move towards right until the position limit. In Fig.13 c) legs 2-4-6 move towards left in order to achieve position limit. In Fig.13 d) legs 1-3-5 is brought back in configuration begin them. At last legs 2-4-6 are brought back in the initial configuration. From the images it can be seen that the positions limit for the legs are not exactly the same ones.

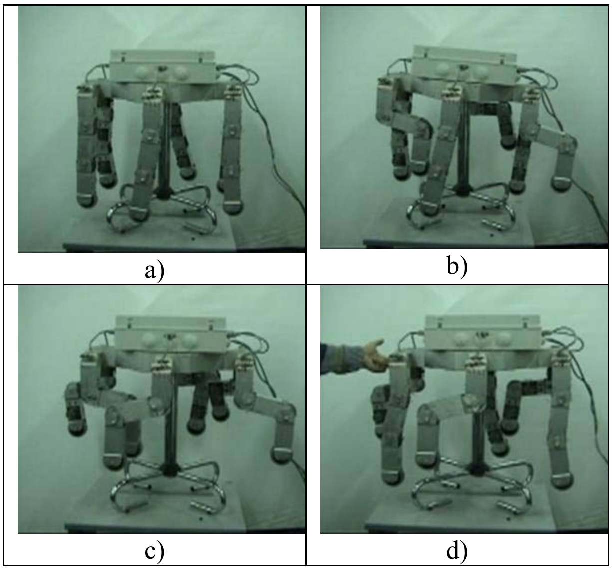

Figure 13 A laboratory test for the tripod-gate walking of Cassino Hexapod Walking Machine: a) starting configuration (phase 1 in Fig. 9); b) three legs up(phase 2 in Fig. 9); c) all legs up(phase 3 in Fig. 9); d) legs up and legs down (phase 7 in Fig. 9).

This is due to the switch limits, since in each joint the output of the sensors is activated in different positions.
In addition, tests have been carried out with sensors to monitor and measure the movement characteristics. In particular, the acceleration of reference points of the legs and torque of the motors have been measured during walking movements. A first test concerned the bending motion of one single leg in two phases of a movement. In the initial phase (figure 13 a) the leg is in vertical position and in the final phase (figure 13 b) the leg is in the final position. The measures of the acceleration have been obtained by using a Kistler accelerometer model k-beam 8303A 10 that has been installed on one leg in several places [10]. In Fig. 14 the modalities of installation of the accelerometer are shown.
In Fig. 15 the values of the measures are shown as referred to the tests with acceleration installations in Fig. 14. It can be observed that the value of the acceleration in the third plot is different from the second plot; therefore it means that there might be a problem in the actuation system of that joint.

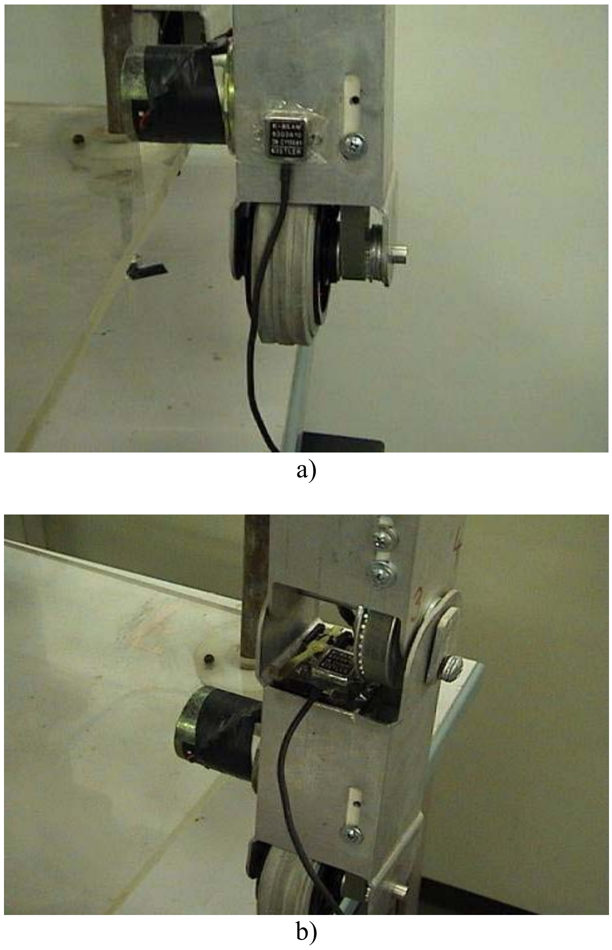

Figure 14 Kistler accelerometer k-beam 8303A on a leg of the Cassino Hexapod Walking Machine: a) accelerometer on the left side of a leg; b) accelerometer installed horizontally in a leg.

In order to improve the operation of the robot it has been thought useful to provide manual regulation of the speed of the actuators. The regulation of the speed that is previewed for the robot is based on the variation of the tension of alimentation of the motors. With reference to a single motor, a potentiometer has been installed in series to the rotor windings [10].

6 CONCLUSIONS

This paper presents The Cassino Hexapod Walking Machine Robot with proposals for enhancing its design and operation. The main contribution of this paper is in the new proposed design, in which the mechanical structure has also been modified. This modification allows the robot to improve the turning and movement capability. In order to define the above modification, modeling and simulation have been worked out. In particular the paper has reported:

- simulation results for straight-line walking, rotating, obstacle avoidance and combined movement with the new robot design;

- laboratory tests for operation of one leg, and the whole Cassino Hexapod Walking Machine, with measurements of the accelerations (after suitable calibration), the torque, and potentiometer outputs;
- new design solutions for the robot with the aim to improve the turning and movement capability.

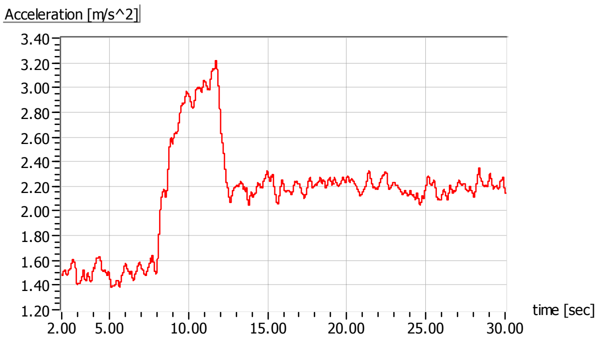

a)

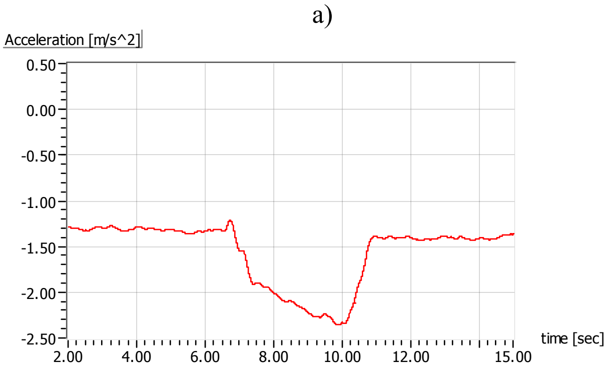

b)

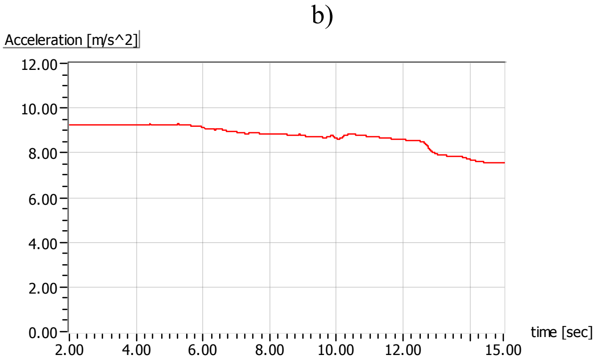

c)

Figure 15 Measured accelerations : a) component along the Z axis; b) component along the Y axis with the; c) component along the Y axis with the sensor installed on the left side.

ACKNOWLEDGEMENTS

The work which is reported in this paper has been partially developed during a stay of the second author at LARM in Cassino within ERASMUS program in 2008.

REFERENCES

[1] Carbone G., Ceccarelli M., "Legged Robotic Systems", Cutting Edge Robotics ARS Scientific Book, Wien, pp. 553-576, 2005.
[2] Deere & Company©: The walking forest machine, website http://www.techeblog.com/index.php/tech-gadget/a-look-back-walking-forest-machine, 2008.
[3] Pfeiffer F. Weidemann, H.-J.; Eltze, J. " TUM Walking Machine", Technische Universität München, Munchen 1994.
[4] Craig, J. (1986). *Introduction to robotics*. Addison – Wesley, New York.
[5] Carbone G, Ceccarelli M., "A Mechanical Design of a Low-Cost Easy-Operation Anthropomorphic Wheeled Leg for Walking Machines", The International Journal Robotics & Management, vol.9, n.2, pp.3-8, 2004.
[6] Carbone G., Shrot A., Ceccarelli M., "Operation Strategy for a Low-Cost Easy-Operation Cassino Hexapod", Applied Bionics and Biomechanics, 2007, Vol.4, N.4.
[7] Carbone G.,Ceccarelli M., " A low-cost Easy-Operation Hexapod Walking Machine ", International Journal of Advanced Robotic Systems, Vol. 5, no.2, 2008, pp. 161-166.
[8] MSC.Adams , http://www.mscsoftware.com/ ,2008.
[9] SolidWorks and CosmosMotion, http://www.solidworks. com/, 2008.
[10] Suciu M., Master Thesis "Design enhancements and test laboratory of Cassino Hexapod Walking Machine", CESTER Laboratory, University of Cluj-Napoca, Cluj-Napoca, 2008.

ISSN 1590-8844
International Journal of Mechanics and Control, Vol. 10, No. 02, 2009

DYNAMIC AND ENERGY ANALYSIS OF A PRODUCTION SYSTEM OF FILAMENT WOUND ELBOWS

Pasquale Buonadonna, Gennaro Dionoro, Aurelio Tronci

Department of Mechanical Engineering, University of Cagliari
Piazza d'Armi – 09123, Cagliari, Italy

ABSTRACT

An automatic production system for reinforced-fibre products with no-axial symmetric geometry was very difficult to obtain by filament winding technology, until the recent development of new calculation codes. Especially difficult was to design a deposition trajectory that respected the complete mandrel covering and uniform fibre distribution conditions in the final composite. This work shows the dynamical analysis and the energetic balance of a completely automated production system for no-axial symmetric product by filament winding technology. This system was applied to 90° curved pipefitting.

Keywords: filament winding, dynamic analysis, energy balance.

1 INTRODUCTION

Filament winding technology is an automated production process of fibre-reinforced composite materials. It consists in winding resin-impregnated fibres sheaf round a mandrel that determines composite geometry. A deposition eye guides the fibres from the bobbin to the mandrel. Often many sheaves, at the same time drawn from different bobbins, are winded. These sheaves pass through combs, that take them separated, and through systems that remove the excess of resin. After the complete resin polymerisation, the composite is removed from mandrel. The greatest benefit of this technology is to obtain products with a very good mechanical property-weight ratio, for this reason filament winding is one of the more effective techniques in composite materials production [1, 2]. But a great limitation was its application, in industry, almost exclusively to generally axial-symmetric very simple shapes products, such as pipefitting, under-pressure tanks and for chemical substance. To realise more complicated shapes was used manual or semi-manual winding, which causes inaccuracy and lack of repetition, refuses, low production level and workers interaction with potentially wealth dangerous materials. In the nineties, the introduction of computerised 6-axis independent winding machines allowed process automation. An efficient employment of these machines needs to use software tools that permit a complete automatic products design, including part-program for commercially available control systems. So, many software tools for calculating the deposition trajectory of fibres sheaf in filament winding were developed. But the major part of them is unable to create complex geometry, creating only axial-symmetric forms [3]. The most important technical problem to complete production process automation was the lack of software tools able to calculate deposition trajectory for complex geometry. Recently, however, calculation codes have been developed (CADWIND, CADFIL) suitable for the design of complex deposition trajectories.

In this work the dynamic and energetic analysis of a completely automated winding system of elbows, through 4 axis computerised winding machines (fig. 1) is presented. At first, it will be dealt with deposition trajectory calculation, and then a dynamic and energetic analysis of winding process will be carried out.

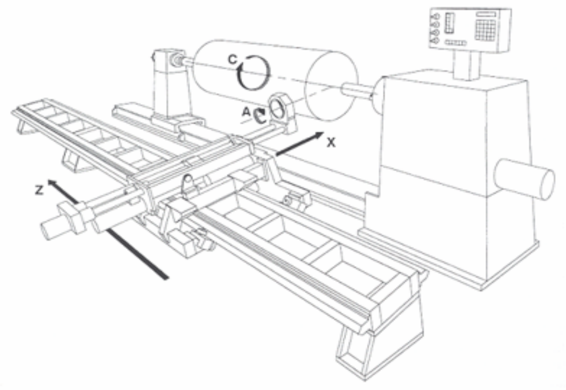

Figure 1 Computerised 4 axis machine.

Contact author: Gennaro Dionoro[1]

[1] University of Cagliari
Department of Mechanical Engineering
Piazza d'Armi – 09123, Cagliari, Italy
E-mail: dionoro@unica.it

2 FIBRE PATH CALCULATION

Deposition trajectory calculation is founded on two principles: uniform mandrel covering and best composite resistance. To obtain both the conditions, all filament winding technical qualifications must be respected, such as lack of fibre slipping and bridging and complete mandrel covering, so that fibres were laid accurately [4]. It is clear that the deposition trajectory calculation is very important in a filament winding production system design.
There are two methods to calculate deposition trajectory: the first one is the analytical solution of differential equations of trajectory, while the second one subdivides the dominion of such equations, i.e. the surface to be covered, in more simple parts, as, for example, triangles [5]. The first method is usually employed for axial-symmetric geometry workpieces, because an analytical solution to differential equations can be obtained. For no axial symmetric mandrels, numerical methods are preferred, because the differential equations' system doesn't have an easy solution. The numerical method is suitable for general surfaces, but it provides an approximate solution and the mistake that is committed respect the analytical one is difficult to evaluate. In fact, even if it is possible to divide the surface to be covered in as many parts as we wont, the solution is however approximate.
Among the actually available software tools, only CADFIL [6] and CADWIND [7] are able to calculate deposition trajectories for asymmetric surfaces, and both of them use a numerical method.
Deposition trajectory calculation is obviously strictly dependent from product geometry, so, first of all, to study the problem is necessary to choose the more suitable calculation algorithm.
In this work the application of the numerical method in the production of 90° elbows is shown. It is even shown that, if we want to develop a completely automated winding system, it is necessary to modify manual winding mandrel's geometry in order to optimise the deposition process. The experimental part has been carried out into a filament winding specialized factory.
Two mandrel kinds are considered in this work. The first one (A type) is formed by a circular torus (fig. 2) and is the one that is employed in the manual winding. In this case the operator has to stop the mandrel's rotation before changing the fibre's deposition direction and, for big-size handworks, we must spend a great amount of energy in order to win inertia's forces. This amount can be very large and because of it, in some cases, the production of these elements is technically impossible. The second type (B type) is formed by a central circular torus and two cylindrical extension parts (fig. 3) and is the one that is employed in the automated winding. While the inertia's forces problems are solved by the use of this geometry, when the deposition eye has to invert the direction of the pay out speed is an inescapable fact to have a fibre's build up at the ends of the mandrel. In order to avoid the handwork's refuse, the mandrel's geometry has been modified by the addiction of two cylindrical extensions where the fibres are built up. The extensions will be removed at the end of the resin polymerisation's process. This solution has been adopted in a real process and this paper is going to demonstrate its energetic advantages.
An alternative splines-based method to calculate deposition trajectory has been developed by Li H. et al. [8, 9] but, for such a geometry, the ideal algorithm is still the not geodesic one [7], used by CADWIND.

CADWIND production process starts setting the winding machine parameters:

- Start point;
- winding machine working-space geometric dimensions;
- winding machine maximum velocities and accelerations;
- axis;

and then proceeds with mandrel design, by setting specifically geometric parameters (fig.4):

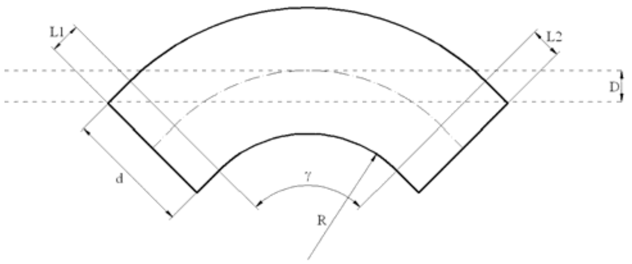

Figure 4 Mandrel's geometric parameters.

- d section diameter [m];
- R internal radius [m];
- γ opening angle [rad];
- D transposition central axis-rotation axis [m];
- L1,L2 mandrel extensions [m].

During winding process, typical material parameters for this kind of working have been used:

- roving number = 10;
- fibre mass content = 50%;
- fibre's density = $2.54\ 10^3$ kg/m^3;
- roving thickness = $4\cdot10^{-3}$ m;
- fibre's linear density = $2.40\cdot10^{-3}$ kg/m;
- resin's density = $1.20\cdot10^3$ kg/m^3.

Non geodesic algorithm is a numerical method for calculating trajectories that divides the mandrel in triangular surfaces (fig. 5).
Parameters setting, necessary for not geodesic algorithm, follow:

- winding angle;
- pattern number;
- friction factor (tab. 1);
- degree of covering: [%];
- turning zone;
- starting frame;
- dwell [rad];
- starting position.

ISSN 1590-8844
International Journal of Mechanics and Control, Vol. 10, No. 02, 2009

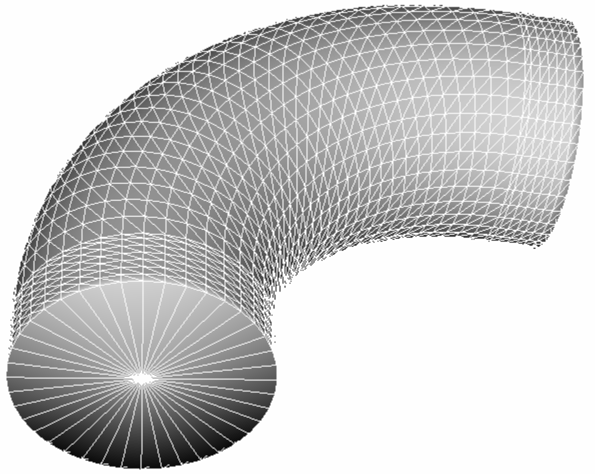

Figure 5 Mandrel’s surface subdivision.

Table I - Friction factor.

Surface	Dry Fibre	Preg. Fibre	Pre-Preg.
Metal	0.18	0.15	0.35
Plastic	0.20	0.17	0.32
Dry Laminate	0.22	-	-
Preg. Laminate	-	0.14	-
Pre-Preg. Laminate	-	-	

The trajectory is composed of a series of points into the depositor’s workspace that, starting from the origin point, are touched in succession. A matrix (fig. 6), where lines succession represented the same trajectory points and columns are depositor’s degrees of freedom, represents this trajectory. In this case, the eight matrix columns represent: the first one a sequence’s advancing index, the second mandrel’s rotation, the third Z axis, the fourth X axis, the fifth deposition eye rotation angle, the sixth and the seventh are degrees of freedom not used in the process, while the eighth is the time.

1	241.447433	61.039352	305.600006	0.000000	0.000000	0.000000	0.000000
2	258.894135	57.994034	305.600006	0.000000	0.000000	0.000000	0.080811
3	267.371277	58.480396	305.600006	0.000000	0.000000	0.000000	0.161621
4	275.115479	73.404274	305.600006	0.000000	0.000000	0.000000	0.428032
5	283.276581	84.842522	305.600006	0.000000	0.000000	0.000000	0.535919
6	291.332550	95.660599	305.600006	0.000000	0.000000	0.000000	0.616730
7	299.349182	107.097168	305.600006	0.000000	0.000000	0.000000	0.697540
8	307.104797	123.995262	305.600006	0.000000	0.000000	0.000000	0.785767
9	315.194153	141.738770	305.600006	0.000000	0.000000	0.000000	0.866577
10	323.390442	160.249557	305.600006	0.000000	0.000000	0.000000	0.947388
11	331.735901	175.704788	305.600006	0.000000	0.000000	0.000000	1.028198
12	340.224304	190.919876	305.600006	0.000000	0.000000	0.000000	1.109009
13	349.580017	210.897461	305.600006	0.000000	0.000000	0.000000	1.198059
14	358.823395	230.329544	305.600006	0.000000	0.000000	0.000000	1.309525
15	368.264343	248.837158	305.600006	0.000000	0.000000	0.000000	1.458374
16	377.741821	261.727570	305.600037	0.000000	0.000000	0.000000	1.631783
17	378.858398	263.694061	305.600006	0.000000	0.000000	0.000000	1.712593
18	388.873047	279.617950	305.600006	0.000000	0.000000	0.000000	1.926811
19	398.630371	288.174438	305.600006	0.000000	0.000000	0.000000	2.007622
20	408.176575	293.028351	305.600006	0.000000	0.000000	0.000000	2.088432
21	417.577484	295.776031	305.600006	0.000000	0.000000	0.000000	2.169243
22	418.870087	294.777039	305.600006	0.000000	0.000000	0.000000	2.250053

Figure 6 Trajectory matrix.

Matrix single column can be plotted into CadWind, to verify eventual discontinuity points’ presence (calculation defects, fig. 7-8). When discontinuity points are smoothed, part program trajectory matrix of calculation can be generated in ISO Standard language for winding robot.

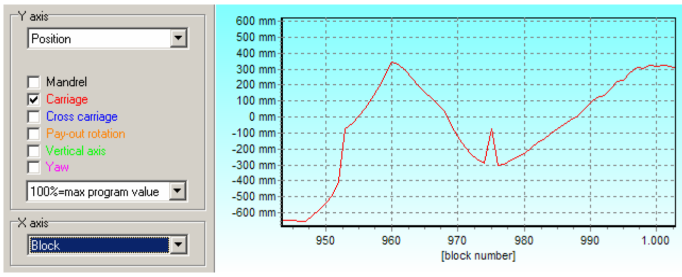

Figure 7 X axis deposition trajectory representation with evident discontinuity point.

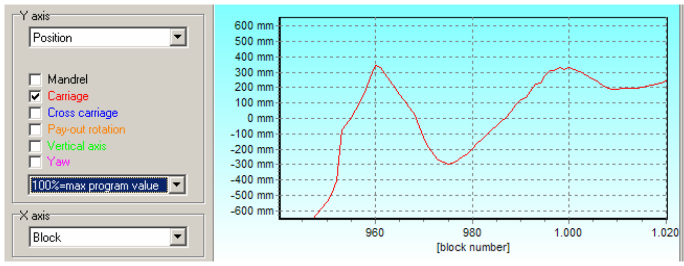

Figure 8 X axis deposition trajectory representation after the correction.

3 DYNAMICAL ANALYSIS

3.1 INERTIA MOMENT CALCULATION OF A-TYPE MANDREL.

The mandrel is a homogeneous part (ρ = cost) formed by a circular torus part, defined in an x-y-z coordinates system (fig. 9) by parametric equations:

$$\begin{cases} x = (R + r\cos\varphi)\cos\vartheta & r \in [0.18, 0.20]R = 0.60[m] \\ y = (R + r\cos\varphi)\sin\vartheta & \vartheta \in \left[-\frac{\pi}{4}, \frac{\pi}{4}\right][rad] \\ z = r\sin\varphi & \varphi \in [0, 2\pi][rad] \end{cases} \tag{1}$$

where volume V is produced by the integral:

$$V = \int_V dV = \iiint dxdydz = \iiint \det|J|\, dr\, d\vartheta\, d\varphi \tag{2}$$

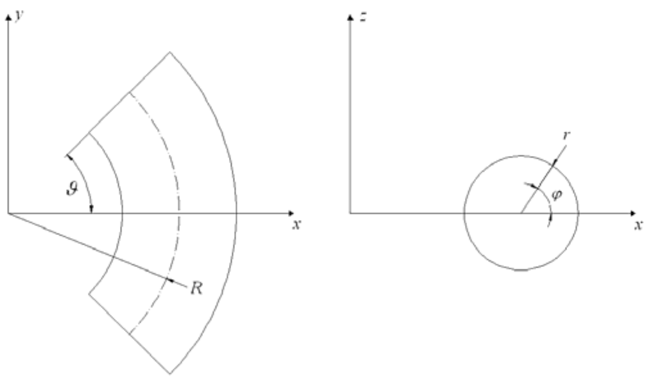

Figure 9 Torus parameters.

In this case the Jacobian determinant is:

$$\det|J| = r(R + r\cos\varphi) \tag{3}$$

So, substituting the (3) in the (2):

$$V = \iiint r(R + r\cos\varphi)\, drd\vartheta d\varphi = 0.0225m^3 \tag{4}$$

Consequently, m mandrel's mass, considering that it is a steel one (ρ = 7830 kg/m^3), is:

$$m = \rho V = 176kg \tag{5}$$

For homogeneous solids, y-axis inertia's moment is defined as:

$$\begin{aligned} I_{yy} &= \rho \int_V (z^2 + x^2) dV = \\ &= \rho \iiint r[r^2 \sin^2 \varphi + (R + r\cos\varphi)^2 \cos^2 \vartheta] \\ &\quad (R + r\cos\varphi) drd\vartheta d\varphi \end{aligned} \tag{6}$$

Therefore we have:

$$I_{yy} = 69.2kgm^2 \tag{7}$$

While, if we want to calculate inertia's moment respect an axis passing through centre of gravity G, we must know its co-ordinates:

$$x_G = \frac{\int_V xdV}{V} \qquad y_G = \frac{\int_V ydV}{V} \qquad z_G = \frac{\int_V zdV}{V} \tag{8}$$

y_G and z_G co-ordinates are of no value, because the mass is symmetrically distributed respect y and z axis. So just x_G calculation is needed:

$$x_G^A = \frac{\int_V xdV}{V} = \frac{\iiint (R + r\cos\varphi)^2 \cos\vartheta drd\vartheta d\varphi}{V} = 0.567m \tag{9}$$

Now, using Steiner's formula, it is possible to obtain inertia's moment I_G passing through a barycentric axis parallel to y-axis:

$$I_G^A = I_{yy} - mx_G^2 = 6.21kgm^2 \tag{10}$$

From this calculation it is possible to extract mandrel's geometric parameters to put in CadWind to calculate fibre deposition trajectory's matrix:

- d = 0.4 m;
- R = 0.6 m;
- γ = π/2 rad;
- D = 0.033 m;
- L1 = L2 0.001 m.

Non-geodesic algorithm parameters used in this case are:

- winding angle = 1.29 rad;
- pattern number = 1/1;
- friction factor = 0.175;
- degree of covering = 140%;
- turning zone back = 34;
- turning zone front = 9;
- starting frame = 21;
- dwell = 2.44 rad;
- starting position = 0 rad.

3.2 DYNAMICAL ANALYSIS

During fibres deposition process, the mandrel turns around a barycentric axis drawing an α angle, that is obtained from trajectory's matrix produced by CADWIND. The instantaneous mandrel's angular speed is easy to get if this angle's trend in function of t time is known. Since this is expressed as α and t vectors, numerical derivatives are necessary to obtain angular speed (fig. 10), but they don't give the exact solution. Precisely, finite difference method was used caused by t regular intervals' lack:

$$\dot{\alpha} = \frac{\Delta\alpha}{\Delta t} = \frac{\alpha_i - \alpha_{i-1}}{t_i - t_{i-1}} \tag{11}$$

In the same way angular acceleration (fig. 11) was calculated:

$$\ddot{\alpha} = \frac{\Delta\dot{\alpha}}{\Delta t} = \frac{\dot{\alpha}_i - \dot{\alpha}_{i-1}}{t_i - t_{i-1}} \tag{12}$$

The torque given to mandrel's axis is obtained from angular acceleration:

$$C = I_G^A \ddot{\alpha} \tag{13}$$

The elementary work made from external forces is:

$$dL_e = Cd\alpha \tag{14}$$

So, the total work provided from external forces during process is given from the integral:

$$L_e = \int_\alpha Cd\alpha \tag{15}$$

Having α and C values vectors at disposition, this integral was solved numerically using trapezium's method:

$$L_e = 10kJ \tag{16}$$

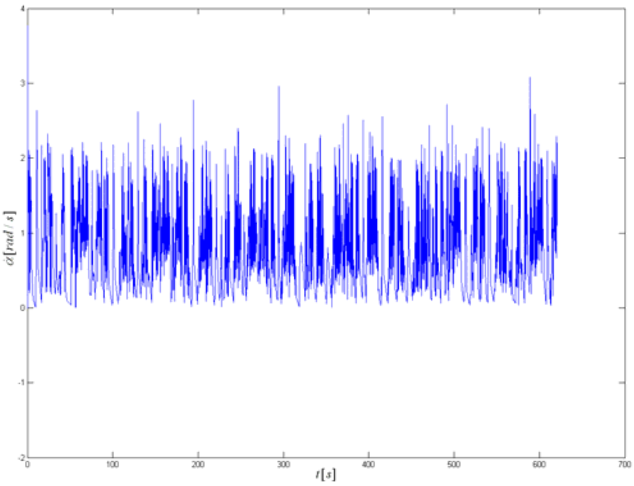

Figure 10 Mandrel angular speed.

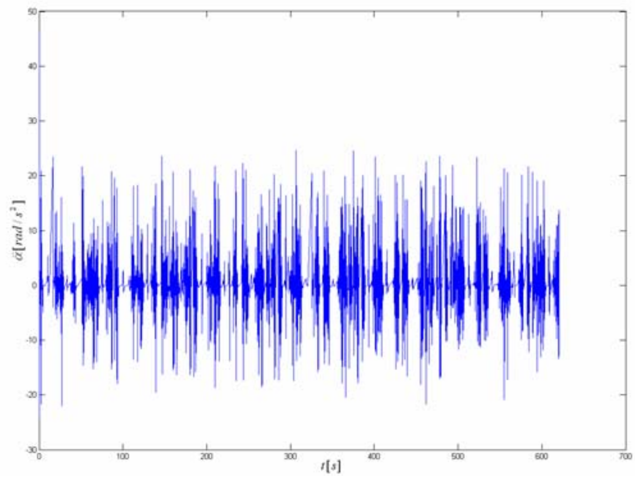

Figure 11 Mandrel angular acceleration.

3.3 ENERGY BALANCE

For a mechanical system we have:

$$dL_e + dL_i = dE_c + dE_g + dE_e \quad (17)$$

Or, in finite terms:

$$L_e + L_i = \Delta E_c + \Delta E_g + \Delta E_e \quad (18)$$

Where

- L_i is the internal forces work (friction)
- ΔE_c is kinetic energy variation
- ΔE_g is potential gravitational energy variation
- ΔE_e is potential elastic energy variation

In this case potential energy variations are of not value and friction is negligible, so energy conservation equation is:

$$L_e = \Delta E_c \quad (19)$$

Kinetic energy in a rotational object is given by:

$$E_c = \frac{1}{2} I_G \dot{\alpha}^2 \quad (20)$$

So the sum of internal and external forces works during the process will be equal to the summation of kinetic energy variations:

$$L_e = \sum_i \Delta E_c{}^i = 10kJ \quad (21)$$

This result confirms the previous one and to validate both of them the real energy consumption during the manual process was measured and it was obtained a value of:

$$L_e^m(A) = 11.3\,kJ \quad (22)$$

The difference between this value and the one obtained by analytical calculation is due to the performance of the gears that transmit the rotational motion from the engine to the mandrel.

3.4 ALTERNATIVE TECHNOLOGY ANALYSIS

During fibres deposition process, the main part of A-type mandrel's work is due to accelerations, which occur at every cycle's end. These occur because it is necessary to stop and re-start the rotation to obtain a correct fibre deposition but it doesn't happen if the mandrel rotates at a constant angular speed. In fact, it will take place in one of the two cylindrical parts at the circular torus sides, and there is no more need to stop and restart the rotation.

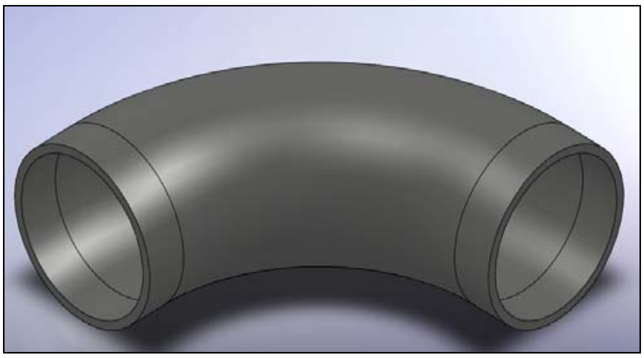

Figure 12 Modified Mandrel in SolidWorks.

The modified mandrel (fig. 12) has been modelled with SOLIDWORKS, a CAD software that allows, once it is defined the mandrel's geometry and its material, to calculate its barycentre and its barycentric inertia's moments. So we have:

$$x_G^B = 0.536m \quad (23)$$

And:

$$I_G^B = 8.22\,kg \cdot m^2 \quad (24)$$

As in the case of the manual winding, from this calculation it is possible to extract mandrel's geometric parameters to put in CADWIND to calculate fibre deposition trajectory's matrix:

- d = 0.4 m;
- R = 0.6 m;
- $\gamma = \pi/2$ rad;
- D = 0.064 m;
- L1 = L2 0.1 m.

The only parameters that are changed are D and L, while the winding ones were the same used in the manual process. Starting from the deposition trajectory's matrix the dynamical analysis has been carried out in the same way we did for the manual winding. From the analysis is clear how the greatest part of the energy consumption during the whole automated process is due to the initial work necessary to give the requested constant rotational speed to the mandrel. Operating in the two ways employed for the manual winding we obtained:

$$L_e = \int_\alpha C d\alpha = 126\, J \tag{25}$$

$$L_e = \sum_i \Delta E_c^{\,i} = 126\, J \tag{26}$$

Figure 13 4-axis computerised machine

Figure 14 B-Type Mandrel in process.

After these analytical calculations it was decided to take out a part program as output from CADWIND. The part program was executed by a 4-axis computerised machine (fig. 13, 14) and the real energy consumption was measured by means on the on-board instrumentation:

$$L_e^m(B) = 164\, J \tag{27}$$

The difference between this value and the one obtained by analytical calculation is due to the performance of the gears that transmit the rotational motion from the engine to the mandrel and the energy consumption along carriage and cross-carriage axis. However it is evident the energy advantage of this alternative technology in non axis-symmetric parts' production, in fact the energy consumption ratio between this technology and traditional one is:

$$E_r = \frac{L_e^m(A)}{L_e^m(B)} = \frac{11300}{164} = 68.9 \tag{28}$$

That means that the manual process consumes 70 times the energy employed by the automated one.

4 CONCLUSIONS

Manual or semi-manual winding have great disadvantages if we compare them to automatic processes, such as inaccuracy and lack of repetition, refuses, low production level and workers interaction with potentially wealth dangerous materials. This work has also demonstrated an energetic advantage of automated winding by the use of B-type mandrel. The lack of inertia's torques during mandrel rotation has a great consequence in the whole process. In this way, in fact, it would possible to provide the deposition robots with low-powered engines and mechanical components that don't have to resist to the stresses due to the torques needed to stop and restart the mandrel rotation. But there are not only benefits in the employment of this kind of technology. The presence of cylindrical extensions is a surplus of material (resin and fibre) and makes it necessary another operation to cut and remove them. To evaluate the real economic advantage of type-B mandrels should be required a complete costs analysis of an automatic filament winding cell for this kind of parts production that will involve all the process elements such as the design and the realisation of a specific deposition robot, fibre and resin consumption during the process, labour and energy consumption, but this is not the aim of the presented paper.

REFERENCES

[1] C. Anon, Robotised production of thermoplastic composites [J], *Br. Plast. Rubber* (1998) 30–31.
[2] Jhon E. Creen, Overview of filament winding, *SAMPE J.* 37 (1) (2001) 7–11.
[3] B.S. Johansen, Aa. Lystrup, M.T. Jensen, CADPATH: a complete program for the CAD-, CAE- and CAM-

winding of advanced fiber composites, *J. Mater. Process. Technol.* 77 (1998) 194–200.
[4] J. Decarvalho, M. Lossie, D. Vandepitte, Optimization of filament wound parts based on non-geodesic winding, *Compos. Manuf.* 6 (2) (1995) 79–84.
[5] J. Scholliers, H. VanBrussel, Computer-integrated filament winding: computer-integrated design, robotic filament winding and robotic quality control, *Compos. Manuf.* 5 (11) (1994) 15–23.
[6] V. Middletm, M.J. Owen, D.G. Elliman, M. Shearing, Developments in non-axisymmetric filament winding, in: *Proceedings of the Second International Conference on Automated Composites*' 88 PRI, Noordwijkerhout, The Netherland, September, 1998, pp. 10.1–10.15.
[7] Laval Christian, Process simulation in filament winding, *Reinforced Plast*. (1991) 40–42.
[8] Li Haisheng, Liang Youdong, Bao Hujun. CAM system for filament winding on elbows. *Journal of Materials Processing Technology* 2005; 161:491–6.
[9] Li Haisheng, Liang Youdong, Bao Hujun. Splines in the parameter domain of surfaces and their application in filament winding. *Computer-Aided Design* 39 (2007) 268–275.

ISSN 1590-8844
International Journal of Mechanics and Control, Vol. 10, No. 02, 2009

IMPROVING THE DYNAMIC PERFORMANCE OF REDUNDANT ELECTROHYDRAULIC SERVOACTUATORS

Giovanni Jacazio Laura Gastaldi

Politecnico di Torino, Department of Mechanics

ABSTRACT

To counteract the variations of servovalve offsets in redundant electrohydraulic servosystems different solutions have been taken, but limited use has been done of techniques based on the injection of compensation signals into the servovalves such to reduce the difference between the pressure differentials across the control lines of the two servoactuators. A research activity has thus been performed in which different equalization techniques have been examined and their relative merits have been assessed. An optimal equalization control strategy has then been devised, capable of minimizing the force fighting between two redundant servoactuators and the appropriate authority limit to the equalization signals has been determined such to prevent unacceptable uncommanded movements in case of failure of a component of the equalization loop.

Keywords: aerospace engineering, redundant servoactuators, equalisation techniques, flight control system, fly-by-wire

1 ELECTROHYDRAULIC SERVOACTUATORS AND FLY-BY-WIRE SYSTEMS

As it is well known, fly-by-wire flight control systems use electrical signalling to relay the pilot commands from the cockpit controls to flight control computers (FCCs) that issue the commands to the flight control actuators and accept from them the electrical feedback signals. In order to ensure the necessary redundancy, two actuators are normally used in primary flight controls to drive the same aerodynamic control surface, with each actuator interfacing with one or more FCCs. In some particular applications three actuators were connected to the same flight control surface, though this configuration has been used only when deemed absolutely necessary since it increases the system complexity. The present paper will thus deal with the typical case of two hydraulic actuators driving an aerodynamic control surface.

Contact author: Giovanni Jacazio[1], Laura Gastaldi[1]

[1] Politecnico di Torino, Department of Mechanics
Corso Duca degli Abruzzi, 24 – 10129 Torino Italy
E-mail: giovanni.jacazio@polito.it
laura.gastaldi@polito.it

When two hydraulic actuators are connected to the same aerodynamic control surface, a very important design issue is to guarantee that no conflict originates between the two actuators such to impair the flight control system performance.
This is particularly critical when the servoactuators hold the flight control surface at a certain fixed position under rapidly varying loads, such as those occurring when the flying aircraft is subjected to gusts or turbulence.
Over the years different design solutions have been worked out for redundant electrohydraulic servoactuators and have been implemented into operational aircraft. The main critical issues to be addressed have been: input signal mismatch, control valve offset, difference between supply pressures of the two hydraulic systems interfacing with the actuators, system robustness following failures and, of course, overall system complexity. Though generalization is often a risky business, still it is possible to state that the different configurations of redundant electrohydraulic servoactuators for flight control systems can be grouped in the following four categories.
Active/standby systems. In these systems one of the two actuators connected to the same flight control surface is active while the second one is in standby. In case the operating actuator fails, the other one is activated and ensures an unabated operation.

Single flow control valve. In these systems the flows to the two hydraulic actuators are simultaneously controlled by two sections of a single control valve.

Reduction to the sensitivity to the control valve offsets. In these systems appropriate actions are taken to reduce the offsets of the control valve and hence the associated mismatch between the actuator forces.

Equalization between the two electrohydraulic servoactuators. In these systems sensors are introduced to measure the differences between the two servoactuators parameters and appropriate control laws are defined to correct those differences.

These four types of architectures will be discussed in the following and the results of a research activity aimed at defining an optimal and robust equalization technique will be presented.

2 LOAD DISTRIBUTION BETWEEN PARALLEL SERVOACTUATORS

When two electrohydraulic servoactuators are connected to the same flight control surface, the forces developed by the two actuators are summed and the problem of ensuring an even load sharing between the two actuators arises. The force developed by an actuator is a function of the pressures acting on the two sides of the actuator piston, and when the actuator is stationary, the pressure differential across the two control valve ports, and thus across the two actuator sides, changes very rapidly with the change of the input signal of the control valve. The valves used to control the pressurized fluid flow to flight control actuators typically consist of closed-center spool valves with very high pressure gains around null so that a large pressure differential, and therefore a large actuator force, is created as a result of small spool displacements. In general, close-center spool valves have a pressure gain that brings about the full pressure differential for a spool displacement equal to 3-5% of maximum. In spool type control valves the spool displacement is generally proportional to the input signal, therefore 3 to 5 % of maximum input signal to the control valve is sufficient to generate the full pressure differential in a no-flow condition.

The flow control valves commonly used in electrohydraulic servoactuators for flight control systems are two-stage electrohydraulic servovalves (EHSVs) which use an internal hydraulic amplifier to convert the electrical input signal into valve spool displacement. Servovalves offer several advantages: they have a limited cost, weight little, require a very small electrical input power (in the 0.1 W range), and they have a large chip shear capability: if the valve spool is stuck in one position due to a debris, the pressure differential between the two sides of the control valve spool created by the internal hydraulic amplifier generates a large force on the spool to break it loose. A problem associated with servovalves is their offset, that can greatly differ from one servovalve to another and that can change with life and with the operating conditions. The servovalve offset is typically considered as the sum of two contributions: the null bias and the null shift. The null bias is the difference between electrical null (zero input current) and hydraulic null (zero pressure differential) under standard operating conditions: supply and return pressures at their rated values, standard ambient temperature, valve mounted on a stationary structure. The typical value of null bias is 3 to 4% of the rated input current and may increase a little at the end of the operating life. The null shift is a temporary variation of null bias with changing operating and environmental conditions and may be as high as 10% of the rated input current. Worst of all the null shift is not a deterministic effect; two nominally equal servovalves may exhibit different null shifts, and also in the opposite directions, with the same change of operating and environmental conditions. It thus turns out that under an adverse combination of null bias and shift, the resulting total servovalve offset can reach 15% of the rated input current.

This particular behaviour of the servovalves has always been a critical issue and high performance light-weight proportional valves, known as direct drive valves (DDVs) within the aerospace community, have also been applied as flow control devices for electrohydraulic servoactuators. DDVs use the force developed by a proportional solenoid to drive the valve spool and do not rely on an internal hydraulic amplifier. This configuration leads to several advantages: reduced offset, lower internal leakage, lower probability of a hardover failure, but it has critical drawbacks. First of all, a much greater electrical input power is required (in the 3 - 5 W range), then, greater weight, reduced chip shear capability and high cost. Moreover, DDVs require an internal spool position feedback loop and often also a spool velocity loop nested within the spool position loop to ensure a high dynamic response with adequate stability. Although DDVs have been used in recent applications, EHSVs are still the preferred choice as flow control valves in electrohydraulic flight control systems, especially considering their low electrical power consumption. The 3-5 W power required by DDVs is apparently little, but when one considers the electrical drivers of several DDVs all tightly packed within a flight control computer, that power consumption and the associated thermal dissipation may become a concern for the electronic designers.

Let us now consider two electrohydraulic servoactuators driving a flight control surface as shown in the concept block diagram of Figure 1. Each servoactuator consists of a linear hydraulic actuator, a flow control valve, a solenoid valve, a shutoff/bypass valve and a control electronics; a position transducer inside the hydraulic actuator provides the feedback signal to the control electronics to close the position control loop. The actuator control electronics receives the position command for the flight control surface from the section of the flight control computer that processes the signals from the cockpit controls and from the aircraft sensors and generates the control signal to the control valve according to a proper control law, thereby modulating the flow/pressures to the hydraulic actuator as required to respond to the pilot inputs and to the variable loads on the aerodynamic surface. The actuator control electronics also generates an on/off electrical signal (arming signal) to a solenoid valve; when the solenoid valve is energized, a high pressure pilot signal is ported to a shutoff / bypass valve which causes this valve spool to move into a position such to connect the ports of the control valve to the two sides of the hydraulic actuator, thus enabling the actuation system operation. If the arming signal is off and the solenoid valve is deenergized, or if no pressure is available due to a hydraulic system failure, the pilot signal is at low pressure and the shutoff / bypass valve is switched into a position such to close the connection between the ports of the control valve and the hydraulic actuator, and to simultaneously interconnect the two sides of the actuator in order to allow a flow recirculation as a consequence of the movements imposed to the actuator from the other active actuator connected to the same flight control surface. Very often, the fluid recirculating between the two sides of the actuator passes through a restrictor providing a pressure drop which is a function of the flow rate and thus of the actuator speed. This feature is instrumental in creating a certain amount of damping to the flight control surface in case of loss of operation of both hydraulic actuators; in such a case, the flight control surface operation is lost, but the same surface automatically positions itself in the aerodynamic wake and the amount of movements around that average position is limited by the actuators damping.

Each of the two identical electrohydraulic servoactuators is hooked to a different aircraft hydraulic system and it is often controlled by two different control lanes, thereby leading to a dual hydraulic/quadruplex electrical architecture. With this architecture, each of the electrical components of the servoactuator (solenoid valve, control valve, position transducer) is dual electrical and accepts/transmits two electrical signals; moreover, the four position signals provided by the position transducers of the two servoactuators (two electrical signal per transducer) are exchanged among the four flight control computers (FCCs) via optoisolated links. Each FCC has thus available all position transducers signals, performs a signal consolidation according to a common logic, and perfectly identical control signals are thus issued by the FCCs to the electrical lanes of the two control valves.

We now consider the case of the two control valves actually consisting of two equal EHSVs. When a servovalve receives a control signal to move off null, a pressure differential is created between the control ports that is proportional to the magnitude of the control signal and on the servovalve pressure gain; this pressure differential is acting upon the actuator that develops a load force.

For an ideal servovalve with zero offset the control signal versus the load force is as shown in Figure 2a. If a servovalve offset is present, the curve of the actuator load force is shifted of an amount equal to the offset as shown in Figure 2b.

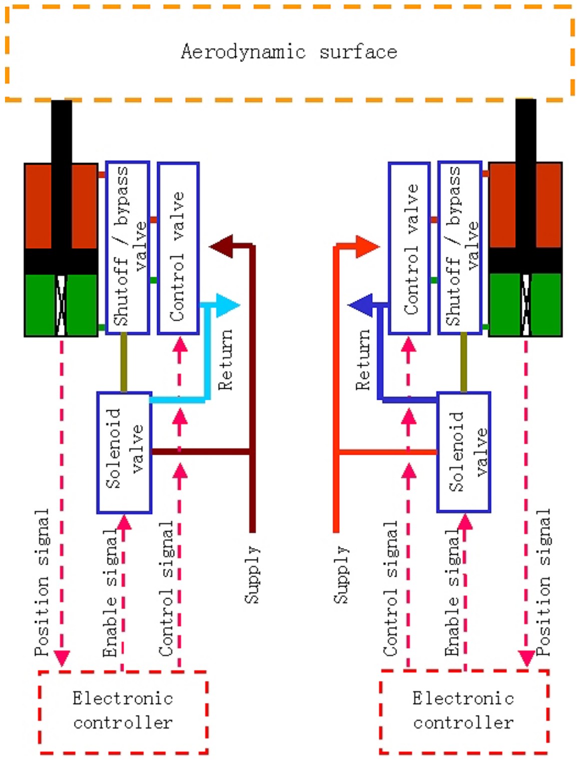

Figure 1 Concept schematic of a dual redundant electrohydraulic servoactuator.

If only one servoactuator were driving the flight control surface, or if the two EHSVs of the two servoactuators had exactly the same offset, the presence of an offset would non originate any problem to the system operation.

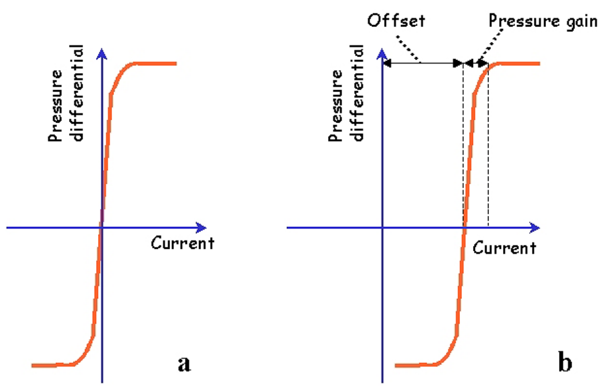

Figure 2 Servovalve control signal vs. actuator load force for a servovalve without offset (a) and with offset (b).

As it is shown in Figure 3a, if a certain load force F_1 must be developed by sum of the two actuators controlled by two EHSVs with equal offsets, a current control signal i_1 must be created by each of the control electronics, such to create

ISSN 1590-8844
International Journal of Mechanics and Control, Vol. 10, No. 02, 2009

a pressure differential across the two sides of each actuator to develop a total force equal to F_1. The control signal i_1 is equal to:

$$i_1 = i_0 + \frac{F_1}{2AG_P} \qquad (1)$$

where:

i_0 = servovalve offset
F_1 = load force on the flight control surface (total of the two actuators)
A = active area of each actuator (assuming balanced area actuators)
G_P = servovalve pressure gain.

For the simple case of a servoactuator controlled with a proportional control law, the position error is equal to the control signal divided by the proportional gain, and since this gain can normally be set sufficiently large while still maintaining the system stability, the resulting position error is low and generally acceptable. Should it be required to further reduce this error, that can be achieved by addiying an integrator with a suitable gain in the control law.
If the two servoactuators driving the same flight control surface are controlled by two servovalves with offsets in opposite directions, a total load force is obtained as shown in the diagram of Figure 3b. The total load force diagram shows a region of zero force gradient in which the overall system does not respond to the control signals issued by the electronic controllers. This behaviour is totally unacceptable in flight control systems because of the resolution, frequency response and dynamic stiffness requirements.
The accuracy requirement for a servoactuator of a primary flight control system is in general not particularly stringent since the flight control servoactuator is actually a subsystem of the aircraft attitude control system that makes up the outer reference loop, and 1-2 % error is normally a requirement. In other words, the overall objective is to accurately control the roll, pitch and yaw angles of the aircraft, and the accuracy errors of the flight control servoactuators are divided by the gains of the outer reference loops. On the other hand, a very tight requirement is the resolution of the servoactuator, which is defined as the capability to respond to the command changes. The resolution requirements depend upon the aircraft category, but are most often in the range from 0.006° to 0.025° of angular deflection of the flight control surface. For the case of 60° maximum that corresponds to a servoactuator resolution between 0.01% and 0.04% of full actuator travel.
Consider now the unlucky case of a dead band (Figure 3b) equal to 20% of maximum servovalve control signal; the electronic controller gain is typically set such that the maximum servovalve control signal is obtained for a position error equal to 4-5% of the full actuator travel, and this stems from the need to provide a suitable frequency response while maintaining an adequate stability margin. As a result, a 20% dead band for the control signal is reflected into a dead band of 0.8% to 1% of full actuator travel, which is about two orders of magnitude greater than the specified resolution.

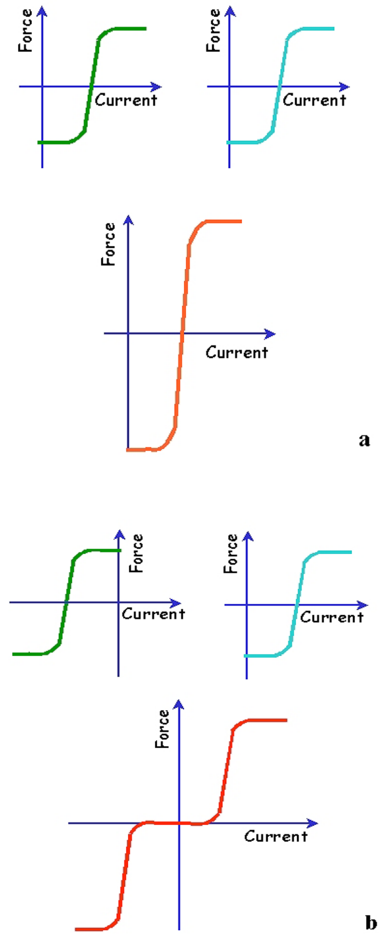

Figure 3 Total load force provided by two servoactuators connected to the same flight control surface for the cases of servoactuators controlled by servovalves with identical offsets (a), and of servoactuators controlled by servovalves with opposite offsets (b).

The dead band around the null condition also negatively affects the system frequency response to small amplitude commands introducing excessive phase lag and gain attenuation.
A second critical condition created by the dead band of the actuators load force is that the system stiffness is practically reduced to zero in that area. As a consequence, when the aircraft flight control surface is subjected to fluctuating loads originated by the atmospheric turbulence, large oscillations of the flight control surface are originated which on their turn give rise to a bumpy aircraft flight.
It is therefore clear that a flight control actuation system architecture in which two servovalve controlled electrohydraulic servoactuators driving the same flight control surface are both active is not acceptable for aircraft primary flight control systems.

3 TECHNIQUES USED FOR A BETTER LOAD SHARING OF PARALLEL SERVOACTUATORS

A solution often used to avoid the dead band in the signal versus load force diagram is to always operate one servoactuator at the time: one of the two servoactuators is operating while the second one is in a bypass mode (active / standby architecture). This solution is simple and eliminates the root cause of the dead band and has for instance been used by Airbus the fly-by-wire primary flight control actuators of their aircraft. Two main drawbacks are however associated with this architecture. First, the actuators must be overdesigned since under normal operating conditions the active actuator must be capable of driving the maximum aerodynamic load plus the load created by the standby actuator. Second, in case of a failure of the hydraulic system providing the pressure supply to the active actuator, a time delay occurs between the onset of hydraulic system failure and the instant in which the standby servoactuator is activated and takes up the control of the aerodynamic surface. This delay depends on the time necessary to positively recognize the failure, on the energization time of the solenoid valve and on the commutation time of the shutoff / bypass valve. During this time delay there is a temporary loss of control of the aerodynamic surface, which does not lead to a flight critical condition since it lasts relatively little (0.1 to 0.2 s), but can anyhow create an unpleasant sudden disturbance during the aircraft flight.
Another approach to minimize the effect of the servovalve offsets and improving the load sharing between two actuators driving a common flight control surface is that to reduce the sensitivity to the offests by softening the pressure gain characteristics of the servovalves. As it can be seen in the diagram of Figure 4, two gain servovalves with large opposite offsets and low pressure gains do not originate a dead band in the combined load force diagram of the two actuators.

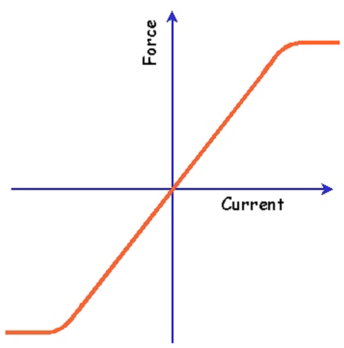

Figure 4 Total load force provided by two servoactuators connected to the same flight control surface for the case of servoactuators controlled by low pressure gain servovalves.

A reduction of the pressure gain can be obtained by overcutting the spool lands in order to achieve an open-center valve configuration. This solution is effective in eliminating the dead band of the load force diagram, but it brings about two main disadvantages: an average low stiffness due to the low pressure gain and large internal leakages due to the open-center configuration. For these reasons, this solution had very limited applications.
A different way for obtaining an even load sharing between two hydraulic actuators driving a common aerodynamic surface consists of controlling the pressurized fluid flows to the two hydraulic actuators with a single control valve consisting of long spool sliding inside a sleeve interfacing with the two hydraulic systems and the two actuators. The valve actually consists of two sections: section I controls the flow between hydraulic system I and actuator I, while section II does the same for hydraulic system II and actuator II. A very careful and accurate machining of the spool lands allows an excellent matching between the two sections, so that equal pressure differentials are created for the two actuators as a result of a spool displacement away from null, providing that the supply pressures of the two hydraulic systems are equal. With this solution, the movement of the spool is obtained by applying appropriately controlled pressures at its two ends. Each opposite end of the spool carries an integral piston sliding inside a cylinder whose two chambers are connected to the control ports of a servovalve, as it is shown in the concept block diagram of Figure 5. The position of the main control valve spool is measured by a position transducer that provides a feedback signal used to close a main control valve position loop. The two servovalves are of a little size since they only have to control the flows resulting from the displacement of the main control valve spool, and present low pressure gains. High gains are not necessary here because the main control valve position feedback loop does not need to be particularly stiff. As it has been shown in the diagram of Figure 4, the use of servovalves with low pressure gains minimizes the negative effects of adverse combinations of servovalves offsets; at the same time, there is no reduction of the servoactuator stiffness since the low pressure gain only affects the stiffness of the internal position loop of the main control valve and not that of the servoactuator loop, which is ensured by the high pressure gain of the main control valve. Although this architecture is more complex, it has been widely used in fly-by-wire primary flight control systems due its undisputable performance advantages. The primary flight control systems of the Tornado and of the F-18 are examples of application of this architecture.

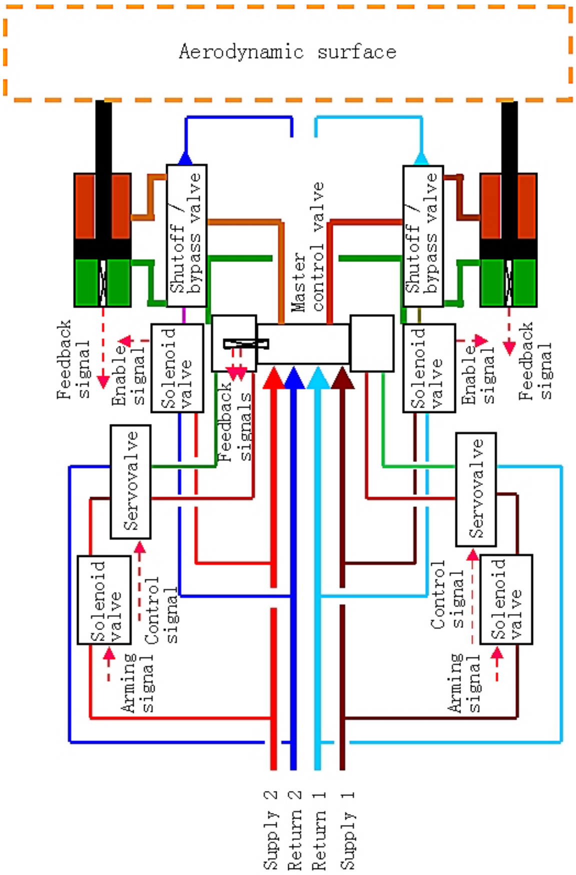

Figure 5 Concept block diagram of a system comprised of two electrohydraulic servoactuators controlled by a common dual section flow control valve.

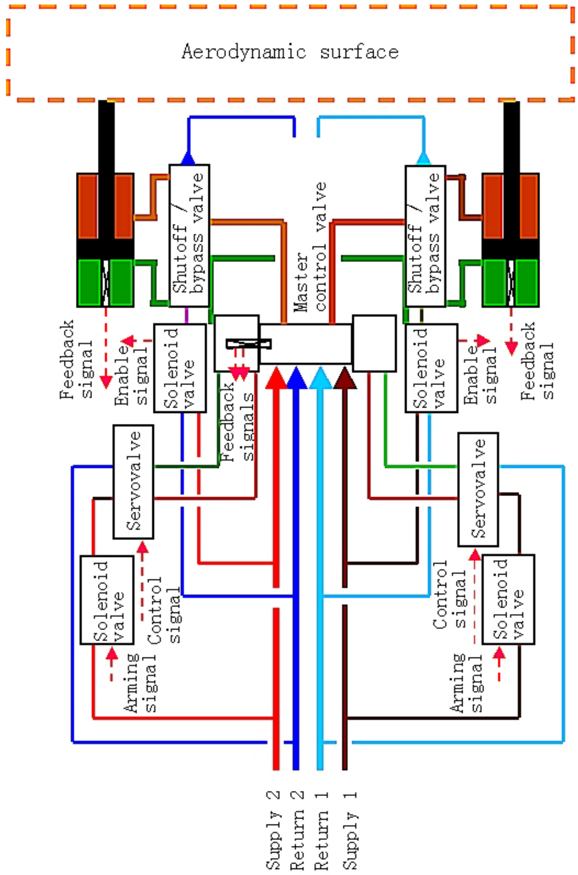

Figure 6 Concept block diagram of two electrohydraulic servoactuators with individual servovalves (EHSVs) and differential pressure equalization.

The same design concept of using a single valve for modulating the flows to two hydraulic actuators can be pursued by using a direct drive valve whose spool is driven by multiple force motors. The spool position is measured by a transducer that provides the signal necessary to close the spool position feedback loop. High performance DDVs tend to be marginally stable and their stability is often improved by providing them with the capability of measuring the spool velocity and increase their internal damping by creating a spool velocity feedback loop internal to the spool position loop. Primary flight control actuation systems based on this architecture have been used in the primary flight control systems of some military aircraft such as the Eurofighter. As it has been pointed out at the beginning of paragraph 2, a DDV based architecture as the merits of an overall greater reliability and of lower internal leakages, but the much greater electrical power draw and cost may thwart their use in several applications. Moreover, the lower axial force developed on the spool by the force motors when compared to that developed by hydraulic pressure raises concerns about their ability of shearing off large debris that could remain stuck between spool and sleeve and create a spool lock.

A fourth way to improve the load sharing between two electrohydraulic servoactuators while simply using two servovalves, with each valve controlling the flow to its own actuator, is to sense the pressure differentials across the two actuators, compare the two pressure differentials and inject compensation signals into the servovalves currents such to equalize the actuators pressure differentials (Figure 6).
This technique is simple in principle, but its implementation is not an easy task since a careful tradeoff must be performed between the need of equalizing the actuators pressure differentials and that to avoid excessive transient uncommanded movements in case of a failure and of the subsequent shutoff after the failure has been recognized. The main areas requiring a careful scrutiny are: definition of the best strategy to change from the system null that existed prior to the failure to the system null after the failure, performance with different supply pressures of the two hydraulic systems, dynamic response and stability of the equalization loop, errors of the pressure measuring devices, maximum authority granted to the equalization loop, failure detection of the differential pressure sensors and corrective actions. Concerns about these design issues have been the main reason for a very limited application of this type of architecture to fly-by-

wire flight control systems. A partial application of this architecture is found in the primary flight controls of the B2. The primary flight control servoactuators of this aircraft actually have their flows controlled by separate DDVs and differential pressure sensors are used by each servoactuator to provide a dynamic pressure feedback for improved dynamic performance. In addition, the signals of the two differential pressure sensors are compared to each other to create compensation signals to the two DDVs to reach a better load sharing between the actuators. DDVs, however, exhibit a much lower offset than EHSVs, therefore, the equalization issue is much less critical than with EHSVs.

4 OPTIMISATION OF THE CONTROL STRATEGY FOR EQUALIZING PARALLEL SERVOACTUATORS CONTROLLED BY ELECHTROHYDRAULIC SERVOVALVES

As emphasized before, the purpose of the research activity presented in this paper was to define an optimized solution for achieving an even load sharing between two hydraulic actuators separately controlled by individual electrohydraulic servovalves. The merits of the solution that was eventually developed are: simple system architecture, lower cost, limited transient disturbance following a failure, possibility of operation following a seizure of a valve spool. Though the probability of a seizure of valve spool is considered very low, still the system architectures based on a single flow control valve for the two actuators (schematic of Figure 5) present multiple redundant control lanes with a common link made up by the single main control valve; a failure of this valve leads to the loss of operation of the relevant flight control surface. Controlling the actuator flows with two different control valves offers a greater survivability to the flight control system. The concept schematic for the system under study is therefore the one shown in Figure 6.

In order to define the general architecture of a control law aimed at equalizing the forces developed by two actuators controlled by electrohydraulic servovalves it is convenient to refer to a linear model of the system; the actual values of the control parameters will then be fine tuned with the use of a detailed non-linear model, that will also be used for evaluating the system performance under normal operating, degraded and failure conditions. The block diagram of the linearized mathematical model of the system is illustrated in Figure 7. The input command x_C is compared to the position feedback z to generate the position error e which is processed by a control law with a transfer function $G_1(s)$ to provide the control signals to the two servoactuators. The control signals (equal for both servoactuators) are modified by the equalization signal h, which is subtracted to the control signal of servoactuator 1 and added to the control signal of servoactuator 2; the modified control signals are then fed to digital-to-analogue converters to generate the input signals to the servoamplifiers with a gain G_A generating the controlled currents i_1 and i_2 to the servovalves. The offsets of the two servovalves are represented in the block diagram by disturbance currents i_{d1} and i_{d2}, which are added to the actual currents i_1 and i_2. Therefore, the two servovalves will behave in response to equivalent currents $i_{V1} = i_1 + i_{d1}$ and $i_{V2} = i_2+i_{d2}$. The remaining portion of the forward path of the control loop is the usual block diagram of a hydraulic servoactuator; $G_V(s)$ is the transfer function defining the servovalve dynamics, G_Q and G_P the servovalves flow and pressure gains, C the hydraulic capacitance of each actuator chamber with the actuator assumed at mid position, k_L the internal leakage coefficient, A the actuator area, k the stiffness of the actuator attachment point to the underlying structure, c_V the external damping coefficient, m the total mass of the moving parts reflected to the actuators linear output. In the same block diagram δp_1 and δp_2 are the pressure differentials across the two sides of actuators 1 and 2, F_1 and F_2 the corresponding actuator forces, R the load force, y the actuators linear displacement.

The transfer function H(s) of the feedback path is that of the demodulator filtering the electrical signal provided by the actuators position transducer. Fly-by-wire flight control systems typically use LVDT type position transducers because of their robustness and capability of operating in harsh environments; these transducers are supplied with a high frequency ac input voltage and require low-pass second-order filters to cancel out the alternating component of the output signal.

The two pressure differentials δp_1 and δp_2 are measured by differential pressure transducers also consisting of LVDTs measuring the displacement of a spring centered cylinder subjected to the pressure differential. The output signal of each of these transducers is therefore demodulated by a filter with a transfer function $H_P(s)$. The difference between the two pressure differential signals is then fed to the equalization control law that is indicated in the block diagram of Figure 7 with the transfer function $H_e(s)$, which is actually a complex function as it is shown in the diagram of Figure 8.

The difference $\delta p_{1\text{-}2} = \delta p_1 - \delta p_2$ between the two pressure differential signals first passes through an activation block that is commanded by the enable/disable control logic.

In order for the equalization function to be activated, both servoactuators must operate correctly and be pressurized, which condition is signalled by the pressure switches of the two servoactuators.

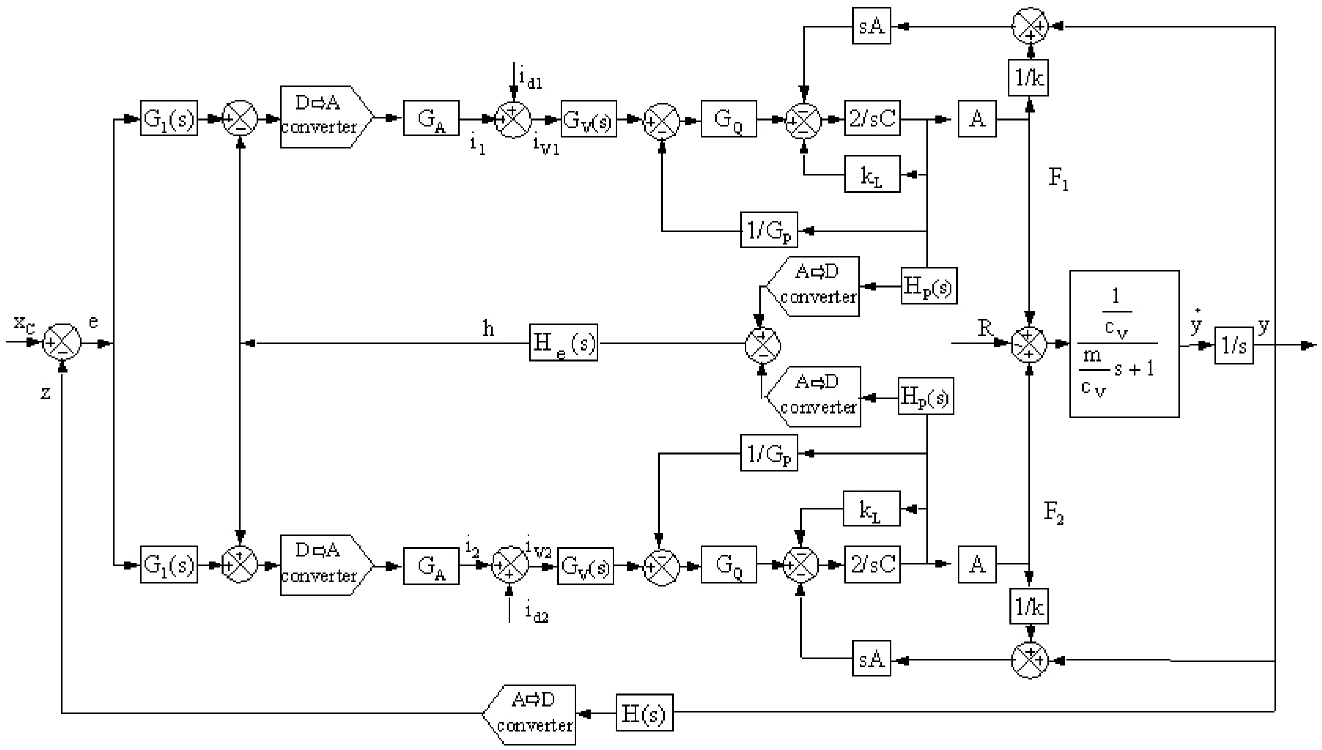

Figure 7 System block diagram.

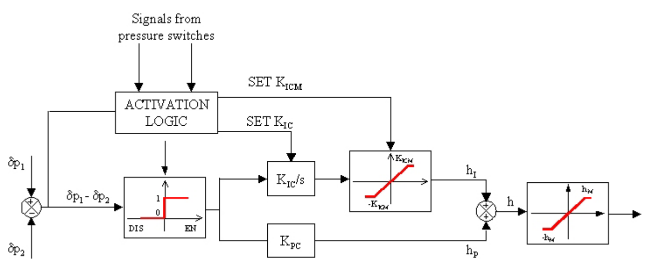

Figure 8 Block diagram of the equalization control law.

If both pressure switches signals are "on", an enable signal is sent to the activation block that transfers the $\delta p_{1\text{-}2}$ signal to the following blocks; on the contrary, the output of the activation block is equal to zero. The $\delta p_{1\text{-}2}$ signal is processed by a modified PI controller in which the gain K_{IC} of the integral part of the controller is varied with time when the equalization logic is activated, starting from an initial large value at switch-on to a smaller one after the initial equalization transient has settled. The integrator output signal is saturated to maximum / minimum values; the saturation limits are enabled if both pressure switches signals are "on"; on the contrary they are set to zero. The output signals h_I and h_P from the integral and proportional controllers are summed up, the resulting equalization signal h is saturated to a maximum/minimum limit and injected with the appropriate sign into the summing points of the forward paths of the two servoactuators control loops.

In order to better understand the rationale behind the selection of the equalization controil law outlined above, it is convenient to consider a simplified case of a system in which the control transfer function $G_1(s)$ is a pure gain K_1, the equalization transfer function $H_e(s)$ consists only of a proportional gain K_{PC}, and the system is in a stationary condition. For these simplified conditions, the two pressure differentials δp_1 and δp_2 are given by the following expressions, where e is the servoactuators position error and $K'_L=G_Q/G_P$ is the ratio between servovalve flow and pressure gains..

$$\delta p_1 = \frac{K_1 G_Q G_A}{k_L + K_L'} e + \frac{G_Q\left(\dfrac{k_L + K_L'}{G_A G_Q K_{PC}} + 1\right) i_{d1} + G_Q i_{d2}}{\left(k_L + K_L'\right)\left(\dfrac{k_L + K_L'}{G_A G_Q K_{PC}} + 2\right)} \quad (2)$$

$$\delta p_2 = \frac{K_1 G_Q G_A}{k_L + K_L'} e + \frac{G_Q i_{d1} + G_Q\left(\dfrac{k_L + K_L'}{G_A G_Q K_{PC}} + 1\right) i_{d2}}{\left(k_L + K_L'\right)\left(\dfrac{k_L + K_L'}{G_A G_Q K_{PC}} + 2\right)} \quad (3)$$

For the worst case of two servovalves with opposite offsets, $i_{d1} = -i_{d2} = i_{d0}$, equations (2) and (3) become:

$$\delta p_1 = \frac{K_1 G_Q G_A}{k_L + K_L^{'}} e + \frac{i_{d0}}{1/G_Q \cdot \left(k_L + K_L^{'}\right) + 2G_A K_{PC}} \qquad (4)$$

$$\delta p_2 = \frac{K_1 G_Q G_A}{k_L + K_L^{'}} e - \frac{i_{d0}}{1/G_Q \cdot \left(k_L + K_L^{'}\right) + 2G_A K_{PC}} \qquad (5)$$

The flow gain G_Q is a parameter that is selected as a function of the actuation speed to be developed by the actuator, therefore, should no equalization be present ($K_{PC} = 0$), the only possible way for reducing the difference between δp_1 and δp_2 is to increase the internal leakage (greater k_L) or reduce the pressure gain G_P. However, both these ways lead to a reduction of the value of the coefficient multiplying the servoloop error e, which implies a reduction of the servoactuator stiffness, since a greater error is necessary to obtain the same pressure differential. Introducing the pressure equalization ($K_{PC} > 0$) brings about a reduction of the effect of the offset current id0 on the pressure differentials. The difference between δp_1 and δp_2 thus decreases with increasing the value of K_{PC}, but this process cannot continue above a certain limit for it would lead to an instability of the pressure equalization loop. However, it must be considered that the servovalve offsets are the result of different contributions, as it was outlined at the beginning of this paper. Some contributions (null bias and null shift with temperature) are steady-state or quasi-steady-state factors and their effect can thus be recovered by introducing a low gain integrator (K_{IC} in the block diagram of Figure 8), that eventually develops a signal such to compensate these contributions to the servovalve offsets. Since the maximum null bias is about 4% of the rated servovalve current, and the maximum null shift with temperature can take another 4% of rated servovalve current, the saturation limit K_{ICM} of the block diagram of Figure 8 can be set such to correspond to 8% of the rated servovalve current. However, in case the signal of one of the two pressure switches is "off", the saturation limit K_{ICM} is set to zero to fully disable the equalization logic. At the same time, the saturation limit h_M of the entire equalization control law can be set to 15% of the rated servovalve current, which is the maximum possible offset under normal servovalve operation.

The rationale for this control law is to use the integral control for compensating the steady-state offsets, while using the proportional control only for compensating the rapid variation of servovalve offsets, such as those originated by variations of the return pressure due to the pressure drops originated by the flow through the return lines. Since the proportional control has to compensate only a fraction of the servovalve offset, it can be kept lower than it would be required for entire offset compensation, and the equalization loop stability can be maintained while minimizing the residual difference between the two pressure differentials.

The gain K_{IC} of the integrator must be kept low to prevent an adverse effect on the stability of the equalization loop, but this may be a negative factor at the start-up when the equalization logic is activated, since it would lead to a long settling time. The value of the integrator gain is thus initially set high and equal to 10 times its normal value and is reduced to its normal value as the difference $\delta p_1 - \delta p_2$ is reduced to a value equal to 20% of the supply pressure. From then on, the integrator gain remains constant at that value, no matter of the variations of $\delta p_1 - \delta p_2$. This technique allows an acceleration of the initial settling time without affecting the equalization loop stability.

5 CHARACTERISTICS OF A SERVOACTUATOR FOR A PRIMARY FLIGHT CONTROL SYSTEM

The merits of the equalization control technique described in the previous paragraph have been assessed with reference to a typical fly-by-wire system for the control and actuation of a primary flight control surface of a medium-size aircraft. The system consists of two microprocessor controlled electrohydraulic servoactuators with the main characteristics reported in table I.

Table I servosystem characteristics

Supply pressure	28 MPa
Return pressure	0.5 MPa
Hydraulic fluid conforming to MIL-PRF- 5606	
Actuator stroke	100 mm
Maximum external load	25000 N
No-load speed	100 mm/s
Total system inertia reflected to actuator	90 kg
External damping coefficient	10000 Ns/m
Stiffness of the actuator attachment point	$4x10^7$ N/m
LVDTs excitation frequency	3 kHz
Microprocessor recursion rate	400 Hz
Microprocessor computation time	1 ms
Analogue/digital converters resolution	12 bit

The design characteristics of the actuators and their components, and the system control law were defined to meet the requirements listed above. Extensive simulations were run for the ideal case of two servoactuators supplied with identical pressures and controlled by zero offset servovalves; the results of these simulations were used as a benchmark for the performance of servoactuators with servovalves exhibiting different offsets and for assessing the merit of the equalization control technique. The system response to different conditions was taken as representative of the system dynamic behaviour; these conditions were:

- No-load - frequency response for input commands of ±0.1 mm (autopilot adjustments) and ±2 mm (small amplitude pilot commands)

- No actuator command - dynamic stiffness for a load fluctuations of ±500 N (level flight under turbulence) and ±3000 N (level flight under gusts)
- No actuator command - half sine variation of load from 0 to 10000 N to 0 in 0.5 s (windshear).

6 DYNAMIC BEHAVIOUR OF SERVOACTUATORS WITH OFFSETS

Starting from the reference system with ideal servoactuators, a system consisting of actuators controlled by servovalves with different offsets was analyzed. In particular, servovalves with two opposite offsets corresponding to 10% of the rated current were considered, which case could well occur within the normal range of operating conditions. The dynamic behaviour of the system was assessed in response to the same input conditions considered for the ideal servoactuator. A system **without equalization** was first analyzed which showed as expected a large worsening of its dynamic characteristics, as clearly seen in Figures 9 through 12. When a small input command of ±0.1 mm amplitude is given at a very low frequency of 0.1 Hz (Figure 9a), a system with opposite servovalve offsets can respond to the command, though with a relatively large phase lag; however, if the command frequency is increased to 0.2 Hz (Figure 9b), the same system is practically not responding any longer to the small amplitude command. If the amplitude command is increased to ±2 mm, the differences between systems with and without servovalve offsets become marginal, since the dead band in the combined pressure gain curve is negligible with respect to the command amplitude, and some differences show up only at high frequencies as it can be seen in Figure 10.

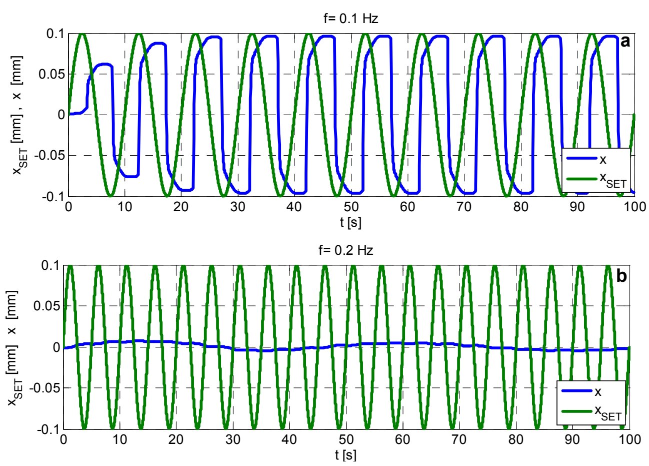

Figure 9 Servosystem without equalization: time response with no-load and input displacement of ±0.1 mm (a) f=0.1 Hz and (b) f=0.2 Hz.

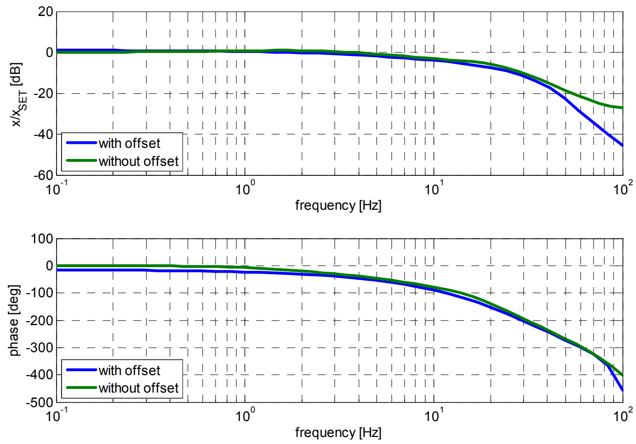

Figure 10 Servosystem without equalization: frequency response with no-load and input displacement of ±2 mm.

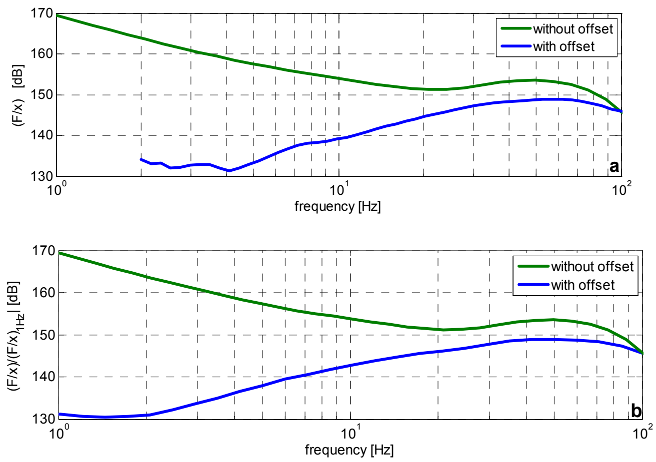

Figure 11 Servosystem without equalization: dynamic stiffness with eternal force (a) R=±500 N and (b) R=±3000 N. (Stiffness units are N/m).

A very large difference in the system performance between the two conditions of zero servovalve offsets or maximum opposite offsets occurs for the dynamic stiffness. Since the typical frequency range for the loads fluctuations on the primary flight control surfaces is between 5 and 20 Hz, it can be seen from the diagrams of Figure 11 that a dramatic reduction of the dynamic stiffness up to 30 dB can be originated by the opposite servovalves offsets, which is clearly unacceptable. This loss of dynamic stiffness is reflected into the system response to a strong gust, as shown in Figure 12. A system without offsets reacts with a minimum transient error, while a system with opposite servovalves offsets shows a large compliance and a transient disturbance up to 0.7 mm of actuators stroke.

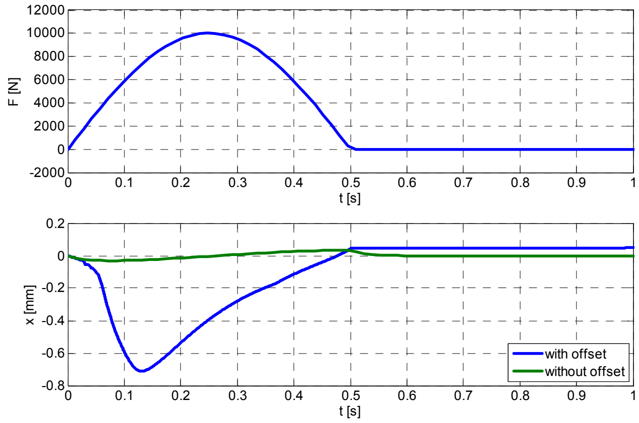

Figure 12 Servosystem without equalization: response to a half sine variation of load.

A system **with pressure differential equalization** according to the strategy outlined at the end of paragraph 4 was then analyzed, and the system response to the different input conditions is illustrated in Figures 13 through 16. In particular, Figure 10 shows that no practical difference exists between the ideal system (no servovalve offset) and a system with maximum opposite servovalves offsets and differential pressure equalization; the curves for these two conditions are actually superimposed in the diagrams of Figures 13 and 14. Some minor difference exists in the response to a large gust (Figure 16), and the maximum transient position error is equal to 0.052 mm compared to 0.03 mm of the ideal system. However, this error is one order of magnitude lower than the error of a system with servovalve offset without differential pressure equalization, which is equal to 0.7 mm as it can be seen in Figure 12.

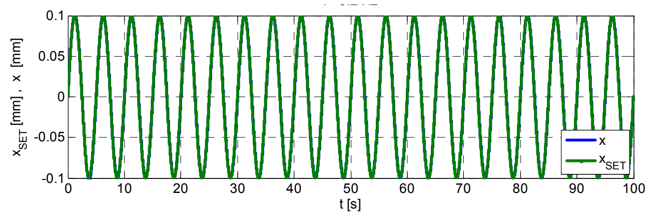

Figure 13 Servosystem with equalization: time response with no-load and input displacement of ±0.1 mm at f=0.2 Hz.

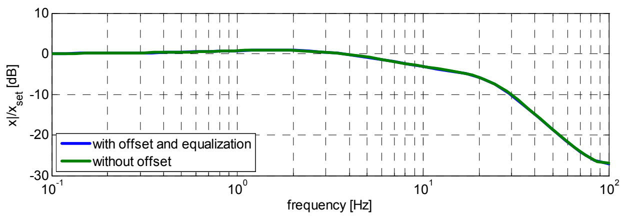

Figure 14 Servosystem with equalization: frequency response with no-load and input displacement of ±2 mm.

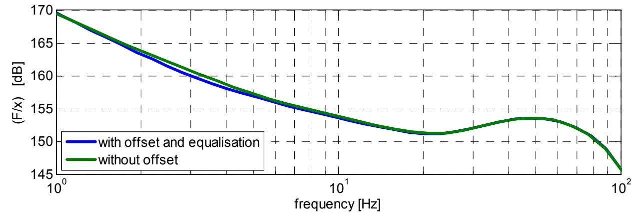

Figure 15 Servosystem with equalization: dynamic stiffness with external force R=±3000 N (stiffness units are N/m).

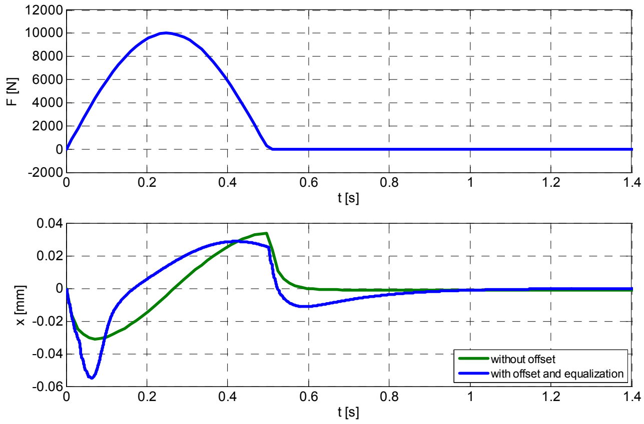

Figure 16 Servosystem with equalization: response to a half sine variation of load

7 CONCLUSIONS

The research activity performed on the equalization techniques for dual redundant electrohydraulic servoactuators for aircraft flight controls showed that the implementation of a suitable control strategy permits to attain a good load sharing between two electrohydraulic servoactuators of the aerodynamic force acting on a flight control surface. By using in an appropriate way the signals provided by two pressure differential transducers it is possible to perform an effective compensation of variable servovalves offsets and to minimize the transient disturbances following a failure, which enables the use of servoactuators with a simple and less expensive architecture.

An accurate analytical model was prepared that clearly showed the merits of implementing the pressure differential equalization control algorithm.

REFERENCES

[1] Thayer W.J. Redundant Electrohydraulic Servoactuators. Moog Technical Bulletin 127, May 1976.

[2] Harschburger H.E. Development of Redundant Flight Control Actuation Systems for the F/A-18 Strike Fighter. SAE paper 831484, 1983.

[3] Shaefer W.S., Inderhees L.J. and Moynes, J.F. Flight Control Actuation System for the B-2 Advanced Technology Bomber. SAE paper 91112, 1991.

[4] Straub, H.H. and Creswell R. The Boeing 747-400 Upper Rudder Control System with Triple Tandem Valve. SAE paper 912133, 1991.

[5] Raymond E.T. and Chenoweth C.C. *Aircraft Flight Control Actuation System Design*. SAE, 1993.

[6] Schmitt V.R., Morris, J.W. and Jenney G.D. *Fly-by-Wire*. SAE, 1998.

[7] Van den Bossche D. A380 Primary Flight Control Actuation System. *Proceedings of the Int. Conference on Recent Advances in Aerospace Actuation Systems and Components*; Toulouse, France, June 2001.

[8] Jacazio G. and Gastaldi L. Equalization techniques for dual redundant electrohydraulic servoactuators for flight control systems. *Proc. Fluid Power and Motion Control*, Bath (UK), pp. 543-557, 2008.

ISSN 1590-8844
International Journal of Mechanics and Control, Vol. 10, No. 01, 2009

TEMPLATE FOR PREPARING PAPERS FOR PUBLISHING IN INTERNATIONAL JOURNAL OF MECHANICS AND CONTROL

Author1* Author2**

* affiliation Author1
** affiliation Author2

ABSTRACT

This is a brief guide to prepare papers in a better style for publishing in International Journal of Mechanics and Control (JoMaC). It gives details of the preferred style in a template format to ease paper presentation. The abstract must be able to indicate the principal authors' contribution to the argument containing the chosen method and the obtained results. (max 200 words)

Keywords: keywords list (max 5 words)

1 TITLE OF SECTION (E.G. INTRODUCTION)

This sample article is to show you how to prepare papers in a standard style for publishing in International Journal of Mechanics and Control.
It offers you a template for paper layout, and describes points you should notice before you submit your papers.

2 PREPARATION OF PAPERS

2.1 SUBMISSION OF PAPERS

The papers should be submitted in the form of an electronic document, either in Microsoft Word format (Word'97 version or earlier).
In addition to the electronic version a hardcopy of the complete paper including diagrams with annotations must be supplied. The final format of the papers will be A4 page size with a two column layout. The text will be Times New Roman font size 10.

Contact author: author1[1], author2[2]

[1]Address of author1.

[2]Address of author2 if different from author1's address.

2.2 DETAILS OF PAPER LAYOUT

2.2.1 Style of Writing

The language is English and with UK/European spelling. The papers should be written in the third person. Related work conducted elsewhere may be criticised but not the individuals conducting the work. The paper should be comprehensible both to specialists in the appropriate field and to those with a general understanding of the subject.
Company names or advertising, direct or indirect, is not permitted and product names will only be included at the discretion of the editor. Abbreviations should be spelt out in full the first time they appear and their abbreviated form included in brackets immediately after. Words used in a special context should appear in inverted single quotation mark the first time they appear. Papers are accepted also on the basis that they may be edited for style and language.

2.2.2 Paper length

Paper length is free, but should normally not exceed 10000 words and twenty illustrations.

2.2.3 Diagrams and figures

Figures and Tables will either be entered in one column or two columns and should be 80 mm or 160 mm wide respectively. A minimum line width of 1 point is required at actual size. Captions and annotations should be in 10 point with the first letter only capitalised *at actual size* (see Figure 1 and Table VII).

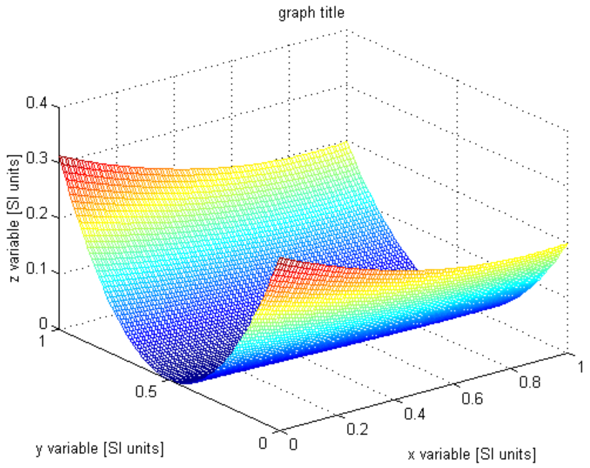

Figure 1 Simple chart.

Table VII - Experimental values

Robot Arm Velocity (rad/s)	Motor Torque (Nm)
0.123	10.123
1.456	20.234
2.789	30.345
3.012	40.456

2.2.4 Photographs and illustrations
Authors could wish to publish in full colour photographs and illustrations. Photographs and illustrations should be included in the electronic document and a copy of their original sent. Illustrations in full colour …

2.2.5 Equations
Each equation should occur on a new line with uniform spacing from adjacent text as indicated in this template. The equations, where they are referred to in the text, should be numbered sequentially and their identifier enclosed in parenthesis, right justified. The symbols, where referred to in the text, should be italicised.

- point 1
    - point 2
        - point 3

1. numbered point 1
    2. numbered point 2
        3. numbered point 3

$$W(d) = G(A_0, \sigma, d) = \frac{1}{T}\int_0^{+\infty} A_0 \cdot e^{-\frac{d^2}{2\sigma^2}} dt \qquad (1)$$

3 COPYRIGHT

Authors will be asked to sign a copyright transfer form prior to JoMaC publishing of their paper. Reproduction of any part of the publication is not allowed elsewhere without permission from JoMaC whose prior publication must be cited. The understanding is that they have been neither previously published nor submitted concurrently to any other publisher.

4 PEER REVIEW

Papers for publication in JoMaC will first undergo review by anonymous, impartial specialists in the appropriate field. Based on the comments of the referees the Editor will decide on acceptance, revision or rejection. The authors will be provided with copies of the reviewers' remarks to aid in revision and improvement where appropriate.

5 REFERENCES (DESCRIPTION)

The papers in the reference list must be cited in the text. In the text the citation should appear in square brackets [ ], as in, for example, "the red fox has been shown to jump the black cat [3] but not when...". In the Reference list the font should be Times New Roman with 10 point size. Author's first names should be terminated by a 'full stop'. The reference number should be enclosed in brackets.
The book titles should be in *italics*, followed by a 'full stop'. Proceedings or journal titles should be in *italics.* For instance:

REFERENCES (EXAMPLE)

[1] Smith J., Jones A.B. and Brown J., *The title of the book*. 1st edition, Publisher, 2001.
[2] Smith J., Jones A.B. and Brown J., The title of the paper. *Proc. of* Conference *Name*, where it took place, Vol. 1, paper number, pp. 1-11, 2001.
[3] Smith J., Jones A.B. and Brown J., The title of the paper. *Journal Name*, Vol. 1, No. 1, pp. 1-11, 2001.
[4] Smith J., Jones A.B. and Brown J., *Patent title*, U.S. Patent number, 2001.

International Journal of Mechanics and Control – JoMaC

Published by Levrotto&Bella

TRANSFER OF COPYRIGHT AGREEMENT

NOTE: Authors/copyright holders are asked to complete this form signing section A, B or C and mail it to the editor office with the manuscript or as soon afterwards as possible.	*Editor's office address:* Andrea Manuello Bertetto Elvio Bonisoli *Dept. of Mechanics* *Technical University – Politecnico di Torino* *C.so Duca degli Abruzzi, 24 – 10129 Torino – Italy* *e_mail: jomac@polito.it* *fax n.: +39.011.564.6999*

The article title:

By:____

To be Published in ***International Journal of Mechanics and Control JoMaC***
Official legal Turin court registration Number 5320 (5 May 2000) - reg. Tribunale di Torino N. 5390 del 5 maggio 2000

A Copyright to the above article is hereby transferred to the JoMaC, effective upon acceptance for publication. However the following rights are reserved by the author(s)/copyright holder(s):

1. All proprietary rights other than copyright, such as patent rights;
2. The right to use, free or charge, all or part of this article in future works of their own, such as books and lectures;
3. The right to reproduce the article for their own purposes provided the copies are not offered for sale.

To be signed below by all authors or, if signed by only one author on behalf of all co-authors, the statement A2 below must be signed.

A1. All authors:

SIGNATURE________________________________DATE__________ SIGNATURE________________________________DATE__________

PRINTED NAME____ PRINTED NAME____

SIGNATURE________________________________DATE__________ SIGNATURE________________________________DATE__________

PRINTED NAME____ PRINTED NAME____

A2. One author on behalf of all co-authors:
"I represent and warrant that I am authorised to execute this transfer of copyright on behalf of all the authors of the article referred to above"

PRINTED NAME____

SIGNATURE____________________________________ TITLE________________________________ DATE_______________

B. The above article was written as part of duties as an employee or otherwise as a work made for hire. As an authorised representative of the employer or other proprietor. I hereby transfer copyright to the above article to Editel-Pozzo Gros Monti effective upon publication. However, the following rights are reserved:

1. All proprietary rights other than copyright, such as patent rights;
2. The right to use, free or charge, all or part of this article in future works of their own, such as books and lectures;
3. The right to reproduce the article for their own purposes provided the copies are not offered for sale.

PRINTED NAME____

SIGNATURE____________________________________ TITLE________________________________ DATE_______________

C. I certify that the above article has been written in the course of employment by the United States Government so that no copyright exists, or by the United Kingdom Government (Crown Copyright), thus there is no transfer of copyright.

PRINTED NAME____

SIGNATURE____________________________________ TITLE________________________________ DATE_______________

CONTENTS

next number scheduled titles:

MR Compatible Device for Active and Passive Foot Movements
G. Belforte, G. Quaglia, G. Eula, S. Appendino, F. Cauda, K. Sacco

A 3D-Laser Scanner for Mobile Robot Applications
G. Reina, N. I. Giannoccaro, A. Messina, A. Gentile

Calibration of wrist-mounted profile laser scanning probe using a tool transformation approach
T. Borangiu, A. Dogar, A. Dumitrache

The Open Control Concept in a Holonic Manufacturing System
S. Răileanu, T. Berger, Y. Sallez, T. Borangiu, D. Trentesaux

A Lunar Rover Leg: Optimal Design of a Decoupling Joint
R. Ambu, C. Falchi, A. Manuello Bertetto

Design and Operation Issues for Parallel Robotic Devices in the Rehabilitation of Stroke Patients
M. Ceccarelli, D. Pîslă, F. Graur, E. Ottaviano, C. Vaida, R. Ungur, S. Grande, M. Pop